Investigating Brine and Air Porosity from Sea Ice Samples from the Antarctic Marginal Ice Zone



A dissertation in fulfilment of a Masters of Science in Chemical Engineering

Prepared by:
Hayley Swait

Supervisor:
Dr Tokoloho Rampai

University of Cape Town
Department of Chemical Engineering
Marine and Antarctic Research centre for Innovation and Sustainability (MARiS)

May 2024

University of Cape Town

The copyright of this thesis vests in the author. No quotation from it or information derived from it is to be published without full acknowledgement of the source. The thesis is to be used for private study or non-commercial research purposes only.

Published by the University of Cape Town (UCT) in terms of the non-exclusive license granted to UCT by the author.

University of Cape Town

Plagiarism Declaration

I understand the meaning of plagiarism and declare that all work presented in this dissertation, save for that which is properly acknowledged, is my own. This thesis/dissertation has been submitted to the Turnitin module (or equivalent similarity and originality checking software) and I confirm that my supervisor has seen my report and any concerns revealed by such have been resolved with my supervisor.

Hayley Swait

Signature Signed by candidate **Date: 07 May 2024**

Abstract

Micro-scale sea ice properties have cascading effects onto larger scale climate and ocean systems. Brine and air inclusions are influenced by the growth conditions, which are highly dynamic in the Antarctic Marginal Ice Zone (MIZ) compared to the calmer Arctic. There are varying depths within an Antarctic pancake floe due to these dynamic conditions, yet the spatial variability of brine and air porosity profiles has not been previously investigated. Additionally, the sea ice brine phase is greatly influenced by temperature, yet similarly there are limited studies on the impact of temperature storage and heating methods on brine inclusions. Understanding the impacts of environmental and storage conditions is essential to ensure accurate and representative analysis of sea ice's thermally responsive properties.

In this study, non-destructive X-ray computer tomography (CT) analysis was used to investigate the brine and air inclusions within pancake ice from the Antarctic MIZ during winter 2019 and 2022 expeditions. Sampling protocols from the 2019 expedition were optimised during the 2022 expedition to store samples at the CT analysis temperature (-10°C) to minimise the impact of low temperature (-18°C) storage on these inclusions. Investigating the impacts of low temperature storage and heating methods on these inclusions was then conducted through uni- (UD) and multidirectional (MD) heating samples from -18°C to -10°C.

This study showed on average reductions of 41% in the brine porosity of sea ice after being subjected to low temperature storage, unlike air porosity that showed no significant changes. However, there was no significant difference between the UD and MD heating methods. The number of brine inclusions increased after low temperature storage. The brine inclusions showed a decrease in sphericity in samples subjected to low temperature storage conditions. Air showed slight increases in the number of air inclusions in the sections in the upper region of the ice while the lower region showed a decrease in air number densities, potentially attributed to the gas saturation factor within the sea ice. In addition to the storage conditions influencing the inclusions, the spatial variability of coring locations within a pancake floe has also shown to have slight variation in the porosity profiles within sea ice samples.

This study disqualifies the general assumption that sea ice porosity is not affected by low temperature storage conditions and therefore the storage conditions are of paramount importance in studying the microstructural properties of sea ice. Maintaining sea ice samples at higher analysis temperatures that is closer to *in situ* temperatures will minimize the effects of low temperature storage on the sea ice inclusions.

Acknowledgements

I would like to thank and acknowledge my supervisor, Dr Tokoloho Rampai, whose guidance, support and expertise have been invaluable to me throughout this project. Her mentorship and insight has shaped my understanding and approach to sea ice research.

To Prof. Marcello Vichi and Robyn Verrinder for their leadership and support on the SCALE winter 2022 cruise and throughout this academic journey.

To the captain and crew of the *S.A. Agulhas,* who navigate the Southern Ocean to assist us with the field work that would not have been possible without them.

To the technical staff, Curwin, Ameen, Colm and Paul at both UCT and X-sight for their assistance and expertise over the duration of this project.

I am deeply grateful to my family for their unwavering support and encouragement throughout my Master's degree. Their understanding and belief in me have been a great comfort during challenging times. Mom, dad, Jade and Carly, I am forever grateful for your unwavering support.

I am immensely thankful to my work colleagues in my research group, who I am lucky to also call friends. Safiyyah and James, you have made filled some of the toughest times with joy and laughter which has given me the motivation throughout this project. To Bongani, Mufudzi and Jenna thank you for all the encouragement and always checking in.

To Agi, Ash, Dayna, Riesna, Justin, Lawrence, Siobhan and Felix, the incredible people with whom I have formed friendships on winter 2022 cruise. You have not only shared your knowledge, but also working spaces, snacks, tea-breaks, tears and laughs.

I am grateful to the National Research Foundation (NRF) and the University of Cape Town (UCT) for the financial support of my project and degree.

Table of Contents

List of Figures vi

List of Tables ix

List of Equations x

Glossary xi

Nomenclature and Abbreviations xii

1 Introduction 1

2 Literature Review 2

2.1 Sea Ice Growth Drivers and Ice Types 2

2.2 Sea Ice Texture 3

2.3 Sea Ice Inclusions 5

2.3.1 Air inclusions 5

2.3.2 Brine inclusions 8

2.4 Analysis of Sea Ice Texture and Structural Properties 16

2.4.1 X-ray Computed Tomography Scanning 17

2.4.2 Methodological Limitations of Microstructural Analysis Methods 20

2.5 Rationale of Study 22

3 Research Objectives 24

3.1 Research aim and objectives 24

3.2 Scope of study 24

4 Methodology 25

4.1 Sample Collection, Physical Property Measurements and Analytical Methodology for Sea Ice Texture and Microstructure 25

4.1.1 Sample Collection Locations 25

4.1.2 Pancake Sample Collection and Safety Protocols 26

4.1.3 Temperature and Salinity Measurements of Cores 29

4.2 Textural and Structural Analysis 30

4.2.1 Cross Polarisation Methodology 30

4.2.2 X-ray Computed Tomography Methodology 31

4.2.2.1 X-ray Computed Tomography Sample Preparation 31

4.2.2.2 Sample Preparation for Directional Heating Analysis 33

4.2.2.3 Density Measurements of μCT Scanned Samples....35
4.2.2.4 X-ray Computed Tomography Imaging Methodology....35
4.2.2.5 X-ray Computed Tomography Post Image Processing....37
5 Data Analysis and Results....40
5.1 Textural Analysis....40
5.2 Microstructural Analysis....41
5.2.1 Data Analysis for μCT Scan Results....42
5.2.1.1 Inclusion Analysis Limitations....42
5.2.1.2 Noise Filtering....43
5.2.1.3 Inclusion Characterisation....44
5.2.1.4 CT based Salinity and Density Measurements....47
5.2.1.5 Statistical Analyses....50
5.2.2 Directional Heating Results....50
5.2.3 Comparison of Winter 2019 and 2022 Protocols and Results....63
5.2.4 Spatial variability of inclusions profiles in a pancake floe....71
6 Overall Discussion....76
7 Conclusions and Recommendations....78
7.1 Conclusions....78
7.2 Recommendations....79
8 References....80
Appendix A: Ethics Clearance....88
Appendix B: Physical Property Results....89
Appendix C: Cross Polarisation Images....91
Appendix D: Heat Transfer Calculations for UD and MD Heating....97
Appendix E: UD and MD Heating Additional Results....99
Appendix F: Statistical Analysis Results....104
Appendix G: Images and Additional Results from CT Scans....106

List of Figures

Figure 2.1: Sea ice growth in different conditions (adapted from European Space Agency, 2016) (top), photograph of Antarctic pancake ice (Zicus, 2017) (A) and photograph of thin nilas ice (Scott & Hansen, 2016) (B) 3
Figure 2.2: Ice crystal structure with the c-axis [0001] indicated (Weeks & Ackley, 1982) 4
Figure 2.3: Schematic of the profiles of typical sea ice (Petrich & Eicken, 2017) 5
Figure 2.4: Phase diagram of sea ice based on a closed volume of standard sea water at different temperatures (Assur, 1960) 8
Figure 2.5: Freezing point of brine as a function of the ratio of dissolved salts to pure water (Assur, 1960) 11
Figure 2.6: Illustration of a warming sequence (a-c) and cooling (d) on a sea ice brine and air inclusions (Light, Maykut & Grenfell, 2003) 14
Figure 2.7: Schematic representation of the formation of brine pockets from brine cylinders during cooling (Grenfell, 1983) 15
Figure 2.8: Thresholding a trinary image of sea ice (grey), brine (white) and air (black) (Lieb-Lappen, Golden & Obbard, 2017) 18
Figure 2.9: CT scan image with highlighted air inclusions (Crabeck et al., 2016) 18
Figure 2.10: Otsu's method applied with and without a Gaussian filter (OpenCV, 2022) 19
Figure 2.11: Example of global and local thresholding (Gonzalez, 2015) 19
Figure 2.12: Representative histogram for thresholding (Lieb-Lappen, Golden & Obbard, 2017) 20
Figure 4.1: Pancake floes collection locations for winter 2019 (left) and winter 2022 (right) expedition with sea ice concentration shown for the 27th July 2019 and 24th July 2022 respectively 26
Figure 4.2: Photograph taken during the winter 2022 expedition of pancake collection in progress with the wooden slates shown where the floes are placed 27
Figure 4.3: Photographs of the pancake floes (left) with their corresponding schematics (right) of the coring locations from the pancake floes collected at 19WMIZ1 (top) and 22WMIZ3 (bottom) (Photographs from winter 2019 from Lin (2022) and winter 2022 from Agoritsa Spirakis) 28
Figure 4.4: Schematic diagram showing how a core sample was cut to produce a section of sea ice for cross polarisation 31
Figure 4.5: Schematic diagram showing how a core sample was cut to produce a section of sea ice for CT scanning 32
Figure 4.6: Schematic of UD and MD sample depth selection 33

Figure 4.7: Styrofoam holder used to promote a heat flux through the vertical axis of sea ice CT samples 34
Figure 4.8: Cooling chamber for sea ice samples in the CT scanner 36
Figure 5.1: Stratigraphy diagrams for sea ice core collected from pancake floes collected during the winter 2019 and 2022 41
Figure 5.2: Average crystal size profile with 95% confidence intervals of cores collected during winter 2019 and 2022 41
Figure 5.3: Effect of filtering inclusions based on the inclusion voxel count 44
Figure 5.4: Effect of tube size parameter (mm) on the brine tube porosity (left) and number densities (right) 45
Figure 5.5: Number densities of brine tube inclusions that have projected lengths dimensions over 1 mm on the X, Y, Z or combination thereof axes 46
Figure 5.6: Salinity profiles of the winter 2019 cores based on conductivity measurements (A3, A4 and A5) and salinity derived from CT-based brine and air volumes 48
Figure 5.7: Density profiles of the winter 2022 B1 core for density based on cuboid dimensions and weighting (blue) and the density based on the brine and air volumes observed in CT analyses. 49
Figure 5.8: Effects of heating on the total porosity of sea ice from the top, middle and bottom section of an ice core 51
Figure 5.9: Effects of heating on the brine and air porosities from a top, middle and bottom section of an ice core 52
Figure 5.10: Effects of heating on the number of brine and air inclusions from a top, middle and bottom section of an ice core 54
Figure 5.11: Histograms of brine inclusion volume distributions for the top, middle and bottom sections with different heating methods 56
Figure 5.12: Box and whisker diagram of brine inclusion volume distribution 57
Figure 5.13: Box and whisker diagrams of brine inclusion projected length distributions 58
Figure 5.14: Effects of heating on the sphericity of all the brine inclusions from a top, middle and bottom section of an ice core 60
Figure 5.15: Effects of heating on the air porosity and number densities of the micro, large and macro air inclusions from a top, middle and bottom section of an ice core 61
Figure 5.16: Temperature profiles of cores collected from the winter 2019 (A3-A5) and winter 2022 (B6-B8) pancakes 64
Figure 5.17: Brine and air porosity (left) and number density (right) profiles of cores collected from the winter 2019 (A1) and winter 2022 (B1) pancakes 67
Figure 5.18: Sphericity distribution of brine inclusions within the B1 (top) winter 2022 core and A1 (bottom) winter 2019 core at varying depths 69

Figure 5.19: Histograms of brine inclusion volume distributions for the winter 2022 (top) and winter 2019 (bottom) at varying depths (cm) 70
Figure 5.20: Profile of brine (left) and air porosities (right) from a single pancake floe at varying locations within the floe collected during winter 2022 72
Figure 5.21: Inclusion number density profiles of brine and air of ice cores from the winter 2022 at varying locations within a pancake floe.....73
Figure C.1: Cross-polarised images from A2 core of the winter 2019 expedition, photo's ordered from 4 to 1 respectively 91
Figure C.2: Cross-polarised images from B4 core of the winter 2022 expedition, photo's ordered from 5 to 1 respectively 93
Figure C.3: Cross-polarised images from B5 core of the winter 2022 expedition, photo's ordered from 6 to 1 respectively 95
Figure D.1: Estimated temperature of the ice over the heating periods of UD and MD heating 98
Figure E.1: 2D Greyscale images from CT scans of the heating methods applied to ice sections.....99
Figure E.2: 3D reconstruction of the brine inclusions from CT scans of the heating methods applied to ice sections.....100
Figure E.3: 3D reconstruction of the air inclusions from CT scans of the heating methods applied to ice sections.....101
Figure E.4: Effects of heating on the sphericity of all the air inclusions from a top, middle and bottom section of an ice core 103
Figure G.1: Greyscale CT Images (left), 3D reconstructions of the brine (middle) and air (right) phases of the A1 winter 2019 CT core.....107
Figure G.2: Greyscale CT Images (left), 3D reconstructions of the brine (middle) and air (right) phases of the B1 winter 2022 CT core.....110
Figure G.3: Greyscale CT Images (left), 3D reconstructions of the brine (middle) and air (right) phases of the B2 winter 2022 CT core.....112
Figure G.4: Greyscale CT Images (left), 3D reconstructions of the brine (middle) and air (right) phases of the B3 winter 2022 CT core.....115

List of Tables

Table 2.1: Comparison of brine number densities on a volume basis in sea ice 13
Table 4.1: Summary of weather conditions at ice stations on the winter 2019 and 2022 expeditions 26
Table 4.2: Overview of stations, core IDs, testing designations and core depths (TS - temperature and salinity, CT – μCT scanning, XP- cross polarization) 29
Table 5.1: Summary of the average granular crystal sizes with the 95% confidence interval for the winter pancake ice from 2019 and 2022 40
Table 5.2: Average brine and air porosities of cores from winter 2019 (A1) and winter 2022 (B1) 65
Table 5.3: Average brine and air number densities through the depth of cores from winter 2019 (A1) and winter 2022 (B1) 68
Table 5.4: Average brine and air porosities of cores from a single pancake flow collected during winter 2022 73
Table 5.5: Average brine and air number densities through the depth of cores from winter 2022 74
Table B.1: Temperature measurements from the winter 2019 pancake 89
Table B.2: Temperature measurements from the winter 2022 pancake 89
Table B.3: Salinity measurements from the winter 2019 pancake 90
Table B.4: Dimension, mass and density measurements of the winter 2022 B1 core 90
Table C.1: Crystal size measurements of 20 random crystals from each cross-polarised image for the winter 2019 A2 core 92
Table C.2: Crystal size measurements of 20 random crystals from each cross-polarised image for the winter 2022 B4 core 94
Table C.3: Crystal size measurements of 20 random crystals from each cross-polarised image for the winter 2022 B5 core 96
Table E.1: Data generated from CT scans of the UD and MD heating study 102
Table F.1: Two-Factor ANOVA without replication associated with total porosity of the original, UD and MD samples of the low temperature and heating method sequence 104
Table F.2: Two-Factor ANOVA without replication associated with brine porosities of the original, UD and MD samples of the low temperature and heating method sequence 104
Table F.3: Two-Factor ANOVA without replication associated with brine porosities between the different heating methods 104
Table F.4: Two-Factor ANOVA without replication associated with air porosities of the original, UD and MD samples of the low temperature and heating method sequence 104

Table F.5: Two-Factor ANOVA without replication associated with brine number densities of the original, UD and MD samples of the low temperature and heating method sequence..105
Table F.6: Two-Factor ANOVA without replication associated with air number densities of the original, UD and MD samples of the low temperature and heating method sequence.....105
Table F.7: Two-Factor ANOVA without replication associated with brine horizontal projected dimensions of the original, UD and MD samples of the low temperature and heating method sequence 105
Table F.8: Two-Factor ANOVA without replication associated with brine horizontal projected dimensions between the different heating methods.....105
Table F.9: Two-Factor ANOVA without replication associated with brine vertical projected dimensions of the original, UD and MD samples of the low temperature and heating method sequence 105
Table G.1: Data generated from CT scans of the winter 2019 A1 core.....116
Table G.2: Data generated from CT scans of the winter 2022 B1 core.....116
Table G.3: Data generated from CT scans of the winter 2022 B2 core.....117
Table G.4: Data generated from CT scans of the winter 2022 B3 core.....118
Table G.5: Summary of winter 2019 vs 2022 results.....118

List of Equations

Equation 1.....9
Equation 2.....9
Equation 3.....9
Equation 4.....9
Equation 5.....35
Equation 6.....39
Equation 7.....39
Equation 8.....47
Equation 9.....47
Equation 10.....48
Equation 11.....48
Equation 12.....48
Equation 13.....97
Equation 14.....97
Equation 15.....97

Glossary

Austral	Relating to the Southern Hemisphere
Congelation growth	Ice crystal growth in the basal plane at the bottom of an ice surface
Convection	The transfer of heat and salt in a fluid due to temperature driven density differences
Floe	A sheet of floating ice
Frazil ice	Individual ice crystals suspended near the surface of water
Freeboard	The distance between the water level and upper surface of the ice
Grease ice	Smooth thin flat ice form during calm conditions
Heterogenous	Diverse in phase or characteristics
In situ	Property in its natural environment
Marginal Ice Zone	Region of sea ice that is influenced by the ocean generally considered regions of 10-80% sea ice concentrations
Morphology	Referring to the shape of an object
Nucleation	Initial process in the formation of ice crystals or bubbles
Pancake ice	Disc-shaped ice floes formed in turbulent ocean conditions
Percolation	Movement and filtering of fluids through a porous material
Permeability	The ability of a material to allow a substance through it
Sphericity	A measure of the surface area of a sphere with the same volume of an object to the actual surface area of the object
Supersaturation	A non-equilibrium state where the concentration is beyond the point of saturation
Thermohaline circulation	Sea water movement due to temperature differences causing changes in salt concentrations and density
Thresholding	A value or boundary at which conditions are set e.g. true or false
Voxel	3D pixel

Nomenclature and Abbreviations

$\emptyset_{b/i/a}\ or\ V_{b/i/a}$	Brine/ice/air (b/i/a) Porosity/Volume
$S_{br}\ or\ S_{bu}$	Interstitial brine or bulk Salinity
T	Temperature
ρ	Density
m	Mass
V	Volume
A	Surface Area
PSU	Practical Salinity Units
MIZ	Marginal Ice Zone
UTC	Coordinated Universal Time
$\delta^{18}O$	Standard oxygen 18 isotope
Q	Heat flux
h	Convective heat transfer coefficient of air
C_p	Heat capacity
t	Time
k	Thermal conductivity
L	Length

1 Introduction

Sea ice has a high albedo that reflects incoming solar radiation and aids in regulating global climate, its microstructure contributes to this effect (Untersteiner, 1961; Grenfell, 1983; Perovich, 2017). The microstructure also affects the substantial gas fluxes that occur at the sea ice-atmosphere interface (Gosink, Pearson & Kelley, 1976; Semiletov et al., 2004; Delille et al., 2014). The microstructural properties of sea ice have cascading effects onto larger scale systems and vice versa through feedback mechanisms. The heat, momentum and mass transfer between the ocean and the atmosphere is influenced by the seasonal cycles of sea ice growth and retreat (Allison, 1997; Eayrs et al., 2019). Salt expelled from growing ice cover impacts the thermohaline circulation (Keeling & Stephens, 2001; Petrich & Eicken, 2017). Highly saline liquid and air inclusions are formed within the sea ice structure due to the rejection of salts from the crystallising ice (Weeks & Ackley, 1982; Middleton et al., 2016) and the reduced solubility of gases in growing sea ice (Tsurikov, 1979; Crabeck et al., 2016). The turbulent nature of the Antarctic marginal ice zone (MIZ) , compared to the Arctic, Ross Sea and Weddell Sea (Gow et al., 1982), influences the growth dynamics (Weeks, 2010) and thus the texture and microstructure of the sea ice (Eicken, 2003). The dynamic Antarctic MIZ results in a higher degree of spatial and temporal variability within the sea ice (Vichi et al., 2019).

In order for climate models to better represent the Antarctic MIZ conditions, datasets of the microstructural properties of sea ice from these regions are required to validate these models. Temperature is a factor that greatly influences the microstructural properties of sea ice. Sea ice samples are typically stored at approximately -20°C, lower than *in situ* temperatures, and later heated to higher temperatures (~-10°C) to comply with standard testing conditions. Investigating the microstructure of sea ice is essential to understanding of the mechanisms influencing larger scale systems their feedback mechanisms. A major challenge to that investigation is the storage conditions of samples effecting properties of the microstructure that are not the same as *in situ*, for which there is no complete description of these effects.

The aim of this study was to investigate the impacts of low temperature storage and subsequent heating effects on liquid and air inclusions on sea ice samples from the Antarctic MIZ. In addition, the optimisation of sampling and storage protocols for the sea ice were investigated during the winter 2022 expedition and compared to the winter 2019 expedition. These optimised protocols and temperature impact investigations were used to evaluate the spatial variability of sea ice inclusions within a single pancake floe. This study was carried out using non-destructive X-ray computer tomography (CT) analysis.

2 Literature Review

2.1 Sea Ice Growth Drivers and Ice Types

The Antarctic continent is surrounded by an ocean, in contrast to the Arctic which is surrounded by land. The Antarctic experiences more turbulent conditions as it is exposed to large winds and ocean currents of the Southern Ocean (Maksym, 2019; Vichi et al., 2019). The exposure to these large waves and winds significantly impacts the growth dynamics and extent of first year sea ice in the Southern Ocean.

Dynamic and thermodynamic factors are the two main drivers of sea ice growth. These can be distinguished by the ocean dynamics (Haas, 2003; Petrich & Eicken, 2017). Grease ice solidifies in clam conditions before the onset of congelation growth which forms a smooth bottomed ice sheet (Weeks, 2010; European Space Agency, 2016). Rough ocean conditions favour the formation of frazil ice. Frazil ice in these conditions coagulate and solidify to form what is called pancake ice (Wadhams, Lange & Ackley, 1987) while polynyas develop as areas of open water amidst the surround sea ice. This can be described as large disk-shaped floes with raised edges (Figure 2.1-A) due wind action and ocean swelling that causes pancakes floes to collide against one another (Wadhams, Lange & Ackley, 1987; Petrich & Eicken, 2017). The pancake floes agglomerate over time to form larger pancakes that eventually consolidate to form a continuous ice floe which can have varying ice depths (Wadhams, Lange & Ackley, 1987; European Space Agency, 2016). Continuous solid ice sheets resulting from the consolidation of many individual pancakes can be composed of stacked or tiled pancakes due to rafting and ridging behaviour (Lange et al., 1989).

Sea ice concentration (SIC) refers to the percentage coverage of an area by sea ice. There are regions in the Antarctic MIZ of 100% SIC, however, this does not denote a consolidated ice field as 100% coverage can also be interstitial frazil ice occupying space between pancake floes (Vichi et al., 2019). The heat, momentum and material fluxes of consolidated ice compared to pancake ice with interstitial frazil ice vary greatly (Matsumura & Ohshima, 2015; Vichi et al., 2019), although both conditions denote 100% SIC. Thus climate models may not provide an accurate representation of sea ice interactions in these differing regions of similar SIC without consideration for the ice types. The dynamic conditions in the Southern Ocean near the Antarctic MIZ result in large areas of unconsolidated ice with 100% SIC due to waves that propagate deep into the ice (Vichi et al., 2019). In addition, there is limited data on pancake ice properties from the Antarctic MIZ, necessitating the need for more data to aid in

understanding the development of sea ice growth in the Antarctic MIZ (Skatulla et al., 2022) and the impact on it microstructural properties.

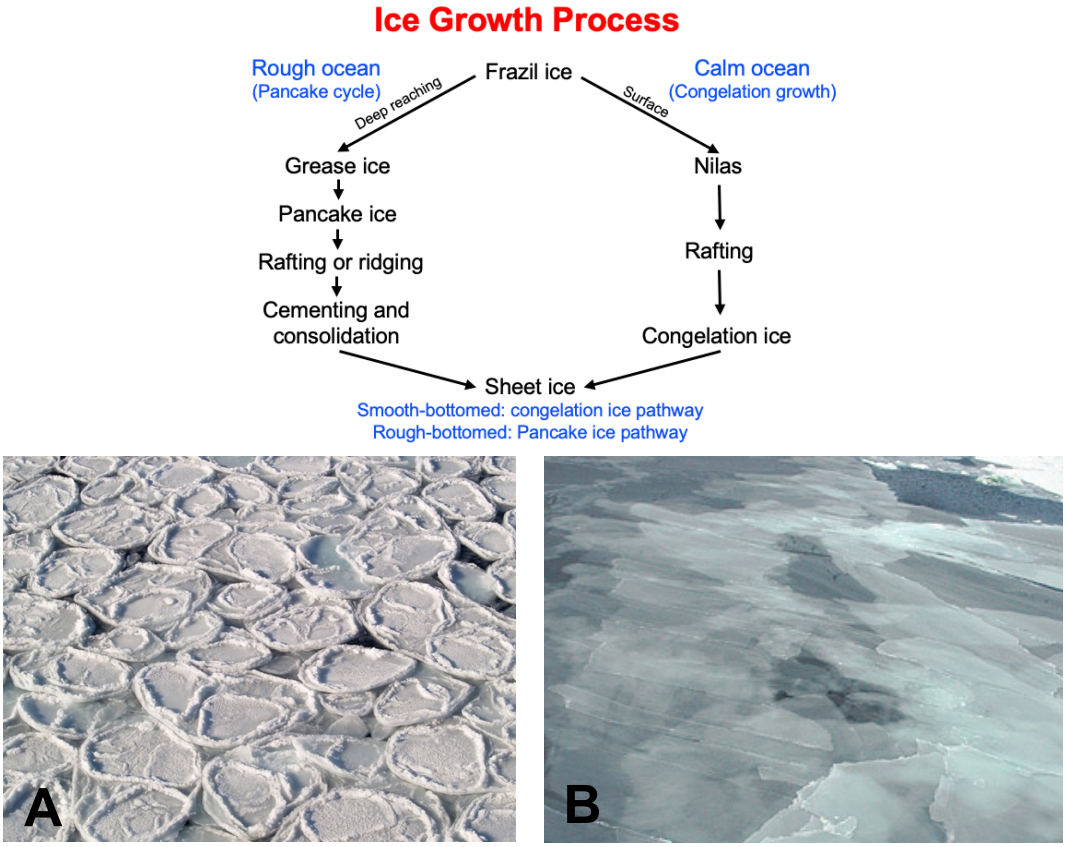


Figure 2.1: Sea ice growth in different conditions (adapted from European Space Agency, 2016) *(top), photograph of Antarctic pancake ice* (Zicus, 2017) *(A) and photograph of thin nilas ice (Scott & Hansen, 2016) (B)*

2.2 Sea Ice Texture

Ice formation commences when the entire mixed layer near the surface of the ocean is cooled to its freezing point (Petrich & Eicken, 2017). The crystal lattice structure of sea ice rejects salt components found in the ocean water, and this phenomenon shapes the microstructure and properties of sea ice which distinguishes sea ice from fresh water ice (Petrich & Eicken, 2017). The abundance of impurities in the ocean allows for a sufficient number of nucleation sites for crystal formation once the freezing temperature of the water is reached (Weeks, 2010). Ice crystals initially form into needles, spicules or platelet shapes that resemble slush (frazil ice) (Weeks, 2010; Petrich & Eicken, 2017). Frazil ice crystals that grow near the air-ocean interface have randomly orientated c-axes (Figure 2.2). The ice becomes shielded from the winds as more ice crystals develop, coagulate and form solid ice structures. Ice crystals with

a horizontally orientated c-axis then begin to dominate (in calm ocean conditions) due to the higher growth rates in the basal plane (Hobbs, 2010).

The ice growth the ice-water interface progresses downwards with salt ions being rejected from the crystal lattice structure of ice (Middleton et al., 2016). A diffusion layer of salt ions form at the advancing front of the ice-water interface (Petrich & Eicken, 2017). The diffusion of the salt ions is slower than the heat flux from the warmer ocean to the colder ice-ocean interface. This results in the formation of a super-cooled layer along the salt enriched ice-water interface which distinguishes the crystallographic properties of sea ice (Weeks, 2010; Petrich & Eicken, 2017).

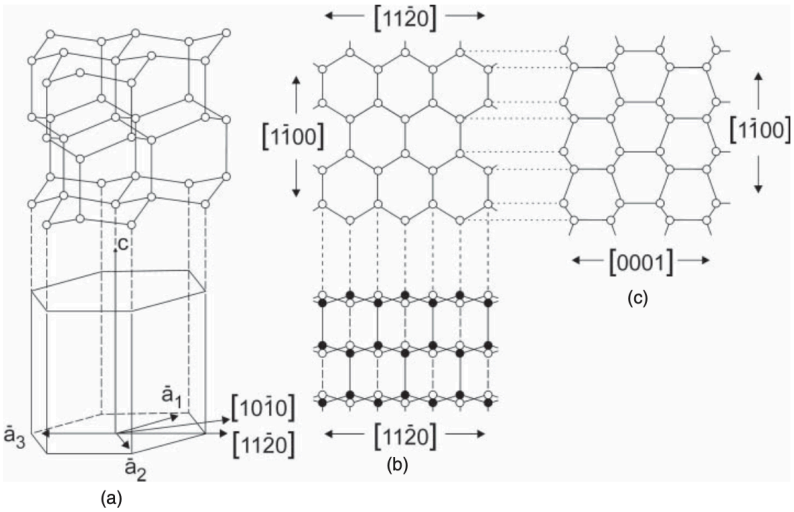


Figure 2.2: Ice crystal structure with the c-axis [0001] indicated (Weeks & Ackley, 1982)

The arrangement, shape and size of the ice crystals can describe the texture of the ice (Eicken & Lange, 1989). Smaller randomly orientated crystals typically occupy the upper section of the sea ice profiles (for thermodynamically grown ice) which is referred to as granular in texture (Weeks, 2010; Petrich & Eicken, 2017). Granular ice can then further be classified into polygonal and orbicular granular ice which can be distinguished by the $\delta^{18}O$ values (Allison & Worby, 1994). Polygonal granular ice has large planar crystals formed in warmer temperatures when surface snow melts and percolates through the colder snow and refreezes becoming superimposed ice. Orbicular granular ice has smaller and more rounded crystals that can form from the agglomeration of frazil ice (Eicken & Lange, 1989) or the flooding of the surface snow ice and its subsequent refreezing, called snow ice (Lange et al., 1990). Transitional textured ice is a mixture of granular and columnar textures with some crystals starting to become elongated. Columnar texture of sea ice can generally be defined by larger crystals with the c-axes of the ice crystal horizontally orientated, producing vertically elongated crystals (Weeks

& Ackley, 1982). A typically profile of sea ice stratigraphy, salinity and temperature is illustrated in Figure 2.3, for sea ice growth in relatively clam ocean conditions.

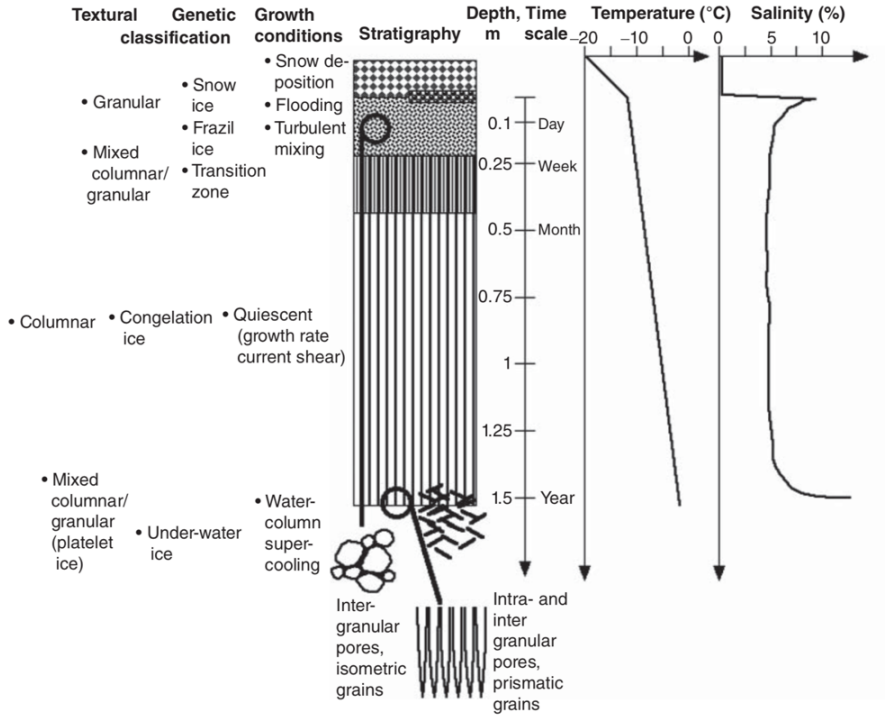


Figure 2.3: Schematic of the profiles of typical sea ice (Petrich & Eicken, 2017)

2.3 Sea Ice Inclusions

Sea ice contains highly saline liquid inclusions and air inclusions within the ice structure. These inclusions and their morphology are influenced by the temperature, salinity and texture of the ice (Crabeck et al., 2016; Oggier & Eicken, 2022). Sea ice has unique characteristics due to these inclusions that influence its physical, mechanical, optical and electromagnetic properties (Assur, 1960; Perovich & Grenfell, 1981; Grenfell, 1983; Crabeck et al., 2016).

2.3.1 Air inclusions

Sea ice was previously considered an insulator for CO_2 exchange between the ocean and atmosphere with gas components assumed be only dissolved in brine and therefore subject to the same processes (Nomura, Yoshikawa-Inoue & Toyota, 2006; Crabeck et al., 2014). It was further assumed that air porosity (air volume fraction) in ice was minor in comparison to brine porosity (brine volume fraction) and was consequently neglected from mushy layer equations (Worster, 1992; Feltham et al., 2006). Unlike ice formed from freshwater, sea ice is highly permeable at surface temperatures above -5°C, which permits gas exchange through

the ice (Gosink, Pearson & Kelley, 1976; Golden, Ackley & Lytle, 1998). Although air porosity has been considered negligible, more recent studies have reported substantial CO_2 fluxes at the ice-atmosphere interface (Semiletov et al., 2004; Nomura, Yoshikawa-Inoue & Toyota, 2006; Delille et al., 2014).

Sea ice provides a medium in which a multitude of factors that favour bubble nucleation are met. Bubble nucleation tends to occur outside thermodynamic equilibrium due to heterogenous supersaturation (Roedder, 1972; Li & Yortsosa, 1994) or in regions of structural irregularities on heterogenous surfaces that can have inhomogeneities either geometrically, structurally or chemically (Kožíšek, Demo & Sato, 2000). Therefore while sea ice provides several factors that favour nucleation of air inclusions, there are various processes that govern the formation of these resulting air inclusions.

Tsurikov (1979) first described three main process types involved in the formation of gas inclusions within sea ice: syngenetic, epigenetic and exogenetic. These relate to phenomena occurring under, within and at the upper boundary of the sea ice itself respectively. The main contributor to air inclusion formation in sea ice is attributed to brine reduction by freezing (Zhou et al., 2013; Crabeck et al., 2016). The solubility of gas reduces with decreasing temperature and increasing salinity. Once the sum of the partial pressure of the dissolved gases within the brine becomes greater than the local hydrostatic pressure, an air inclusion forms within the ice (Zhou et al., 2013; Crabeck et al., 2016) which is termed solubility-driven nucleation.

Other epigenetic processes of air inclusion formation in sea ice include the substitution for air during brine drainage (above the ice freeboard) during a melting period, the formation of water-vapour filled air pores due to partial evaporation of ice and brine during melting periods due to the lower density of ice than water and algae within the ice producing oxygen during photosynthesis resulting in the formation of air inclusions (Tsurikov, 1979). Convection-driven nucleation refers to the formation of bubble due to the movement of fluid cause by density differences, often driven by temperature gradients, that has been used to describe the appearance of micro air inclusions in subsaturated regions of sea ice (Crabeck et al., 2016). Syngenetic processes result in air inclusions in sea ice is due to the entrapment of gas, from both the ocean and atmosphere, in loose crystals such as frazil ice that have not frozen together (Tsurikov, 1979; Crabeck et al., 2016). Exogenetic processes can include the capturing of air inclusions during snow ice formation and migration of air inclusions, from the snow cover into the underlying ice, in the opposite direction of the heat flow (Tsurikov, 1979).

Crabeck et al. (2016) concluded that the processes governing the vertical distribution of salt does not control the vertical distribution of gases within sea ice as most of the gas is not dissolved within the brine as previously thought (Tison et al., 2002; Zhou et al., 2013; Crabeck et al., 2014). Once an air inclusion forms, it is are no longer subject to the same transport mechanisms as dissolved salt. Air porosity profiles have shown decreasing porosity with depth and total gas content has been shown to increase over time (Crabeck et al., 2016; Salomon, Maus & Petrich, 2021). Granular textured ice near the ice ocean interface contained the highest air porosities with macro (>5mm) air inclusions found exclusively in this region for thermodynamically grown ice. These upper regions of the ice also contained air volume fractions greater than the concentrations at saturation and thus were termed supersaturated regions (Crabeck et al., 2016). Lower depths noted lower air porosities that exclusively contained large (< 5mm & > 1mm) and micro (< 1mm) air inclusions, however, the air porosity values determined through CT analysis were greater than the calculated theoretical atmospheric concentrations therefore these had to be subsaturated regions. This leads to the conclusion that convection-driven nucleation resulted in air inclusion formations in subsaturated regions of the ice (Crabeck et al., 2016).

Since air porosity has received little attention in comparison to brine porosity, there are limited studies of the impacts of temperature changes on the air phase of sea ice. During a cooling cycle of ice, these conditions of temperature reductions and increasing salinity (due to local brine salinity increasing) are met for air inclusions formation. Conversely the shrinking and disappearance of air inclusions has been observed in cooling sequences (Light, Maykut & Grenfell, 2003). Over a period of heating, melting occurs on the walls of the brine inclusions but the density of the melted ice is higher than that of the solid ice, theorising the formation of air inclusions as a result of these volume differences between the liquid and solid phases (Tsurikov, 1979; Cox & Weeks, 1986). Light, Maykut & Grenfell (2003) surprisingly observed no nucleation of new air inclusions during a heating sequence, as has been observed in some studies, suggesting air inclusion formation may be energetically unfavourable in metastable liquids (Roedder, 1972; Li & Yortsosa, 1994).

Crabeck et al. (2016) suggested that the air porosity in sea ice is a function of the brine porosity and bulk ice gas saturation. Cox & Weeks (1983) developed equation for determining air porosity using density, salinity and temperature measurements. Additionally, studies on the morphology of air inclusions have been sparse despite the vital role this plays in properties and processes associated with sea ice (Light, Maykut & Grenfell, 2003; Crabeck et al., 2016; Perovich, 2017). The porosity and the morphology of air inclusions in sea ice affects its thermal properties (Cox & Weeks, 1988; Worster & Wettlaufer, 1997; Petrich & Eicken, 2017). The

presence of inclusions within the ice matrix enhances its insulation capacity, reducing the heat transfer through the ice (Cox & Weeks, 1988; Worster & Wettlaufer, 1997; Notz & Worster, 2009; McPhee, 2017). This has implications for the energy balance of the polar regions, as sea ice acts as a thermal barrier between the cold atmosphere and the relatively warmer ocean waters below (Allison, 1997; Sandven & Johannessen, 2006; McPhee, 2017).

2.3.2 Brine inclusions

Sea ice formation is dictated by freezing equilibrium chemistry due to the presence of salt ions in the ocean, as such the freezing point of the ocean is lower than that of pure water (Petrich & Eicken, 2017). While many properties of sea ice have be observed through the observation of a binary mixture of NaCl (Petrich & Eicken, 2017), a more complex phase relationship occurs during freezing of ocean water (Assur, 1960). Ocean water is a mixture of many salts mainly consisting of sodium, chloride, sulphate, magnesium, calcium and potassium ions (Petrich & Eicken, 2017). Figure 2.4 depicts the weight ratio of ice, brine and salts that begin to precipitate at different temperatures.

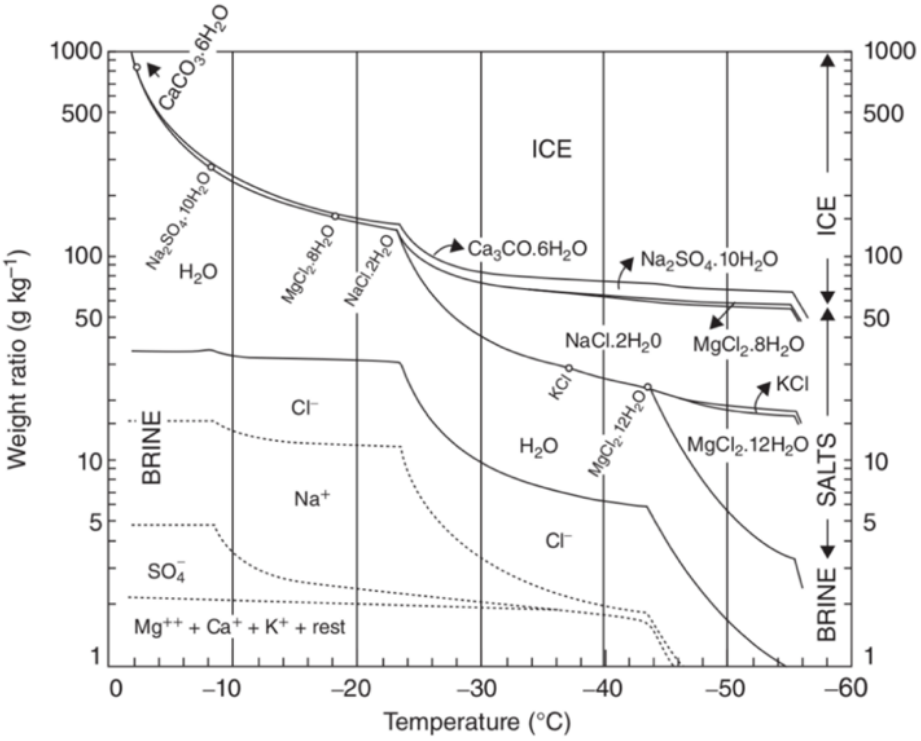


Figure 2.4: Phase diagram of sea ice based on a closed volume of standard sea water at different temperatures (Assur, 1960)

The crystal lattice structure of ice rejects the incorporation of salt ions (Figure 2.2) which results in the accumulation of these salts in the liquid phase (Lofgren & Weeks, 1969; Weeks,

2010; Middleton et al., 2016; Oggier & Eicken, 2022). The liquid phase is in thermodynamic equilibrium with the surrounding solid phase due to the accumulation of these salts in the highly saline liquid, called brine. The brine inclusions are more saline than the underlying ocean, and consequently is a more dense liquid. Therefore gravity drainage results in a measurable salt flux from the ice into the ocean during sea ice growth through brine channels (Notz & Worster, 2009). Other desalination mechanisms occur such as the rejection of salt at the ice-ocean interface, brine expulsion and diffusion, however, these are not considered significant (Notz & Worster, 2009). This results in the bulk salinity of ice being lower than that of the underlying ocean (Figure 2.3).

Lofgren & Weeks (1969) discuss that once a continuous layer of ice has formed and thermodynamic growth of ice has commenced, ice plate at the ice-water interface form regular protuberances during the growth that result in the entrapment of brine inclusions along these substructures. The average width between these substructures called plates is influenced by growth velocity which shows an increasing width with decreasing velocity. The growth velocity tends to decrease with depth, in thermodynamically grown sea ice, thus there is an increase in plate spacing with depth (Weeks & Hamilton, 1962; Lofgren & Weeks, 1969). The total amount of brine entrapped within the ice is influenced by the plate size and geometry. Frankenstein & Garner (1967) (Equation 1, Equation 2 and Equation 3) and Cox & Weeks (1983) (Equation 4) have developed equations for determining the brine volume of sea ice based on temperature, bulk salinity and bulk density.

$$\emptyset_b = S\left(\frac{52.56}{\mathrm{T}} - 2.28\right) \quad for\ -0.5°C \leq \mathrm{T} \leq -2.06°C \qquad \textit{Equation 1}$$

$$\emptyset_b = S\left(\frac{45.917}{\mathrm{T}} + 0.930\right) \quad for\ -2.6°C \leq \mathrm{T} \leq -8.2°C \qquad \textit{Equation 2}$$

$$\emptyset_b = S\left(\frac{43.795}{\mathrm{T}} + 1.189\right) \quad for\ -8.2°C \leq \mathrm{T} \leq -22.9°C \qquad \textit{Equation 3}$$

$$\frac{V_\mathrm{b}}{V} = \frac{\rho S_\mathrm{i}}{\rho_\mathrm{b} S_\mathrm{b}} \qquad \textit{Equation 4}$$

The equations developed by Frankenstein & Garner (1967) were based on the Assur's (1960) table which give the relative volume of brine in standard sea ice of 1‰ depending on temperature. Assur's (1960) table was computed from the phase relations of standard sea ice (Figure 2.4) and values derived from the freezing point of brine. The phase relations data is predominantly based on experimental derivations from Nelson and Thompson (1954) and Ringer (1928; cited in Assur, 1960). Standard sea ice was assumed as the salinity of 34.325‰ was used that corresponds to normal sea water (Assur, 1960).

Assur's (1960) table of relative brine volume along with Frankenstein and Garner's (1967) equations assume a constant ice density of 926 kg/m^3 which corresponds to a salinity of 6‰ and -10°C (Assur, 1960). This assumption was based on the theoretical densities of sea ice varying slightly with salinity and temperature. This allowed for the simplification of the equation for the brine porosity to be strictly proportional to the salinity (Frankenstein & Garner, 1967).

A relationship between the salinity of the brine within sea ice to the freezing point can be determined as the brine and ice are in phase equilibrium. Therefore, the solid phase temperature is equal to that of the liquid phase (Notz, 2005), which is the freezing temperature of the multi-component system. This means a relationship for the salinity of the brine can be derived from the present freezing point. A correlation between the ratio of dissolved salts to the pure water component, on a weight basis, against the freezing temperature can be linearised within select ranges of temperature, as can be seen in Figure 2.5. Assur (1960) described the ratio of dissolved salts to pure water as the proper parameter, stating that the use of chlorinity or salinity in its usual definition would be too empirical, thus, the ratio as previously described was used by Assur (1960).

It can be seen in Figure 2.5 that a break in the linear correlation can be seen, this is due to the precipitation of $Na_2SO_4.10H_2O$ occurring around -8°C. A new linear correlation is formed continuing until -23°C, below such temperature $NaCl.2H_2O$ begins to precipitate (Assur, 1960). The segments of linear correlations between freezing point and brine salinity links to the temperature conditions for the set of equations derived by Frankenstein and Garner (1967). Assur derived a correlation from a least squares analysis used to minimise the absolute errors that is used in Frankenstein and Garner's (1967) derivations.

Cox and Weeks (1983) also derived equations for brine porosity (Figure 2.4) based on the bulk density of the sample being incorporated. These equations were also derived on Assur (1960) phase equilibrium phase tables. Cox and Weeks (1983) incorporates the presence of salts into their derivation assuming a constant solid salt density of 1500 kg/m^3 and compared their results to previously published work, determining that neglecting the presence of solid salts in the derivations proved to be a reasonable assumption.

Sea ice microstructure is an important aspect of the physical properties of the ice and the biogeochemical transformation and cycling of the ice (Grenfell, 1983; Light, Maykut & Grenfell, 2003; Vancoppenolle et al., 2013; Oggier & Eicken, 2022) . Lofgren & Weeks (1969) noted that the size and geometry of plates influence the amount of brine entrapped in the ice. The

Antarctic MIZ that is dominated by the dynamic growth of ice, resulting in large portion of granular-textured ice (Eicken et al., 1997; Haas, 2003; Weeks, 2010), unlike the columnar dominated Arctic ice that receives more attention. Sea ice observations of small-scale properties are largely derived from the Arctic while Antarctic models do not often capture the variability of the Antarctic sea ice, suggesting a systematic misrepresentation of the physical properties of the sea ice in atmospheric and ocean processes (Lecomte et al., 2016).

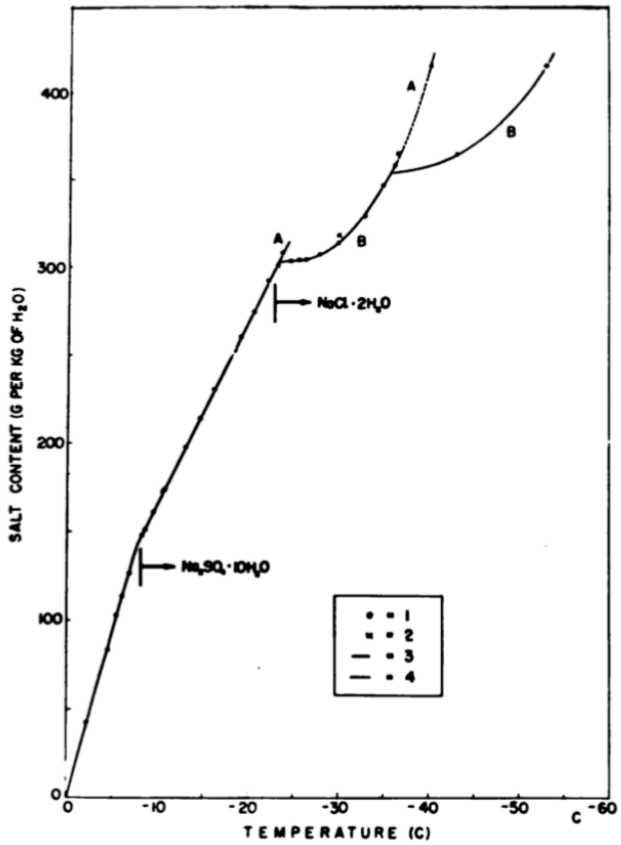


Figure 2.5: Freezing point of brine as a function of the ratio of dissolved salts to pure water (Assur, 1960)

The crystallographic properties of ice are influenced by the growth conditions (Petrich & Eicken, 2017) and will consequently influence the brine inclusions within the ice. The texture of the ice furthermore affects the shape of the brine inclusions (Büttner, 2011; Oggier & Eicken, 2022). Granular ice has shown a more heterogeneous inclusion structure with less interconnected inclusions attributing to lower permeability for similar brine porosities in columnar textured ice during growth periods (Oggier & Eicken, 2022). Elongated tube-like brine inclusions are characteristic of columnar ice (Light, Maykut & Grenfell, 2003; Büttner, 2011; Oggier & Eicken, 2022). The plate spacing, previously mentioned, gives rise the elongated brine inclusions as brine gets trapped between the growing plates. These shapes of the inclusions are important parameters that affect the mechanics and optics of the ice

(Weeks & Assur, 1967; Lofgren & Weeks, 1969; Grenfell, 1983; Light, Maykut & Grenfell, 2003; Crabeck et al., 2016).

Arctic first year ice during ice growth has shown lower permeability in granular ice compared to columnar ice with similar brine porosities (Oggier & Eicken, 2022), although this ice typically contains less than 10 cm of granular-textured ice near the ice-atmosphere interface (Crabeck et al., 2016; Maus, Schneebeli & Wiegmann, 2021; Salomon, Maus & Petrich, 2021). Antarctic first year sea ice has shown significantly greater proportions of granular ice, especially in more dynamic regions, even with interchanging regions of granular and columnar ice possibly due to rafting pancakes (Lange & Eicken, 1991; Johnson et al., 2023). Therefore, the permeability of sea ice in the Antarctic during the winter period may not show the similar trends due the different growth conditions in that environment.

The volume, number density and the size distribution of brine inclusions are important aspects of sea ice that influence the permeability (Golden et al., 2007; Maus, Schneebeli & Wiegmann, 2021; Salomon, Maus & Petrich, 2021) along with mechanical, optical and thermal conductivity properties (Weeks & Assur, 1967; Petrich & Eicken, 2017). Despite the important role the microstructure of sea ice plays, there is no complete quantitative description of the evolution of the microstructure through the growth and melt periods (Petrich & Eicken, 2017). Table 2.1 reports number densities on a volume basis for brine inclusions in sea ice.

There is a general consensus that brine inclusions becomes more interconnected at higher temperatures reducing brine number densities (Eicken et al., 2000; Golden et al., 2007; Maus, Schneebeli & Wiegmann, 2021). This suggests that lower temperatures promote higher brine number densities and smaller inclusion sizes (Grenfell, 1983; Salomon, Maus & Petrich, 2021). The most notable changes in brine number density decreases has been associated with temperatures near the melting points of those sea ice samples (Perovich & Gow, 1996; Light, Maykut & Grenfell, 2003; Golden et al., 2007). The inclusion size distribution has shown varying sizes depending on the resolution of images or scans. This is seen by Salomon, Maus & Petrich (2021), who noted the mode of the inclusion sizes for closed brine inclusions corresponded to two times the resolution of their scans. Similarly, Perovich and Gow (1996) noted in the cross-sectional areas of brine inclusions in first year columnar ice, the highest probability of inclusions corresponded to an area the size of a pixel. However, they state that the area distribution of brine inclusions is best described by a cumulative lognormal distribution. A general trend of decreasing number density of brine inclusions with increasing size is observed through several studies with several parameters that have been used to describe the size of brine inclusions such as volume, throat size, inclusion radius, length and

area (Eicken, 1993; Perovich & Gow, 1996; Light, Maykut & Grenfell, 2003; Maus, Schneebeli & Wiegmann, 2021; Oggier & Eicken, 2022).

Table 2.1: Comparison of brine number densities on a volume basis in sea ice

Notes	Brine Porosity	Number density (no./ mm^3)		Analysis Temperature	Resolution
Salomon, Maus & Petrich, 2021 centrifuged then CT scanned Arctic first year spring sea ice samples	2 to 40%	1-10		Centrifuged at -3°C and scanned at -15°C	25 µm
Light, Maykut & Grenfell, 2003 used thin section analysis on first year Arctic sea ice samples	1.2%	24		-15°C	~3 µm
Eicken et al., 2000 analysed vertical and horizontal slices from MRI scan of artificial sea ice samples	1 to 21%	Vertical: 0.75 0.62 0.58	Horizontal: 0.95 1.05 1.08	-21°C -10°C -6°C	100 µm
Perovich & Gow, 1996 used thin section analysis with the values reported are associated with artificial pancake and first-year ice	3.7% to 14.6%	0.2 to 4.5		-2.0°C to -6.9°C	30 µm

Methodological constraints are important factors that influence the detectability of inclusions as noted by Eicken et al. (2000), however these are discussed further in section 2.4.2. Alternative physical factors that influence the number density and size of brine inclusions are associated with physical parameters that can be attributed to different ice types, depths, brine porosities, salinity, temperatures, textures and growth rates (Grenfell, 1983; Perovich & Gow, 1996). However, there is no complete description of the influences of all these factors on brine number densities.

Temperature is an important factor that governs sea ice formation, evolution and the microstructural properties of sea ice. Despite its importance, there are limited studies on the

effects of temperature on microstructure (Petrich & Eicken, 2017). Several studies have shown brine inclusions merge and become elongated during heating sequences, most notably at temperatures near the melting points of those samples (Light, Maykut & Grenfell, 2003; Golden et al., 2007). Light, Maykut & Grenfell (2003) conducted a heating and cooling sequence, noting the merging of brine inclusions during the heating sequence, however during a subsequent cooling sequence the brine inclusions did not break up into the same number of smaller inclusions as was prior to the thermal sequence (Figure 2.6). This illustrates that despite the sample having the same temperature at the beginning and the end of the heating and cooling sequence, the sea ice showed non-reversible changes in the brine inclusion properties. The temperatures selected in Light, Maykut & Grenfell's (2003) study were relatively high temperatures, closer to the melting temperature of sea ice, therefore these temperatures maybe higher than the threshold for breakdown of brine inclusions.

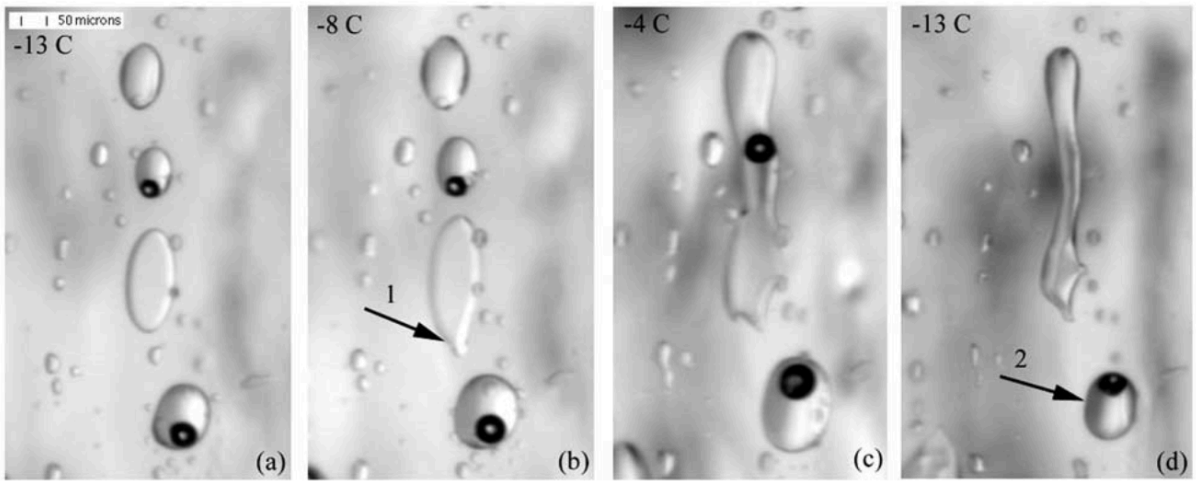


Figure 2.6: Illustration of a warming sequence (a-c) and cooling (d) on a sea ice brine and air inclusions (Light, Maykut & Grenfell, 2003)

Studies of sea ice with lower storage temperatures and longer storage periods have noted higher brine number densities compared to samples analysed or maintained at higher temperatures (Perovich & Gow, 1996; Eicken et al., 2000; Light, Maykut & Grenfell, 2003; Salomon, Maus & Petrich, 2021). Grenfell (1983) and Anderson & Weeks (1958) theorised the breakdown of brine inclusions into smaller spherical inclusions during a cooling cycle. Figure 2.7 illustrates the process described by Grenfell (1983) through the non-uniform shrinkage of the radius of cylindrical inclusions (typical in columnar-textured ice) causing necking along the length of the cylindrical inclusions. Through this breakdown of cylindrical brine inclusions to smaller spherical inclusions there is a phase prior to the necking points freezing over to form multiple smaller inclusions where these inclusions become less regular. This phase of reducing regularity prior to the break-up of the inclusion would be characteristic

of decreasing sphericity followed by an increase after the break-up of the inclusion into multiple smaller inclusions. Once the necking points freeze over breaking-up the brine inclusion into multiple inclusions, the bine inclusions are theorised to be more spherical.

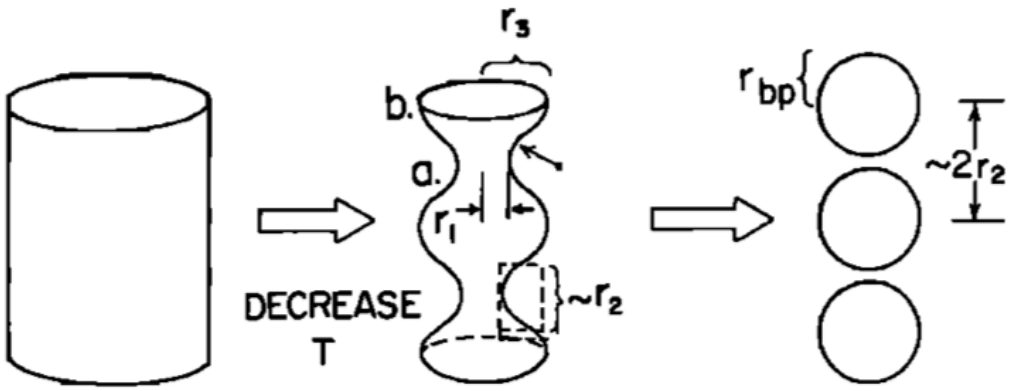


Figure 2.7: Schematic representation of the formation of brine pockets from brine cylinders during cooling (Grenfell, 1983)

Although Grenfell (1983) theorised the breakdown of brine inclusions during a cooling cycle, he did not hypothesize the impact of a subsequent heating sequence on the smaller inclusions and if these brine inclusions would reform a cylindrical inclusion upon heating. Anderson & Weeks (1958) however, speculated that brine inclusions would enlarge and merge along plates thus forming cylindrical inclusions again upon heating. Storage temperatures for sea ice sample are typically -20°C (Cox & Weeks, 1986; Eicken et al., 2000; Crabeck et al., 2016). These protocols were established to immobilise brine and preserve ice microstructure (Eicken et al., 2000). Brine inclusion are greatly influenced by temperature (Assur, 1960; Cox & Weeks, 1983), as such they would also be influenced by these low storage temperatures. Yet, samples are typically tested in warmer conditions than the storage temperatures (Light, Maykut & Grenfell, 2003; Maus, Schneebeli & Wiegmann, 2021; Salomon, Maus & Petrich, 2021; Oggier & Eicken, 2022) resulting in samples experiencing cycles of low temperatures. Studies of the impacts of these cyclic low storage temperatures and heating for analysis on the volume and morphology of the brine and air inclusions are sparse.

Cox & Weeks (1986) conducted a theoretical examination of the impact of shipping and storage temperatures on the salinity and brine porosity of sea ice suggesting a slight reduction in porosity and salinity after low temperature storage. Cox & Weeks (1986) suggested the brine volume would experience a 2% reduction in most cases and a 15% reduction in extreme cases. This theory is based on the expulsion of salt from of pores due to the ~10% difference in the density of ice and liquid water. It was suggested that during cooling salt would be

expelled due to the increasing space the water within the inclusion would take up over the phase change to ice. In turn, during a heating sequence, the inclusion would expand again and air inclusions would form in the brine due to the volumetric differences associated with the phase change from ice to water (Tsurikov, 1979; Cox & Weeks, 1986).

Thermodynamic equilibrium between the different phases in sea ice affects its brine porosity. At equilibrium, the ice and brine coexist in a state where the melting and freezing rates of the brine are equal (Notz, 2005). As temperature decreases brine inclusions within the ice will reduce in size to maintain thermodynamic equilibrium, thus leading to a localised increase in salinity within the brine inclusion. However, the bulk salinity of the sample is expected to remain unchanged (Petrich & Eicken, 2017). Bulk salinity is largely considered a conservative property (Salomon, Maus & Petrich, 2021). This in addition to this, Cox & Weeks (1986) hypothesis suggests that low temperature thermal cycles should result in small reductions of brine porosity over temperature cycling, if the temperature at the beginning and end of a thermal cycle are essentially the same.

There is no complete quantitative description of the impact of these low temperature storage cycles on the inclusions in addition to no complete quantitative description evolution of the microstructure of sea ice through the growth and melt periods (Petrich & Eicken, 2017).

2.4 Analysis of Sea Ice Texture and Structural Properties

There are two categories through which the internal structure of sea ice can be studied, namely destructive and non-destructive methods. Sea ice samples were historically cut into thick or thin sections to study the internal structure of sea ice (Lieb-Lappen, Golden & Obbard, 2017). These are destructive methods and further properties (e.g. mechanical) cannot be determined (Eicken, 1993). Stereological implications can be associated with thin section analysis as it only allows for either horizontal or vertical two-dimensional (2D) sections to be studied (Eicken, 1993) which has been shown to produce different results in different planes (Eicken et al., 2000). Furthermore, the distinction between brine and air inclusions in photographs of thick and thin sections of the ice can be ambiguous (Loose et al., 2011). X-ray computed tomography (CT) scanning and Magnetic Resonance Imaging (MRI) are non-destructive methods of analysis (Kawamura, 1988; Maus et al., 2009; Galley et al., 2015). These non-destructive analysis methods have led to many developments in sea ice microstructural studies as the internal structure of the ice is preserved (Kawamura, 1988).

The texture of sea ice has typically been determined using a microtome and polarised lenses along with qualitative and quantitative measurements (Eicken & Lange, 1989; Crabeck et al., 2016). More recently the development of a thermal macrotome (Johnson, 2020) has allowed for larger thin sections of ice to be segmented for further analysis in order to determine the textural properties of the ice.

2.4.1 X-ray Computed Tomography Scanning

CT scanning was initially developed for the medical field, but has since been adapted for other industries as it allows for the preservation of internal features of porous and multiphase materials such as metals, ceramics and plastics (Kawamura, 1988). The first application of this technique to sea ice was first reported by Kawamura (1988). This technique allows for the three-dimensional visualisation and characterisation of the internal configuration of these materials and the air and brine phases of sea ice to be studied within the ice structure in a non-destructive manner. The advancement of this technology: micro-CT (μCT) scanning further allows for the spatial resolution to be explored down to features that are within the units of several microns (Lieb-Lappen, Golden & Obbard, 2017). The internal brine and air inclusions on a micrometre scale can therefore be studied through CT scans (Kawamura, 1988; Crabeck et al., 2016; Lieb-Lappen, Golden & Obbard, 2017; Salomon, Maus & Petrich, 2021).

The generation of the 3D visualisations of the sea ice structure is possible due to the variation in the absorption and transmission of X-rays as a result of the different densities of ice, brine and air. X-ray absorption is sensitive to material density, therefore, the sea ice phases can be distinguished due to their noticeable differences in densities (Lieb-Lappen, Golden & Obbard, 2017). Ice samples are imaged through X-ray projection radiographs at many angles through 360°. The projections are then reconstructed into vertically stacked 2D grey scale slices (Lieb-Lappen, Golden & Obbard, 2017).

One of the most critical steps that dictates the quantitative and qualitative measurements is the thresholding of CT scan images (Crabeck et al., 2016). Thresholding of images is a technique that segments parts of images based on the colour of voxels (3D pixels), in the case of CT scans the colour range is a greyscale. The thresholding distinguishes the three phases (ice, liquid and air) for which further analysis of sea ice is based (Lieb-Lappen, Golden & Obbard, 2017). Figure 2.8 shows an image slice of a scan where set ranges of greyscale values were chosen, and the image was separated out into 3 phases each represented by a colour. The results of the trinary image provide insight into the internal structure of the

inclusions in sea ice samples (Lieb-Lappen, Golden & Obbard, 2017). The thresholding allows for the measurement of the liquid and air inclusions properties that can lead to mathematical descriptions of the microstructure as well as modelling of the micro-dependent properties of sea ice (Lieb-Lappen, Golden & Obbard, 2017).

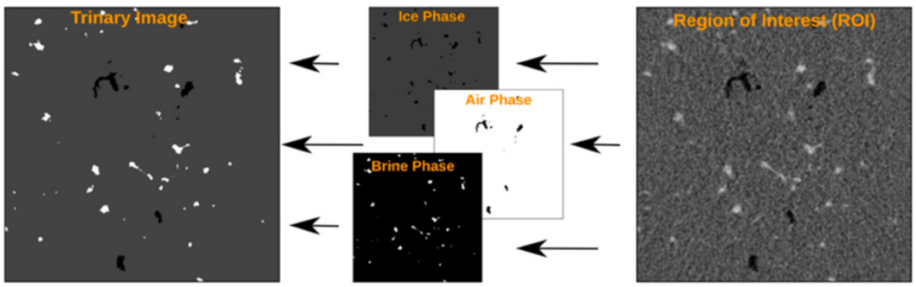


Figure 2.8: Thresholding a trinary image of sea ice (grey), brine (white) and air (black) (Lieb-Lappen, Golden & Obbard, 2017)

The scans are sensitive to the thresholding values chosen. Figure 2.9 highlights air inclusions seen in a slice from a CT scan. The red boxes around the highlighted inclusions indicates the boundaries of inclusion based on the greyscale thresholding values which are different for inclusions 2 and 3. The pixel scale of Figure 2.9 shows how the selection of pixels that form part of the air inclusions can become ambiguous (Crabeck et al., 2016).

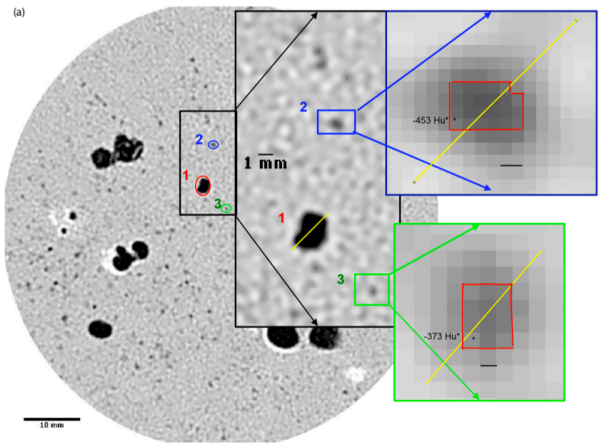


Figure 2.9: CT scan image with highlighted air inclusions (Crabeck et al., 2016)

The three main categories of approaching thresholding are manual thresholding (human visual system), automated thresholding (based on image data that typically employ image histograms) and a mixture model approach (Crabeck et al., 2016). Prior to the application of thresholding methods, scans are filtered. The application of filtering reduces noise in the scans for better application of the thresholding methods as shown in Figure 2.10 (Crabeck et al., 2016; Maus, Schneebeli & Wiegmann, 2021; Salomon, Maus & Petrich, 2021). While filtering

reduces noise it can also remove small inclusions, thus underestimate the brine porosity of samples especially in low ice-brine contrast scans.

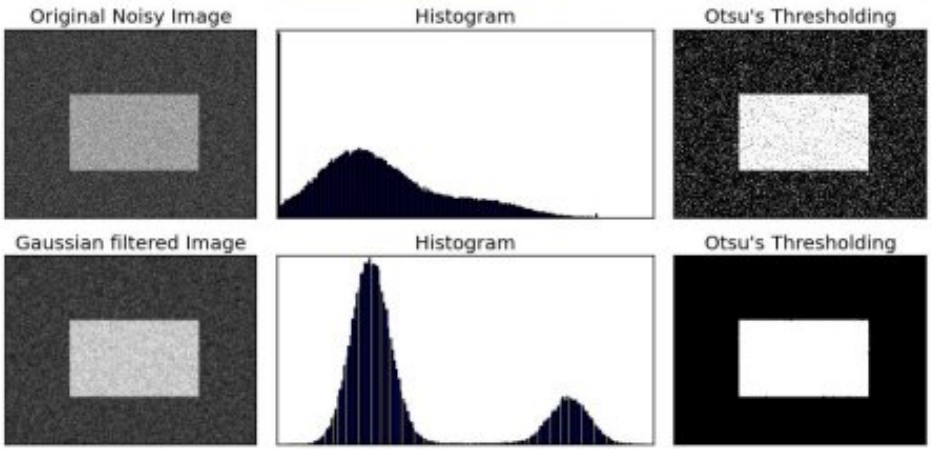


Figure 2.10: Otsu's method applied with and without a Gaussian filter (OpenCV, 2022)

A manual threshold is selected based on a visual analysis of the images or scans. Manual thresholding from a single analyst can yield more reliable results especially when a large variability in brightness over the samples and poor contrast in the phases is seen (Frantz et al., 2019). However, this method is considered subjective (Crabeck et al., 2016).

A mixture model approach determines if voxels that are less than 50% ice are categorised as either brine or air (Oggier & Eicken, 2022). This approach determines the thresholding values for the air-ice interface based on relationships for the Hounsfield Units (HU) which can selcted based on histograms modes or selections within a range of values (Crabeck et al., 2016; Oggier & Eicken, 2022). The same process is used for the determination of the brine and air phases.

Automated thresholding techniques can broadly be defined into global and cluster (or local) categories. Global thresholding selects a single thresholding value that is applied to the whole image a scan while a cluster or local method can adapt the threshold value to different regions within an image as show in Figure 2.11.

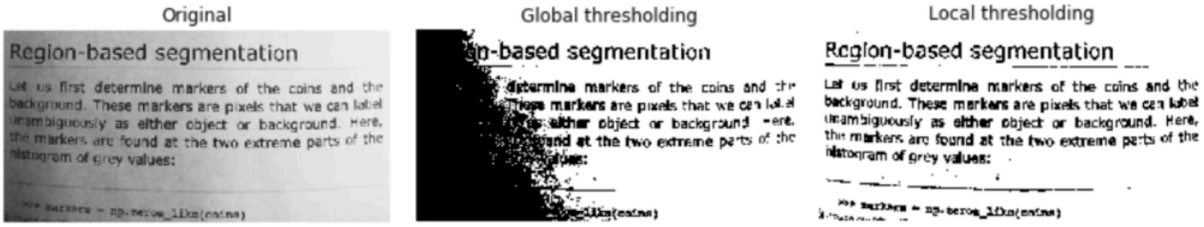


Figure 2.11: Example of global and local thresholding (Gonzalez, 2015)

One example of a global histogram-based thresholding method was used by Lieb-Lappen, Golden & Obbard (2017) to distinguish the different phases. The thresholding values were determined by selecting the transition points along a greyscale histogram as shown in Figure 2.12.

Crabeck et al. (2016) investigated a number of computational algorithms for thresholding of air inclusions within sea ice samples. Statistically no difference was seen in the air volume fractions computed between the mixture model approach and the visual method or the cluster-based algorithm for their study. However, Crabeck et al. (2016) did determined that the cluster-based Rider's method was the most applicable model.

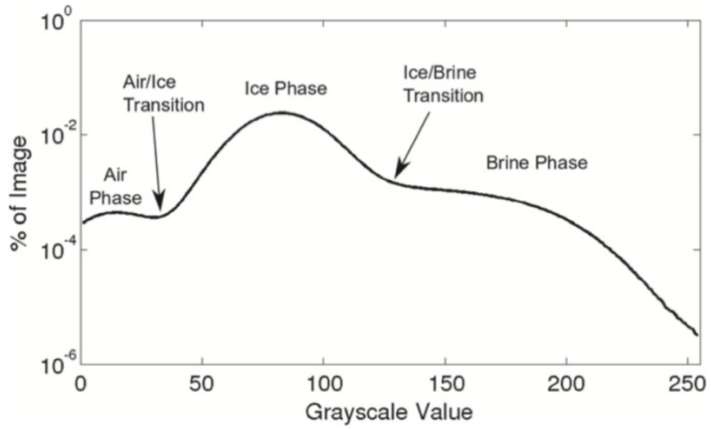


Figure 2.12: Representative histogram for thresholding (Lieb-Lappen, Golden & Obbard, 2017)

The application of these algorithms then allows for phase segmentation after which phase related properties of the ice can be determined and investigated. These can then be used to generate mathematical and quantitative descriptions of properties of the ice such as the evolution of the microstructure or vertical profiles of the inclusion volumes in sea ice.

2.4.2 Methodological Limitations of Microstructural Analysis Methods

As with any analysis methodology, it is imperative to acknowledge certain methodological limitations that may influence the output of the analysis method. These limitations can be associated with procedural constraints linked to sample preparation methods or spatial limitations related to the capabilities of the equipment or technology used to analyse samples.

One procedural method has noted certain analysis limitations associated with centrifuging sea ice samples. More recent studies have centrifuged samples to remove brine from inclusions connected to the surface of the ice samples (Büttner, 2011; Maus, Schneebeli & Wiegmann, 2021; Salomon, Maus & Petrich, 2021; Oggier & Eicken, 2022). Open air inclusions are later classified to have previously been brine from CT scans, as the air is less susceptible to microstructural modifications with temperatures changes. While centrifugation aids in studies about sea ice permeability and percolation using measurements such as throat size and connectivity parameters, the air porosity of the sea ice is not fully quantified. Centrifuging samples may not give an accurate estimation of the total air content of the ice as air inclusions within brine are removed and the air inclusion may be classified to have previously been only brine which were actually large air inclusions. Salomon, Maus & Petrich's (2021) study noted an over estimation of CT-based density measurements above the ice freeboard compared to more conventional density measurements, which may be attributed to open air inclusions in the upper sections of the ice being classified as brine. Macro air inclusion have been observed towards the ice-atmosphere interface (Crabeck et al., 2016) and are therefore likely to be classified as brine in CT studies that centrifuged samples. This can lead to the overestimation of the brine content and other properties such as density in the upper portion of the ice as observed by Salomon, Maus & Petrich (2021). It has noted that ice initially formed from frazil ice contains more air than thermodynamically grown ice with columnar-textured ice (Tsurikov, 1979; Zhou et al., 2013; Crabeck et al., 2016). Additionally, air inclusions entrapped in brine have been observed (Light, Maykut & Grenfell, 2003).

Other procedural limitations as previously mentioned have been noted with the direction in which samples are cut or observed in vertical or horizontal thin section analyses as noted by Eicken et al. (2000). Thin section analysis of ice samples can lead to stereological implications such as the assumption of isometric inclusions in the horizontal plane (Kawamura, 1988; Eicken, 1993; Light, Maykut & Grenfell, 2003). Furthermore, a methodological limitations of thin section analysis specifically for air inclusion is the ambiguity of detecting the difference between brine and air phases of transmitted images (Loose et al., 2011) irrespective of vertical or horizontal orientations.

The methodological constraints of different analysis techniques and the resolution of those techniques are highlighted in the detectability of inclusions (Eicken et al., 2000; Light, Maykut & Grenfell, 2003; Crabeck et al., 2016). As noted by the lower resolution of Eicken et al.'s (2000) study, more inclusion became apparent when analyses at higher temperatures were conducted due to the enlargement of inclusions. The advancement of technology has allowed

for CT scanning capabilities to improve scans from a millimetre scale resolution down to a micrometre scale (Lieb-Lappen, Golden & Obbard, 2017).

Eicken et al. (2000) investigated number densities of brine inclusions on a per slice basis from MRI scans which is able to maintain the 3D nature of the ice akin to CT scanning. They noted higher number densities in the vertical slices compared to horizontal slices of the MRI scans, highlighting the methodological constraints of slice analysis irrespective of 2D or 3D analysis. This illuminates the limitations of the thin section analysis particularly with respect to granular ice which does not exhibit the structured arrangement of vertically elongated cylindrical brine inclusions typical of columnar textured ice (Büttner, 2011; Oggier & Eicken, 2022). Investigations using thin section analysis overlook a comprehensive understanding of the 3D characteristics of the inclusions. The use of analysis methods maintaining 3D properties of the ice allows for better understanding of characteristics such as the interconnection of inclusions that cannot be seen in per slice analysis of CT or MRI scans and thin section analysis. These spatial limitations may determine the detectability of inclusions and therefore properties such as number densities and dimensions and are important factors to take note of.

2.5 Rationale of Study

Microstructural properties of Antarctic sea ice are understudied compared to its Arctic counterpart. Studies that have focused on Antarctic sea ice report on land-fast ice or pack ice from regions in the Weddell, Bellingshausen and Ross Seas that exhibit relatively calm environmental conditions similar to the Arctic. Pancake and frazil ice dominate the Antarctic MIZ, however studies on properties of winter Antarctic pancake ice floes have focused on the textural, mechanical and biogeochemical properties of this sea ice type (Audh et al., in press; Paul et al., 2022; Skatulla et al., 2022). Furthermore, there are no studies on the spatial variability of brine and air porosity profiles within a single pancake floe from the Antarctic MIZ. Temperature greatly influences the volume and number densities of brine inclusions in sea ice samples. Samples are subjected to low temperature (~-20°C) storage prior to heating for analysis at higher temperatures (~-10°C). The impact of temperature fluctuations on the brine and air inclusions within sea ice have been tested on samples after they had been in low temperature storage conditions. The impact of cyclic low temperature fluctuations on brine porosity have been considered negligible with no validation through empirical investigations. In addition, no studies have reported the effects of heating either through the vertical axes of samples or from multiple directions on the shape and volume distributions of brine inclusions in sea ice. This study will focus on the optimisation of sampling protocols through maintaining the samples at higher temperatures (-10°C) prior to CT analysis. In addition, the influence of

low temperature storage on the brine and air inclusions in sea ice samples will be carried out with a specific focus on differences between uni- and multidirectional heating effects. Lastly, the spatial variability of porosity profiles within a single pancake floe will be investigated.

3 Research Objectives

3.1 Research aim and objectives

The aim of this study to provide an optimised methodology, in terms of both sea ice sample handling and data processing of x-ray computer tomography, for air and brine inclusion analysis from pancake ice samples, conducted on samples collected during winter periods from the Antarctic marginal ice zone during winter 2019 and winter 2022 expeditions.

The objectives are therefore:

- Optimise the storage protocols during the winter 2022 expedition in order to minimise the impacts of low temperature storage on the brine and air inclusions.
- To use data engineering methods and tools to optimise the processing of CT scan data. This will be done to get the volume, diameters, projected dimensions, sphericities and number of the brine and air inclusions within sea ice samples.
- To comparatively evaluate the efficiency of the sea ice sample protocol methods utilised in the winter 2022 expedition from the winter 2019 expedition on the brine and air inclusions.
- To investigate the impact of low temperature storage and subsequent heating methods on the measured brine and air inclusions within sea ice samples.
- To investigate the measured spatial variability of brine and air inclusion profiles from a single pancake floe sourced in 2022.

3.2 Scope of study

This study will focus on samples collected from the Antarctic MIZ during the austral winter 2019 and 2022 periods. First-year pancake floes formed in this environment were collected for μCT analysis of the brine and air inclusion within the ice. The scope will encompass the impact of low temperature storage at -18°C and higher temperature μCT analysis conducted at -10°C using uni- and multi-directional heating methods. The impact of time periods in the low temperature storage conditions and sample sizes was beyond the scope of the study. Furthermore, the synoptic history of the ice growth prior to sample collection and the presence of biological organisms were outside the parameters of investigation.

4 Methodology

4.1 Sample Collection, Physical Property Measurements and Analytical Methodology for Sea Ice Texture and Microstructure

Optimising sample preparation and storage protocols is of paramount importance in sea ice research to ensure accurate and representative analysis of its thermally responsive properties. The intricate and heterogenous nature of sea ice requires careful sample handling including preservation and preparation in order to reduce microstructural changes brought about by temperature fluctuation within samples. Sample preparation and storage condition optimisation can enhance the reliability of research findings to facilitate more robust comparisons across studies. This section outlines the optimised protocols for sample storage conditions and preparation methods that were used for samples collected during the winter 2019 and 2022 expeditions to the Antarctic MIZ. Sample protocols underwent initial development for the winter 2019 expedition which were then refined and optimised for the subsequent winter 2022 expedition. Some of the modifications include the storage temperatures and number of samples collected per pancake outlined in the appropriate sections below, with differences in the winter 2019 sample protocols will being mentioned where relevant.

4.1.1 Sample Collection Locations

The Southern oCean seAsonaL Experiment (SCALE) winter 2022 cruise took place from the 11th to the 31st of July departing from Cape Town to the Antarctic MIZ aboard the *S.A. Agulhas II*. The ship entered the MIZ on the 19th of July and exited the ice on the 25th of July (Vichi, 2023). Samples from pancake floes were collected from three stations, but this study will only focus on one station where cores for crystal texture and porosity were collected. The station from the winter 2022 expedition is named 22WMIZ3 and shown in Figure 4.1 (right). The pancake floe was collected on the 24th of July 2022. Two pancake floes were collected at this station, however, this dissertation will only focus on one pancake floe. Five ice cores were collected from the pancake floe, with two for textural analysis and three for porosity analysis.

The SCALE winter 2019 expedition to the Antarctic MIZ on board the *S.A. Agulhas II* took place from the 18th of July to the 8th of August 2019 (Ryan-Keogh & Vichi, 2022) departing from Cape Town. The ship entered the MIZ on the 26th July and departed the ice on the 28th of July. Four pancake floes were collected on the 28th of July at the 19WMIZ1 station shown in Figure 4.1 (left), however, this study will only focus on one of the pancake floes collected.

This was based on the assumption of pancakes from the same location will show similar results and for the purposes of this study on optimisation of sample collection methodology and storage conditions, multiple pancakes from one location is not necessary.

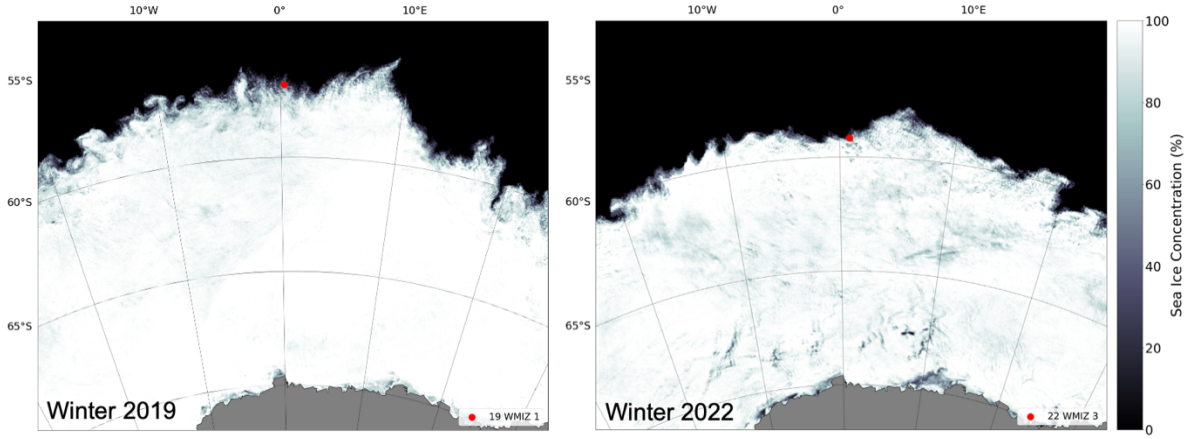


Figure 4.1: Pancake floes collection locations for winter 2019 (left) and winter 2022 (right) expedition with sea ice concentration shown for the 27th July 2019 and 24th July 2022 respectively

Table 4.1: Summary of weather conditions at ice stations on the winter 2019 and 2022 expeditions

Station	**19WMIZ1***	**22WMIZ3**
Sampling Date and Time (UTC)	28th July 2019 09:45	24th July 2022 08:43
Latitude	56.8 S	59.2 S
Longitude	0.3 E	0.9 E
Average air temperature (°C)	-11.6	-1.4
Average wind speed (knots)	7.6	15.7
Snow	none	none
Storage Time prior to CT Analysis	2 years	1 month
Storage Temperature of CT Cores (°C)	-18	-10

*(Johnson, 2020)

4.1.2 Pancake Sample Collection and Safety Protocols

The Antarctic's environment is characterised by its harsh conditions and cold temperatures necessitating the use of specialised personal protective equipment (PPE) when working in these conditions. The PPE worn during sample collection and working in the sub-zero cold laboratories or ship freezers include a polar jacket, polar pants, buff, beanie, thermal gloves and steel-capped safety boots. Additionally, hard hats are worn during crane operations. These conditions and PPE do limit scientific operations do a certain degree.

Pancake floes were collected using the Agulhas's sternward crane that lifts floes with a custom-made heavy duty net, spreader beam and guide ropes from the ocean and onto wooden slates located on the helicopter deck of the ship shown in Figure 4.2. Pancake floes were selected at the locations based on observations of approximate size and weight of floes within the crane operational limits, typically be no more than 3 meters in diameter and 5 tonnes in mass. The operation of the crane is only advised for wind speeds below 20 knots and ocean swells that are not too large (due to the rocking of the boat) to avoid the inertia of the suspended pancake floes from swaying relative to the deck, which would be dangerous given the pancake's mass. The pancake is ideally lowered calmly onto the deck. Coring of ice samples begins once the pancakes were safely placed on wooden slates and crane operations are ceased, which was done within 4 minutes of removal from the ocean in these considered samples. A ladder was placed next to the pancakes for coring due to safety concerns about undermining the structural integrity of the pancakes during the coring process if it was stood upon.



Figure 4.2: Photograph taken during the winter 2022 expedition of pancake collection in progress with the wooden slates shown where the floes are placed

Ice cores were collected using a 1m long and 9cm diameter Kovacs Mark II Corer with a battery-powered drill attached to the top of the barrel to drive the barrel into the ice. The ice core was collected within the barrel as the corer was driven vertically down into the ice. Once the corer had cut through the ice, the ice core was extracted through the top of the barrel and positioned horizontally (to avoid further brine drainage) and was maintained horizontal during

transportation and storage. Ice samples were either placed in marked plastic sleeves or immediately processed on deck to determine the vertical temperature gradient described further in section 4.1.3. The two pancakes outlined in this study had rafted edges and snow cover, however, they did not have any apparent decolouration from a biologically active layer.

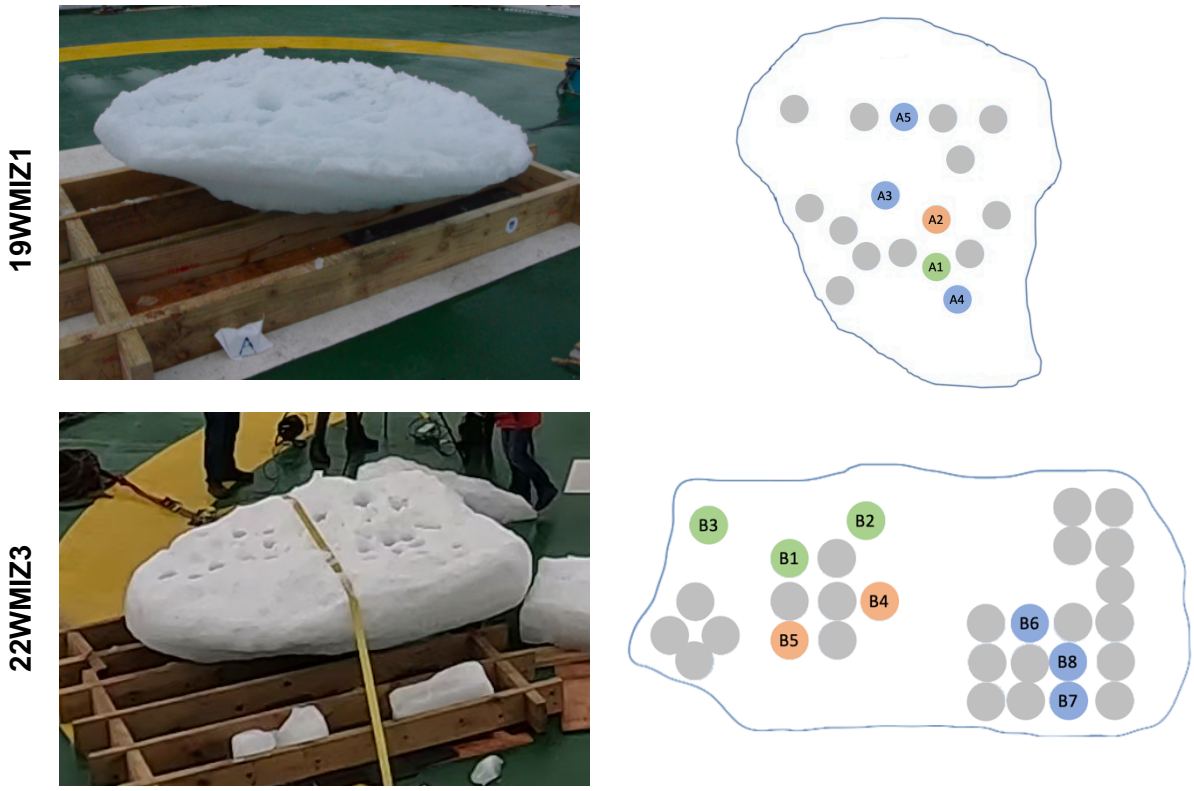


Figure 4.3: Photographs of the pancake floes (left) with their corresponding schematics (right) of the coring locations from the pancake floes collected at 19WMIZ1 (top) and 22WMIZ3 (bottom) (Photographs from winter 2019 from Lin (2022) *and winter 2022 from Agoritsa Spirakis)*

Images of the pancake floes and schematics coring locations on each pancake floe can be found in Figure 4.3. From each pancake floe, between 17 and 30 ice cores were collected. All cores were extracted within approximately three and a half hours and coring began within 40 minutes of the pancake being removed from the ocean. The testing designation of the core pertaining to this study are labelled in the schematics in Figure 4.3 with their testing designation outlined in Table 4.2. Due to the turbulent conditions of the Antarctic MIZ, as apparent by the formation of the pancake floes, the depths of each core within the pancake floe can vary as seen in Table 4.2.

Table 4.2: Overview of stations, core IDs, testing designations and core depths (TS - temperature and salinity, CT – μCT scanning, XP- cross polarization)

Station	Core ID	Analysis			Ice Depth (cm)
		TS	CT	XP	
19WMIZ1	A1		X		20
	A2			X	28
	A3	X			40
	A4	X			35
	A5	X			29.5
22WMIZ3	B1		X		50
	B2		X		61
	B3		X		55.5
	B4			X	50
	B5			X	51
	B6	X			55
	B7	X			65
	B8	X			60

4.1.3 Temperature and Salinity Measurements of Cores

Temperature measurements were immediately taken from the cores after the extraction from the pancake floes as these are time-sensitive measurements. Temperature cores were placed in plastic core holders where temperature readings were taken every 5 cm along the length of the core from the bottom of the core. Temperature readings were taken using a Testo GMH 3750-GE logger and PT-100 penetration probes GTF 401 1/10 DIN with an accuracy of ±0.01°C. The temperature probes were placed in pre-drilled holes using a cordless battery-powered Makita hand drill. Temperature readings were taken within 12 minutes and any minor temperature changes that occurred between when the pancake was removed from the ocean and the temperature measurements recorded are immeasurable, and assumed negligible given the relatively high heat capacity of sea ice.

The cores from which temperature measurements were obtained were then transported to the ship's freezer, set to a temperature of -10°C. The cores were then cut using a circular saw into 5 cm segments and placed into numbered plastic containers for salinity measurements. Although brine drainage is likely to occur before cores were segmented, the extent of brine drainage is indeterminable. The segments for salinity during the winter 2019 expedition were cut at a larger height at approximately 10 cm segments using a band saw operating in a mobile polar laboratory, which was unavailable during the 2022 expedition.

The ice segments were melted in a refrigerator set at +5°C and placed in glass bottle to test the salinity using a 8410A Portasal portable salinometer with a reported accuracy of 0.003 psu (OSIL, 2020). The salinometer underwent initial calibration prior to testing, followed by subsequent calibration after every 24 samples.

The temperature and salinity measurements were recorded for a minimum of 3 cores for each pancake floe, with the length of each core varying slightly due to the spatial variability of cores within the pancake floe.

4.2 Textural and Structural Analysis

This section outlines the methodologies followed to analyse the texture and the microstructure of sea ice. A thermal macrotome is a novel instrument (Johnson, 2020) that was used to determine the crystal texture and stratigraphy of sea ice in addition to polarised sheets, which is discussed in section 4.2.1. CT analysis was used to study sea ice microstructure relating specifically to the brine and air inclusions which is outlined in section 4.2.2. This section will include the protocol used to test the effects of uni- (UD) and multi-directional (MD) heating of sea ice from low temperature storage to higher temperature CT analysis temperatures.

4.2.1 Cross Polarisation Methodology

Cross polarisation is a technique used to visualise individual crystals in thin slices of sea ice, through perpendicular polarised sheets. This allows for the sizes of crystals to be measured as well as the shape of crystals to be seen. As covered in the Literature Review; the shape and size of crystals are indicators of the texture of sea ice of which the main types consist are granular and columnar and this texture is an indicator of the sea ice growth conditions.

Two pancake floe cores were collected during winter 2022 and one during winter 2019 for textural analysis. Cross polarisation cores were cut into 10 cm segments and a 8 mm thick slice through the centre of those segments was then cut using a circular saw (Figure 4.4). Thin slices of 1 mm thickness were then obtained by the thermal macrotome (Johnson, 2020) using a high temperature nichrome wire. The thin slices were transferred onto a transparent plastic sheet within a light box where perpendicular polarised sheets are placed around the sample. Images were then captured with the corresponding section name, orientation and ruler for scale. Each individual crystal can then be distinguished, outlined and then measured. The

crystal sizes were measured using ImageJ (Rasband, 2018) by averaging the size of 20 random crystals. This was used to determine the crystal texture for stratigraphy diagrams. The standard deviation and 95% confidence interval for crystal sizes are computed and coupled with visual inspection to determine the ice texture based on the categorisations and descriptions of Eicken and Lange (1989).

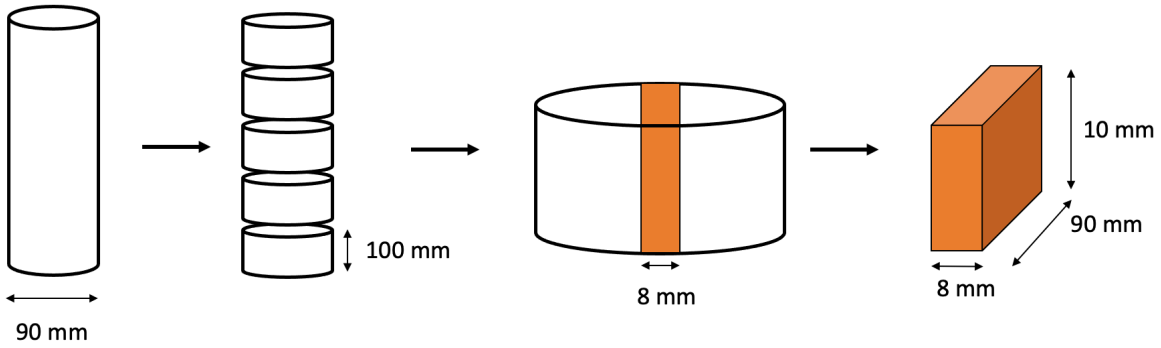


Figure 4.4: Schematic diagram showing how a core sample was cut to produce a section of sea ice for cross polarisation

Winter 2022 samples were cross polarised onboard the SA Agulhas II within 6 days after the pancake at 22WMIZ3 was collected. Cross polarisation of the winter 2019 sample took place at the University of Cape Town approximately six months after collection (Skatulla et al., 2022).

4.2.2 X-ray Computed Tomography Methodology

Micro-computer tomography (μCT) allows for three dimensional visualisation and measurement of different phases within sea ice through non-destructive means. This technique was used to investigate and determine the liquid brine and air phases in sea ice. The different densities of ice, brine and air allow for the phases to be distinguished within μCT scans (Crabeck et al., 2016; Lieb-Lappen, Golden & Obbard, 2017).

4.2.2.1 X-ray Computed Tomography Sample Preparation

Storage conditions play a pivotal role in preserving features of sea ice, which is greatly influenced by temperature (Cox & Weeks, 1983, 1986). The storage protocols underwent initial development for the winter 2019 expedition, followed by subsequent refinements and optimisation of the protocols for the winter 2022 expedition.

One sample was collected for CT scanning from the winter 2019 pancake. On the subsequent winter 2022 cruise three cores were collected for CT scanning from the pancake floe. This allows for the evaluation of the spatial variability of the brine and air volume profiles and inclusions' properties within a pancake floe.

Ice cores were cut onboard the SA Agulhas II with the samples collected at 22WMIZ3 within 5~6 days after collection. They were cut using a circular saw in -10°C conditions, first the ice core was cut into 5 cm segments from the bottom of the core, with each segment labelled respectively. Two thick 2 cm slices were then cut through the centre of the segments and 2 cuboids were cut from the middle of each thick slice to produce 2x2x5 cm cuboids. Figure 4.5 illustrates how a thick slice of ice was cut from each hemisphere of an ice segment and further two cuboids where cut from each slice. Two to four cuboids were preserved from each segment and the cuboids were placed in labelled plastic Ziplock bags taking note of the name and orientation of the sample. Only one cuboid was CT scanned from each segment. The winter 2022 samples were maintained in -10°C conditions during transport to the University of Cape Town and a single cuboid from each segment was maintained at -10°C until it was CT scanned. The winter 2022 samples were scanned a month after returning from the expedition. Samples were scanned before being placed in -18°C storage conditions.

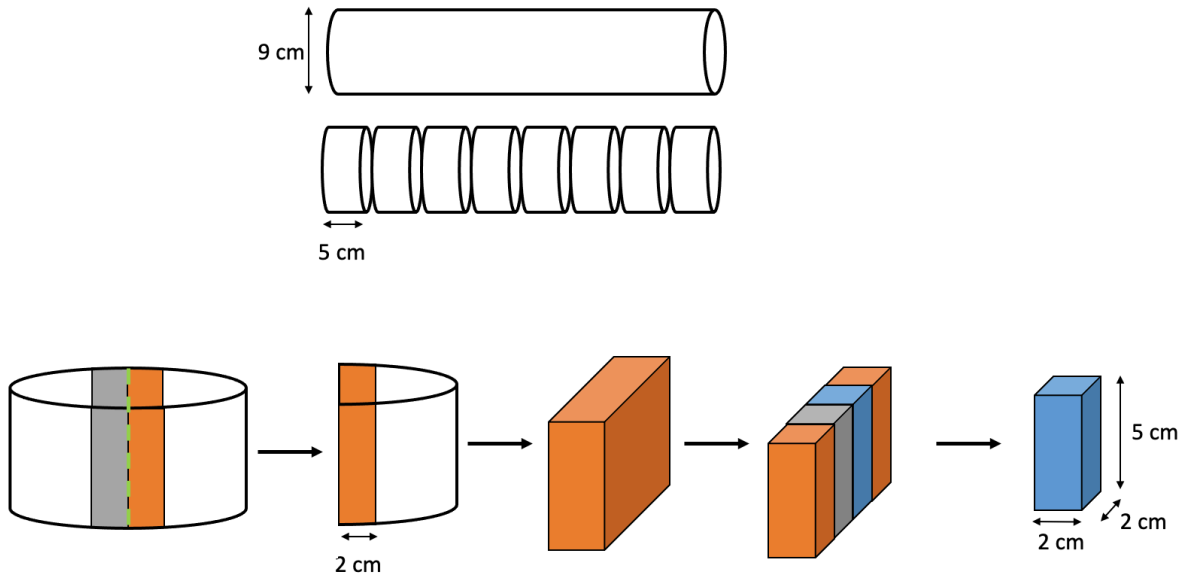


Figure 4.5: Schematic diagram showing how a core sample was cut to produce a section of sea ice for CT scanning

Ice cores collected for CT scanning during the winter 2019 expedition were stored in -18°C conditions for 3 years before the samples were segmented. Only a single cuboid was cut from

the centre of each segment using a band saw. Samples from 2019 were placed in a portable freezer with no insulation at -10°C for at least 12 hours prior to scanning of the ice.

While some studies centrifuge samples, these have a tendency to not accurately determine the air content and overestimate the brine content, especially above the freeboard (Salomon, Maus & Petrich, 2021). Centrifuging samples is mainly associated with permeability and percolation studies of the ice. This study aimed to investigate the impact of low temperature cycles on brine and air inclusions within sea ice, and therefore centrifuging would have reduced the brine content in samples and provided an inaccurate representation of the air volumes, as discussed in section 2.4.2. Ice samples in this study were therefore not centrifuged as the investigation was conducted on both brine and air inclusions and their respective distributions.

4.2.2.2 Sample Preparation for Directional Heating Analysis

Three ice cuboids from winter 2022 were then further used to test the effects of UD and MD heating on inclusion volumes and properties within the sea ice. The three cuboids were maintained at -10°C until they were scanned, then were placed in -18°C storage conditions with no insulation for four months before further investigation. The pieces were taken from a top, middle and bottom section of a winter 2022 ice core (B1) for depth variability (Figure 4.6). The sections were named as such in relation to the depth location of each sample (top, middle and bottom).The core consisted of only granular textured ice (Figure 4.6) thus there is no variability in the texture of the three samples used for heating (Figure 5.1 and Figure 5.2).

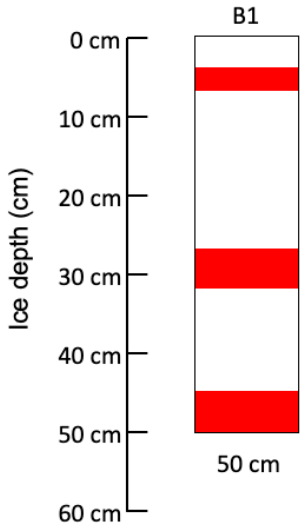


Figure 4.6: Schematic of UD and MD sample depth selection

The pieces were heated in two manners sequentially. The samples were first UD heated in dense Styrofoam holders (Figure 4.7). Samples were placed in the centre of the holders taking note of the orientation and label. The Styrofoam holder was designed to promote greater heat flux through the vertical axis of the ice as opposed heat flux from all directions. In order to further promote vertical heat flux, copper plates at -10°C are placed over the centre of the holder containing the ice. The holder containing the ice was then transferred from an environment of -18°C to a portable freezer at -10°C to acclimatize to the warmer conditions for a period of at least 12 hours prior to scanning. After samples were UD heated and scanned, the samples were cooled to -18°C for a period of at least 24 hours before being heated back to -10°C with no insulation measures to test the effects of MD heating. The MD samples were also placed in -10°C conditions for at least 12 hours prior to scanning.

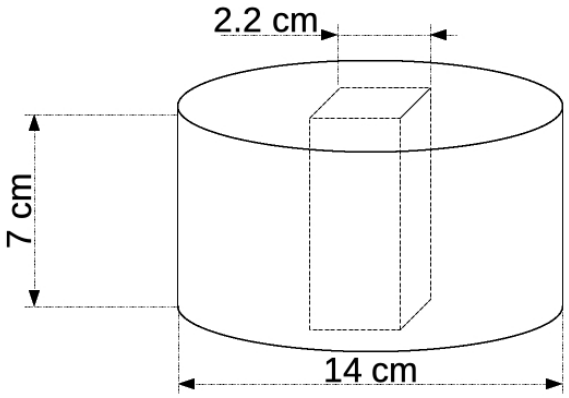


Figure 4.7: Styrofoam holder used to promote a heat flux through the vertical axis of sea ice CT samples

In this study, the choice of storage temperatures for the field samples was based on minimizing the microstructural changes associated with temperature changes (Assur, 1960; Cox & Weeks, 1983, 1986; Eicken et al., 2000). The chosen storage temperatures are reflective of temperature fluctuation observed over the duration of passing polar cyclones in the Antarctic MIZ (Vichi et al., 2019) and temperature fluctuations experienced by the sea ice within similar regions to the location of samples collected within this study (Johnson et al., 2023). Over the period of an explosive polar cyclone in the Antarctic MIZ Vichi et al. (2019) noted rapid temperature fluctuations from near melting point before returning to -15°C within the span of approximately two days. Johnson et al. (2023) back tracked trajectories of the sea ice, determining the temperatures experienced by the sea ice from winter to spring of 2019. During the winter period, temperature fluctuations were observed between approximately -10°C and -25°C. The temperatures range used within this study, of -10°C to -18°C, fall within this temperature range.

It is noted that the lower portions of the ice will not typically experience as large a temperature variation since the underlying ocean temperature does not experience such large temperature fluctuations as the atmosphere (Salomon, Maus & Petrich, 2021; Oggier & Eicken, 2022). Temperatures above -10°C were not utilized due to the larger microstructural changes observed at higher temperatures (Perovich & Gow, 1996; Eicken et al., 2000; Light, Maykut & Grenfell, 2003). Furthermore, there have been differences in storage and scanning temperatures for sea ice CT scanning studies, however studies on the impact of cooling and heating cycles on sea ice are limited (Lieb-Lappen, Golden & Obbard, 2017; Salomon, Maus & Petrich, 2021; Oggier & Eicken, 2022). The temperature conditions were chosen for this study both to provide insight into the behaviour of samples under conditions partially reflective of their natural environment and to investigate the impact of low temperature storage conditions on sea ice microstructure.

4.2.2.3 Density Measurements of µCT Scanned Samples

The density of the CT scanned samples from winter 2022 B1 core were then measured 7 months after the samples were collected. The density of each cuboid was measured after MD heating from the storage conditions of -18°C to -10°C. Samples were placed in the warmer conditions for at least 12 hours before density measurements were taken. The dimensions of each cuboid was determined using a GRIP Digital Vernier Calliper to determine the outline volume of the sample and samples were accurately weighted on a RADWAG AS 220.R2 PLUS scale. The bulk density of the sample was then determined using the standard definition of density shown in Equation 5.

$$\rho = \frac{m}{V} = \frac{m}{(l \cdot b \cdot h)_{sample}} \qquad \textit{Equation 5}$$

4.2.2.4 X-ray Computed Tomography Imaging Methodology

3D µCT scanning of sea ice samples was conducted at the X-sight Labs facility in Somerset West near Cape Town. Samples were transported from the University of Cape Town (UCT) to the scanning facility in a portable freezer set to -10°C. During the scanning process, a custom glass chamber (Figure 4.8) that allows for a circulating refrigerant, ethylene glycol, to maintain temperature at -10°C. A LAUDA10 chiller was placed next to the CT scanner, with insulated tubing fed through the scanner to the cooling chamber. The tubing is suspended above the cooling chamber in a manner that allows for the cooling chamber to rotate 360° while maintaining continuous flow of ethylene glycol from the chiller to the cooling chamber. The

chiller temperature was manually offset to -11.5°C to account for heat loss through the pipes and allow the cooling chamber to maintain a temperature of -10°C within the CT scanner.

Ice build-up occurred on the outside of the cooling chamber over the duration of each scan. This was scraped off between each scan, but resulted in the first and last projection of each scan not being exactly the same. Without dry humidity control, this factor was beyond the available control of the instrument. The resulting variations were adjusted for in post processing, as discussed below.



Figure 4.8: Cooling chamber for sea ice samples in the CT scanner

The sea ice is scanned in a Nikon Metrology XT H 255 ST Industrial CT scanner with the following parameters:

- 120 kV, 250 µA,
- 1fps
- 2 frames per projection
- 2000 projections per sample.

Each scan was conducted over a period of 66 minutes per scan. The beam energy of 120 kV was chosen to allow for penetration of x-rays through the glass, ethylene glycol mixture and sea ice while allowing for sufficient contrast of the different phases within the ice. A beam energy too low would not penetrate through the glass while a value too high would result in the liquid and solid phases not being identifiable within the scan. A beam current of 250 µm was sufficient and used in all scans. The exposure time was one fps with an average of the two frames used per projection. The angle difference between each projection was 0.18°.

The CT scanner was calibrated before each sample using a separate glass cooling chamber containing ethylene glycol at room temperature in order to create a linear reference from four radiographs ranging from no to full attenuation over a period of 4 minutes. The linear reference is then used to generate a shading correction for radiographs to convert the radiographs into projections.

A piece of Styrofoam containing a square hole slightly larger than the base of the sea ice samples is located at the bottom of the cooling chamber to secure the sea ice from the bottom during the scanning process. The Styrofoam also lifts the sea ice samples into the field of view (FOV) of the scan and above the base of the cooling chamber so that the base of the cooling chamber is not within the FOV. The sea ice samples are placed with the top of the sample orientated upwards in the cooling chamber. Another piece of Styrofoam is placed through the top of the cooling chamber to secure the samples from the top as well as seal the cooling chamber. Sea ice samples are approximately 5 cm, with the FOV of the scan around 3 cm in height. The FOV of these dimensions allows for the high resolution of the scans (21 μm) in both the vertical and horizontal planes.

The shading correction is applied to the radiographs to produce 2000 projections of the sea ice from different angles. The projections are reconstructed using Nikon's CT Pro 3D software to reconstruct the projections into a greyscale 3D model of the sea ice sample. The edges of the projections are cropped to eliminate cone beam artifacts before the reconstruction into 8-bit raw files (for the 0-255 greyscale scans of sea ice). While some studies used 16 bit grey value stacks, this study found the 8 bit raw files sufficient and more computationally time efficient. The scans produced 3D models with a voxel size of 21 μm along the x, y and z axis.

4.2.2.5 X-ray Computed Tomography Post Image Processing

The 3D reconstructions are then processed using VGStudio Max 3.5.0 software to determine the different ice, brine and air phases within the scan. A built-in adaptive Gaussian filter was first applied to the grey scale scans to reduce noise when applying the computational algorithms for thresholding of the image to determine the different phases within the sample. A smoothing factor and edge threshold value dependent on the scans was chosen between the values 1.5 and 2 and 0.15 and 0.25 respectively. The values were tailored for each scan due to slight differences in the shading gradients, which vary slightly within each scan due to the beforementioned difference in ice build-up on the outside of the cooling chamber.

The smoothing factor is linked to the noise reduction while the edge threshold value is linked to the sharpness of the shading gradients within the greyscale scan. A combination of these factors will allow for some noise reduction while maintaining the boundaries of the ice and its phases. An edge threshold that is too low will reduce the effectiveness of the smoothing factor as the sharpness of the edges will be overcompensated and no smoothing will occur, therefore a combination of both factors for each scan was determined to enhance output of the phase thresholding algorithm.

Brine inclusions within the samples were detected using one of two methods, chosen based on the brightness conformity of the 3D reconstruction of the sample. The first method tested was through the application of the VGDefX algorithm in inclusion mode, which detects voxels that are higher in density, and thus lighter in colour than the surrounding ice. This adaptive and automatic computational algorithm was used first on samples, however it was found that some samples had a brightness gradient within the sample that did not sufficiently detect brine inclusions throughout the sample. While the VGDefX algorithm is able to adapt thresholding locally, it was found that some sample gradients were too small for that algorithm to detect the gradient and visible noise was observed in the algorithm output. VGStudio Max 3.5.0 is able to apply the local thresholding method to gradients in both the vertical and horizontal planes, which adequately captures the 3D nature of the inclusions - something that has previously not been a point of focus in recent studies.

The second method was then applied to samples where brine could not sufficiently be detected using the VGDefX algorithm on the whole sample. This method runs the VGDefX algorithm within a selected region of interest (ROI) that is adjusted manually from a first iteration the of the VGDefX algorithm output. The ROI outlines borders in in which the algorithm can run, while this method selects the areas to look in, the thresholding selection for determining the phases is not manual. This method was also used for samples where VGDefX selected ring artifacts, the ROI was adjusted manually to remove the regions containing ring artifacts.

The air inclusions were detected using a computational algorithm called VGDefX in the void analysis mode. VGDefX is a sophisticated local algorithm that can adjust thresholding values for brightness variations from several probability criteria. The local thresholding algorithm can account for brightness variation in both the vertical and horizontal dimensions. The void analysis mode detects voids by looking at voxel greyscale values lower in density, thus darker in colour, than that of the surrounding ice. In some cases were darker ring artifacts were observed in samples, the same method as discussed for the brine inclusions was applied to

the air inclusions. Regions of ring artifacts were manually removed from the ROI and VGDefX algorithm in the void analysis mode was subsequently run.

The thresholding analysis for both brine and air distinguishes which voxels are part of each phase. A list of each inclusion is produced from this analysis with different properties of each inclusion that includes the diameter of the circumscribed sphere of the inclusion (mm), equivalent diameter of a sphere with the same volume as the inclusion (mm), volume of the inclusion (mm^3), the number of voxels that the inclusion consists of, surface area of the inclusion (mm^2), compactness, sphericity and projected dimensions of the inclusions along the x, y and z axes.

The diameter of each inclusion is based on the diameter of a circumscribed sphere around the inclusion and the equivalent diameter is the diameter of a sphere with the same volume as the inclusion. The compactness is determined based on Equation 6 with the volume of the sphere being the volume of a circumscribed sphere around the inclusion. Sphericity of inclusions are determined based on Equation 7, using the surface area of a sphere with the same volume of the inclusion and the actual surface area of the inclusion. The projected dimensions are the dimensions of a bounding box around the inclusion, thus the sizes of the inclusions of they were projected on the x, y and z axes.

$$Compactness = \frac{V_{sphere}}{V_{inclusion}} \qquad \textit{Equation 6}$$

$$Sphericity = \frac{A_{sphere}}{A_{inclusion}} \qquad \text{Equation 7}$$

5 Data Analysis and Results

The textural properties, porosities and inclusion size distributions based on CT analysis were taken from winter 2019 and winter 2022 pancake ice floes. The procedures followed are discussed in section 4 and the results are outlined below.

5.1 Textural Analysis

The texture of the ice can be indicative of the growth conditions of the ice (Haas, 2003; Petrich & Eicken, 2017) especially in the Antarctic MIZ where the turbulent conditions of the region result in dynamic ice growth (Allison, 1997; Weeks, 2010). Figure 5.1 shows the texture profiles of the pancake ice from winter 2019 (A2) and 2022 (B4 and B5) determined from images of cross-polarised thin slices of the ice. Most noticeably the pancake from winter 2019 was thinner and only granular texture ice was observed with Table 5.1 providing a summary of the average crystal sizes in each core. Figure 5.2 shows the crystal size profile, showing the crystal sizes across both years are within similar ranges.

Arctic or thermodynamically driven ice growth typically contains only a small portion of granular ice near the ice-ocean atmosphere (Crabeck et al., 2016; Maus, Schneebeli & Wiegmann, 2021; Salomon, Maus & Petrich, 2021) while B4 and B5 showed ~50cm of ice only containing granular textured ice. There have been observations in highly dynamic regions of the Arctic where granular-textured ice has reached up to 70 cm in some cases before columnar-textured ice is observed (Smedsrud & Skogseth, 2006). The granular-textured ice in this study highlights the turbulent growth conditions this ice was subjected to through it growth period.

Table 5.1: Summary of the average granular crystal sizes with the 95% confidence interval for the winter pancake ice from 2019 and 2022

Core ID	Core Length (cm)	Granular Crystal Size (mm)
A2	28	1.98±0.15
B4	50	1.60±0.11
B5	51	1.87±0.12

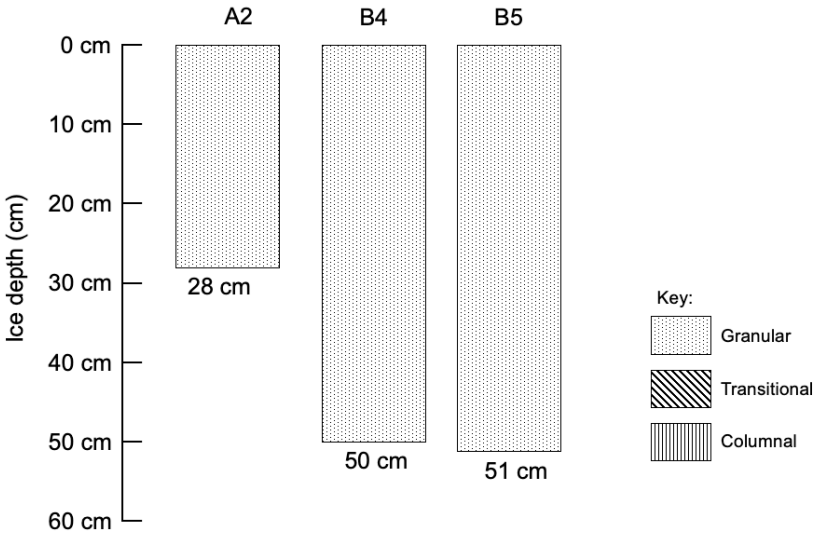


Figure 5.1: Stratigraphy diagrams for sea ice core collected from pancake floes collected during the winter 2019 and 2022

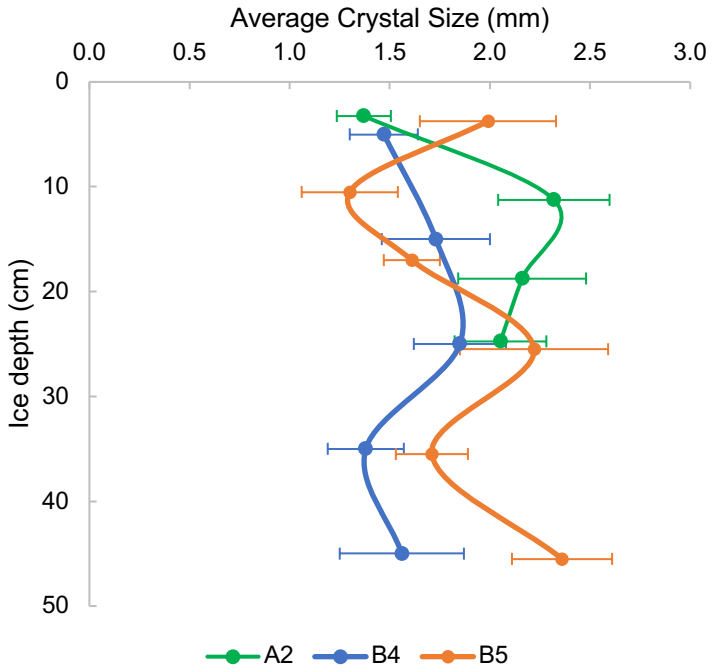


Figure 5.2: Average crystal size profile with 95% confidence intervals of cores collected during winter 2019 and 2022

5.2 Microstructural Analysis

The microstructure is a vital aspect of sea ice that influences properties such as the physical, mechanical and optical properties of sea ice (Assur, 1960; Perovich & Grenfell, 1981). Microstructural properties encompass the connectivity of pores and the distribution of brine and air inclusions. The microstructural and textural properties provide understanding into the

formation of the sea ice, its growth, mechanical behavior and response to environmental influences (Notz, 2005; Thomas, 2017; Oggier & Eicken, 2022). This study looks specifically into the porosity and distribution of inclusions within sea ice samples collected from pancake floes in the Antarctic MIZ during winter periods.

This section will outline the methodology used to analyze the data produced from the CT scans and provide results of the effects of different heating methods, a comparison of protocol methods from winter 2019 and 2022 and the spatial variability of brine and air inclusion profiles from a single pancake floe.

5.2.1 Data Analysis for µCT Scan Results

Each µCT scan produces a lengthy inventory of each brine or air inclusion and properties about the inclusion such as the volume, projected dimensions, circumscribed diameter, equivalent diameter and sphericity of each inclusion. Through use of data analysis, the properties of the inclusions could be comprehensively investigated and categorized. This allows for changing properties, either along the depth of the core, at different locations on the pancake floe or through temperature fluctuations, to be explored.

This section will outline the rationale used for the analysis of the brine and air inclusions. A python program was developed to analyze the data sets, commencing with filtering of inclusions to further reduce noise picked up by the computational thresholding method outlined in Section 4.2.2. This is followed by the classification of further subsets of the brine and air inclusions and methodology of computationally derived properties outlined in the sections below. The analysis methodology and statistical analysis was developed using the nine scans pertaining to the original, UD and MD data sets (original scans refer to the scans of samples prior to cooling down to -18°C). The analysis method was then applied to all CT scans pertaining to this study.

5.2.1.1 Inclusion Analysis Limitations

While the VGStudio Max software is able to provide a comprehensive list of the inclusions and properties of each inclusions, it is noted that some property values are limited the by the resolution of the scans and the rounded values in the output analysis.

An example of this is the rounding of the volume in mm^3 of inclusions to two decimal places, resulting in a zero volume being assigned to inclusions consisting of less than ~570 voxels.

To mitigate issues arising from this, volume are calculated based on a resolution and inclusion voxel count basis. The average difference in the porosity determined from the rounded software output values and the volume of based on resolution and voxels was 0.5% and 0.01% for brine and air respectively which accounted for 25% and 2% of the brine and air porosity respectively in some samples.

Furthermore, properties such as projected areas and surface areas of small inclusions showed this trend with values below a certain threshold being represented by a zero value. Although these properties are generated by VGStudio Max software, analysis was not conducted on them due to the inherent analysis flaws generated by the rounded values.

5.2.1.2 Noise Filtering

While the resolution of the CT scans is approximately 21µm, this study focuses on inclusions larger than ~42µm. The exclusion of smaller inclusions is due to the possibility of that these inclusions may predominantly arise as artifacts and noise of the computational thresholding algorithms rather than actual inclusions. In some scans it was observed that 34% of the brine inclusions consist of a single voxel.

Several filtering methods were considered which included filtering methods based on the volume (number of voxels), the circumscribed diameters and the projected dimensions. A threshold on the circumscribed diameter was considered. However, two times (Nyquist criterion) was not sufficient for filter based on the circumscribed diameters. However, adjusting to three times the resolution also proved insufficient as inclusions with dimensions equal to the resolutions were still present after filtering with this method. Large numbers of small inclusions in high noise samples showed inclusions with similar properties showing a four-fold increase in number densities compared to other samples.

A method of filtering out inclusions consisting of 5 voxels or less (Büttner, 2011) was tested but also found to be insufficient for scans with high noise levels, where there were inclusions with dimensions equal to the resolutions were still present after this filtering method. Furthermore, increasing the threshold up to 8 voxels (based on the cubing of Nyquist criterion as inclusion's parameters are determined on a 3D basis) was considered, however, showed an over-filtering effect in the brine of some samples (Figure 5.3). The effect of using a voxel count threshold on number densities of air and brine inclusions highlights that the MD middle samples and UD bottom samples contain the highest noise levels.

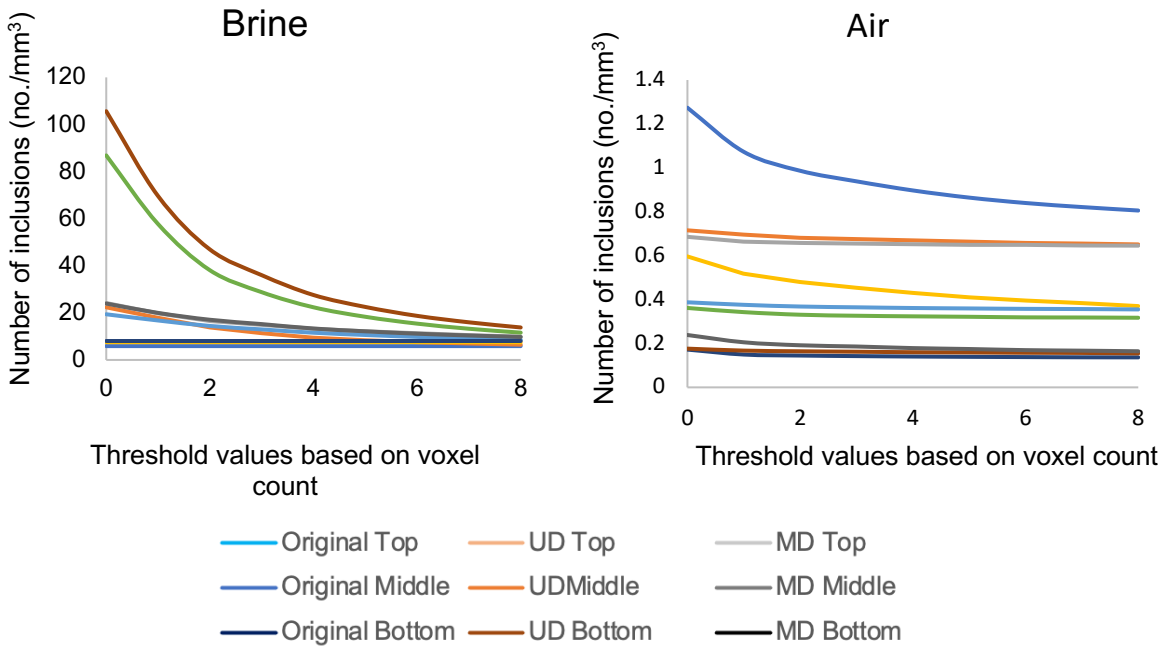


Figure 5.3: Effect of filtering inclusions based on the inclusion voxel count

A Nyquist criterion (two times the voxel resolution of 21µm) was employed for filtering noise from the samples, this method was employed by Maus, Schneebeli and Wiegmann (2021). The threshold based on Nyquist criterion was applied to the projected dimensions of inclusions to filter inclusions. The largest difference in the porosities was 0.2% and 0.001% for the brine and air volumes respectively. This method proved to be sufficient to remove small inclusion with dimensions that are less than two times the resolution. Salomon, Maus & Petrich (2021) noted a limitation within their study linked to their spatial resolution with the mode of inclusions sizes being double the resolution, therefore, reinforcing this choice of filtering method.

5.2.1.3 Inclusion Characterisation

A fundamental characteristic of sea ice is the porous nature of the ice. Studies have shown the porosity is not only an influencing factor on physical properties of the sea ice but also the distribution of the inclusions (Perovich & Grenfell, 1981; Perovich & Gow, 1996). In relation to the optical properties of sea ice, the scattering of 100 small inclusions would not be equivalent to the scatter from one larger inclusion of the same volume (Perovich & Gow, 1996). This principle is applicable to other properties such as the mechanical properties of the ice. Therefore, the distribution of inclusions is an important factor in order to understand the larger scale impacts of sea ice.

Brine inclusions were subdivided into two categories similarly to other studies (Freitag, 1999; Light, Maykut & Grenfell, 2003; Salomon, Maus & Petrich, 2021). The division of 1.0 mm was chosen based on the upper limit of plate spacing, typically 0.4 to 1 mm depending of the growth rate of the sea ice (Weeks & Hamilton, 1962; Lofgren & Weeks, 1969; Nakawo & Sinha, 1984). Similarly to Light, Maykut & Grenfell (2003), the brine inclusions are classified into tubes and pockets, however, there study arbitrarily defined tube as brine inclusion with vertical lengths greater than 0.5 mm. While Salomon, Maus and Petrich (2021) chose a classification limit of 0.7 mm (within typical plate spacing range), interpreting inclusions larger than the limit as secondary pores formed through connecting of the original brine layers. The threshold chosen for this study of 1.0 mm corresponds to the classification used by Freitag (1999) and the typical length of a brine cylinder (Weeks & Assur, 1967).

Figure 5.4 shows the effect on the brine tube parameters of adjusting the dimension length that differentiates between tubes and pockets with a range of typical brine plate spacing of 0.4 to 1 mm (Weeks & Hamilton, 1962; Lofgren & Weeks, 1969; Nakawo & Sinha, 1984). Brine tubes were defined as any brine inclusion with a projected dimensions that are greater than 1 mm, with the tube size parameter shown in Figure 5.4 relating to the projected dimensions in the x, y and z axes.

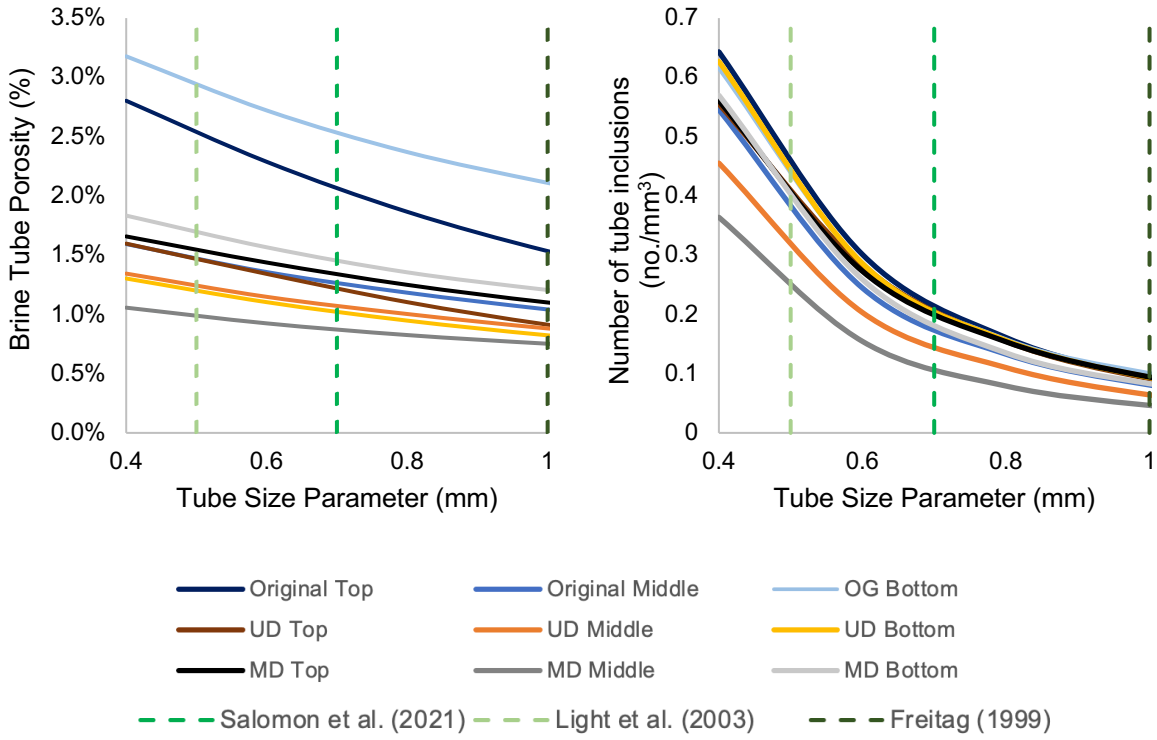


Figure 5.4: Effect of tube size parameter (mm) on the brine tube porosity (left) and number densities (right)

Brine tubes were classified as inclusion with projected dimensions on either the x, y or z axis. The choice of using all 3 axes accounts for the variation in the shape of brine inclusions seen in granular textured ice (Büttner, 2011; Oggier & Eicken, 2022). Ice growth in dynamic conditions is characterised by it granular-dominated texture (Eicken et al., 1997) as evident in textural analysis of the ice cores pertaining to this study (Figure 5.1). The shape of brine inclusions of granular and columnar ice has shown to be characteristically different (Büttner, 2011; Oggier & Eicken, 2022). This is the underlying rationale of not only characterising brine tubes along the z axis, as typically elongated pores are not observed in granular-textured ice. Therefore, limiting inclusions to dimensions previously established for columnar ice would not encompass the granular nature of the ice observed in this study. The distribution of which inclusions have projected dimension over 1.0 mm in the x, y, z or combination of these are illustrated in Figure 5.5 for the Original top, middle and bottom pieces of ice. This demonstrates that some inclusions are not larger than 1.0 mm along the z-axis, but are greater than 1.0 mm in either x, y or both these axes. Consequently, tube parameters typically associated with z-axis length for columnar ice is not sufficient for granular ice.

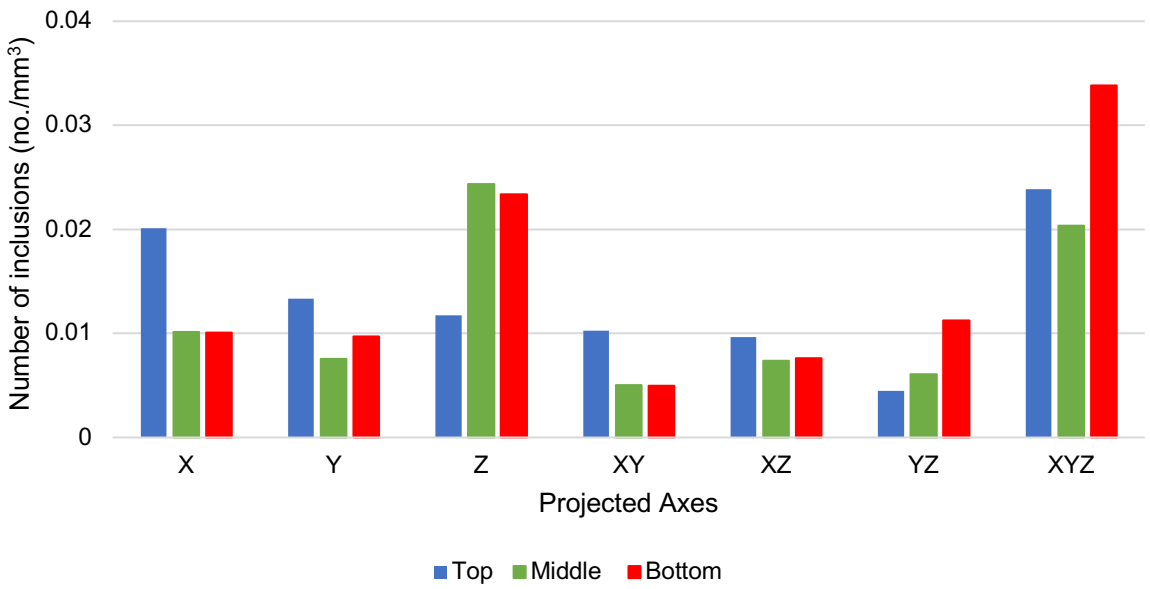


Figure 5.5: Number densities of brine tube inclusions that have projected lengths dimensions over 1 mm on the X, Y, Z or combination thereof axes

Studies on the porosity of sea ice have historically been focused on the brine as air porosity has been considered negligible or subjected to the same processes as brine (Worster, 1992; Feltham et al., 2006; Crabeck et al., 2016). A comprehensive description of the distribution of air inclusions within sea ice is limited. Crabeck et al. (2016) suggest the air porosity of sea ice is a function of both gas saturation and brine volume. Crabeck et al. (2016) further distinguishes air inclusions into micro (< 1mm), large (1mm < D < 5mm) and macro (> 5mm)

air inclusions based on the diameter of inclusions in the transverse plane. These diameter threshold limits were applied in this study, with the exception of the limitations were applied to the circumscribed diameters of the air inclusions in 3D space. The resolution of Crabeck et al.'s (2016) study along the horizontal (x and y) axes was 97.7μm while the resolution along the vertical axis is 600 μm. The resolution of the scans within this study is not limited to larger vertical resolutions and maintains a 21 μm resolution along all axes. Therefore, the diameter thresholds for air inclusion established by Crabeck et al. (2016) was expanded into the 3D space within this study.

Properties and distributions of the inclusions such as average projected dimensions, average sphericity, number density, volumes, size distributions of inclusions for brine, air or subsets of those inclusions can then be determined using the properties determined from VGStudio Max 3.5.0 output as described in section 4.2.2.

5.2.1.4 CT based Salinity and Density Measurements

The CT-based density (ρ_{bu}) and salinity (S_{bu}) are derived from thermodynamic phase equilibrium and CT-based brine and air porosities at the scanning temperature of -10°C. The third order polynomial fit for the salinity of brine (S_{br}) in sea water is given by Equation 8 (Assur, 1960). This relationship shows good correlation for the temperature range used within this study (Notz, 2005), and is based on the thermodynamic equilibrium. The bulk salinity (S_{bu}) of the sample is then determined based on the methodology employed by Notz, Wettlaufer & Worster (2005), with the exception of solid fraction ($Ø_i$) is based on CT analysis rather than impedance (Equation 9).

$$S_{br} = -1.20 - 21.8\,T - 0.919\,T^2 - 0.0178\,T^3 \qquad \textit{Equation 8}$$

$$S_{bu} = S_{br}(1 - \emptyset_i) \qquad \textit{Equation 9}$$

The salinity measurements from the winter 2019 A3, A4 and A5 cores was available for comparison to the CT-based salinity measurements determined from the A1 core. (The salinity measurement of the B6, B7 and B8 cores were unavailable due to logistical reasons at the time of this dissertation.) Figure 5.6 shows the results of the salinity profiles with the depth presented on a percentage basis to account for the variation in core depths (Table 4.2). The profiles do not show similar trends with an average 37% difference in the values, with only overlapping values around 60% depth within the cores. The salinity measurements were taken at a larger resolution of ~10cm per segment in comparison to the ~5 cm segment used in the

CT cores. Despite this, the A1 core for CT analysis was ~10-20 cm shorter than the salinity cores (A3, A4 and A5), resulting in a similar number of segments in each core. In the subsequent winter 2022 salinity cores were cut into smaller 5cm segments for a higher resolution. The samples sizes of the salinity segments of the winter 2019 and CT samples differ significantly which could account for some variation, however, it is recommended for future work the samples used for CT analysis also be used to measure the salinity for a more accurate comparison of the measure and CT-based predictions for salinity.

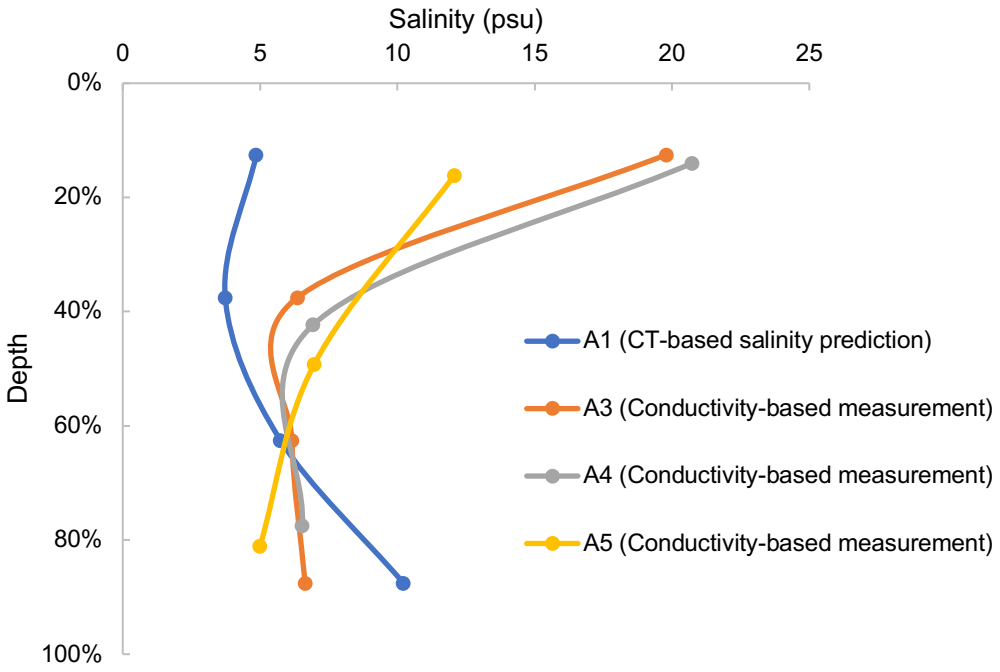


Figure 5.6: Salinity profiles of the winter 2019 cores based on conductivity measurements (A3, A4 and A5) and salinity derived from CT-based brine and air volumes

The density derived from CT scanning uses the density of the pure components and fractions of the brine and ice (the contribution of air density on the total density of samples was considered negligible) shown in Equation 10. The density of the brine is a function of temperature, salinity and pressure. The density of brine is a weak function of temperature but a strong function of the salinity, with Equation 11 showing a less than 2% error for temperatures down to -20°C (Notz, 2005) at atmospheric pressure. The density of the ice is determined based on Equation 12 outlined by Pounder (1965).

$$\rho_{bu} = \phi_{\mathrm{i}}\rho_i + \phi_{\mathrm{b}}\rho_b \qquad \textit{Equation 10}$$

$$\rho_b = 1000.3 + 0.78237S + 2.8008 \cdot 10^{-4}S^2 \qquad \textit{Equation 11}$$

$$\rho_i = 916.8 - 0.1403T \qquad \textit{Equation 12}$$

The density of winter 2022 CT cuboids were measured as outlined in section 4.2.2 which are compared to density calculations based on the brine and air porosities determined through CT analysis. The measured and CT-based profiles generally show similar shapes with the CT-based profile showing an average 6% higher density values (Figure 5.7). Salomon, Maus & Petrich (2021) noted a range of density differences between CT-based and hydrostatical weighing densities with the largest discrepancies mostly noted above the freeboard in which they classified open air inclusions as having previously been brine. This is a relatively large differences noted in this study could be attributed to the volume determination derived from the dimensions of the sample for the measured density values. It is recommended for future work to explore a more accurate methods of volume determination of samples or density measurements method such as hydrostatic weighing.

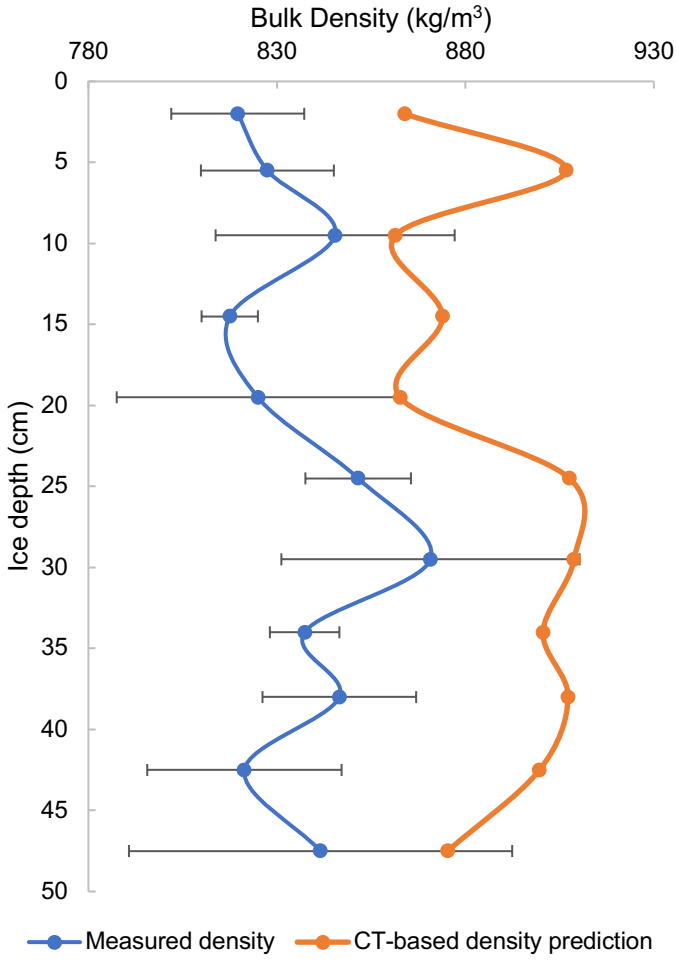


Figure 5.7: Density profiles of the winter 2022 B1 core for density based on cuboid dimensions and weighting (blue) and the density based on the brine and air volumes observed in CT analyses.

5.2.1.5 Statistical Analyses

Statistical analysis serves as a tool to assess the significance of difference between different data sets in order to provide meaningful deductions by evaluating whether observed variations in data are likely due to random chance or indicative of significant differences. Analysis of variance (ANOVA) were used to determine if there are a statistically significant difference between data sets within this study unless otherwise stated. Two factor ANOVA test can be used to determine if there is a statistical difference between the samples before and after experiencing low temperature storage conditions and between the UD and MD heating methods. The two factor method was incorporated to account for the variation in the original parameters of the samples (original top, middle and bottom samples), however, the statistical focus was on the P-values associated with the variation in the heating methods (and not the location of the sections).

The Central Limit Theorem (Islam, 2018) can be used to statistically determine if there is a difference in the average dimensions of data sets given that the size of the data sets are large enough irrespective of the standard deviation. Given the substantial sizes of the data sets in this study (~68000 to ~292000 inclusions per scan which is well above the general rule of 30 (Islam, 2018)) and fairly consistent standard deviation observed. This study allows for the assessment of the differences in the average dimensions of the inclusions, despite potential underlying variability.

5.2.2 Directional Heating Results

The procedure followed is outlined above in section 4.2.2 and 5.2.1, with 2D greyscale images generated from the CT scans shown in Figure E.1. Figure 5.8 shows the total porosity in the ice sections before the low temperature cooling (Original) and after UD and MD heating. The sections were taken from a top middle and bottom section of an ice core and are further named in this section as such as discussed in section 4.2.2. The thermal sequence was applied in order to investigate the effects of low temperature storage and different heating methods on the brine and air porosities and the inclusion size distributions. It is noted that there are slight differences in the field of view's (FOV) heights for the CT scans which resulted in residual mismatch between the scans of each depth, although these were not considered significant especially for the smaller inclusions that are more uniformly present across the samples.

Generally, there is a decrease in the total porosity from the original scans to the UD and MD heated scans, with the exception of the UD middle sample showing a slight increase which

will be discussed in more detail later in this section. A two-factor ANOVA test showed that overall there was no significant statistical difference in the total porosities of the original, UD and MD sections. Although, on average the samples had a 22% reduction in total porosity after being subjected to low temperature conditions (UD and MD).

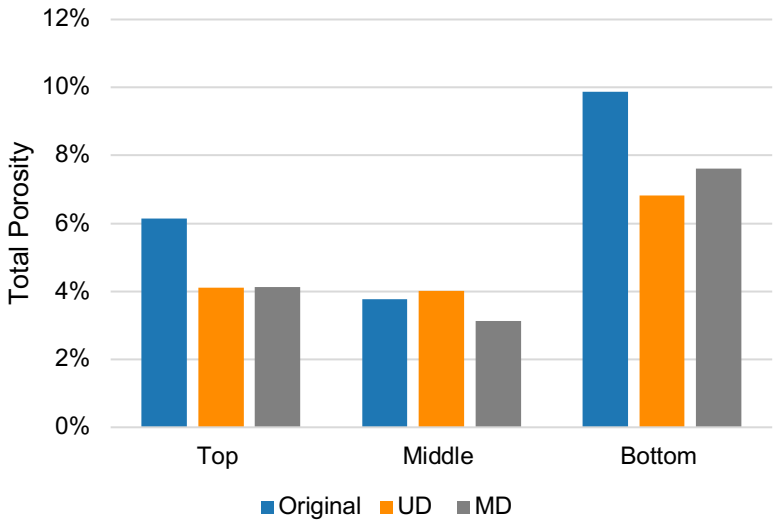


Figure 5.8: Effects of heating on the total porosity of sea ice from the top, middle and bottom section of an ice core

The reduction in total porosity is primarily attributed to the reduction of brine porosity. A statistically significant difference in the brine porosities was observed (Figure 5.9). Lower brine volumes were observed after a cooling and heating sequence, indicating that the cooling and subsequent heating of samples does affect the measured brine porosities. These findings correspond to Cox and Week's (1986) theoretical hypothesis of reducing brine porosity through thermal cycling, although they suggested in most cases the decrease would not be significant, which is not the case with these findings.

Brine porosity reductions are observed through both the UD and MD thermal sequence (Figure 5.9), however no statistically significant difference was noted between the heating methods. The brine porosities appear to show the greatest reductions in samples with the largest initial brine porosities, however more samples would be required to quantify this relationship. The average of the UD and MD brine porosity reductions after the low temperature storage were 46%, 26% and 51% for the top, middle and bottom section respectively. These are well above the theorised maximum reductions of 15% predicted by Cox and Week's (1986). The greater reductions observed in samples with higher initial brine volumes could indicate that ice with higher brine porosities has a greater tendency for brine drainage to occur during the heating sequence, however this is not supported by evidence of large increases in air porosity with

one exception, the UD middle sample, where the increase in air porosity exceeds the decrease in brine porosity.

Although both heating methods resulted in a reduction of brine porosity, there is no apparent difference between either method. The top and bottom sections showed a greater reduction in brine porosities under UD relative to MD, 3% and 15% relative difference in top and bottom sections respectively. While the middle section showed a greater reduction in the MD sample, with an 18% reduction difference between the MD and UD. An average reduction of 41% in both the UD and MD brine porosities was observed across the three samples with a 0.2% difference between the heating methods.

In contrast to the brine, the samples showed no significant statistical difference in the air porosities from before to after being subjected to the thermal sequences (Figure 5.9). The air porosities after cooling and heating in the top and bottom sections of the core showed a slight decrease. The middle section of the core showed an increase in the air porosity, which coincides with the appearance of a macro air inclusion (Figure E.3) that is seen in both the UD and MD sample that was not initially present. The macro air inclusion could have formed due to partial melting of the sample, which is further discussed in conjunction with observations of other properties within the middle sample thermal cycles.

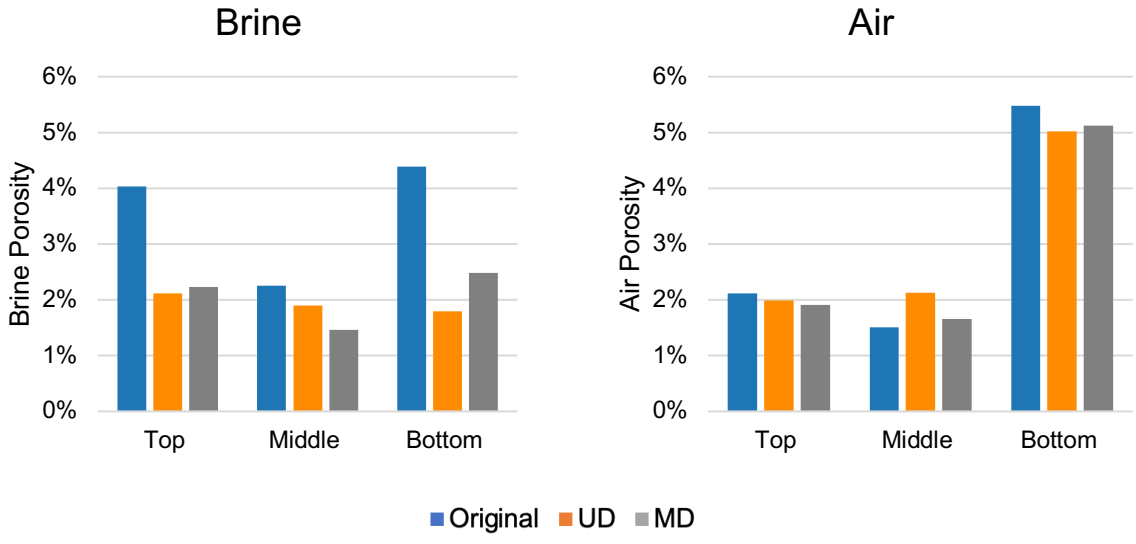


Figure 5.9: Effects of heating on the brine and air porosities from a top, middle and bottom section of an ice core

Visual analysis of the 3D reconstruction of the air inclusions in the scanned samples shows a large volume of macro air inclusions in the ice section taken from the bottom of the core (Figure E.3). Crabeck et al. (2016) exclusively observed macro inclusions near the ice-atmosphere

interface in the snow ice layer, noting a decreasing air porosity with depth. This indicates that possibly a portion or the entire volume of the macro air inclusions in the bottom section of the ice may be attributed to brine drainage during sample collection. The macro air inclusions accounts for approximately 75% of the air volume in the bottom sample. The bottom of the sample would have been near the ice-ocean interface where the ice is near its melting point and higher brine volume is generally associated with higher permeability (Perovich & Gow, 1996; Petrich, Langhorne & Sun, 2006; Golden et al., 2007) hence the higher potential for brine drainage to occur during sample collection.

Further investigation into the impact of low temperature cycles and heating methods on inclusion volume distributions and number densities was made. The number of brine inclusions increases (Figure 5.10) from the samples maintained at -10°C relative to the UD and MD samples. The Original samples contained an average of 7.1 brine inclusions per mm^3 to 10.4 and 10.9 inclusions per mm^3 for the UD and MD samples respectively. An increasing number density of brine inclusions with depth is observed in the Original samples, a trend which is maintained in the UD heated samples. While the MD heated samples show the highest number density in the middle sample followed by the bottom sample. However, it is important to note that the bottom UD and middle MD sample contained the highest noise levels prior to the data filtering previously mentioned. While a statistical analysis shows no statistically significant difference in the brine inclusion number densities across the heating sequence, there is an clear observed increase (Figure 5.10). The statistical indifference is attributed to the high variability between samples of each heating method.

Eicken et al.'s (2000) detected brine number densities of 0.62-1.05 inclusion per mm^3 at -10°C with lower resolutions than used in this study. Despite the lower resolution, the brine number densities are comparable to number densities in this study for larger inclusions with dimensions above the resolution of Eicken et al.'s (2000) study. Salomon, Maus & Petrich (2021) noted comparable number densities to this study at similar resolutions (25μm) with the exception of the middle MD and bottom UD samples having slightly larger number densities of 13.1 and 15.2 inclusion per mm^3 respectively. Even higher densities have been noted by Light, Maykut & Grenfell's (2003), with number densities of 24 inclusions per mm^3, with higher resolutions and a longer storage period.

The increase in brine number density after low-temperature cycling alludes to the notion that brine number densities were affected by the past temperature fluctuations experienced by the ice, and this was consistent across both UD and MD samples. While studies using lower storage temperatures have typically reported higher number densities as compared to

samples maintained at higher temperatures (Perovich & Gow, 1996; Light, Maykut & Grenfell, 2003; Salomon, Maus & Petrich, 2021), this is not definitive evidence that cyclic low temperature storage increases brine number densities. The observed increase in brine number densities (Figure 5.10) through heating and cooling proposes the notion that the division of brine inclusions during cooling is greater than the coalescing of brine inclusions during a warming sequence within the temperatures ranges used in this study.

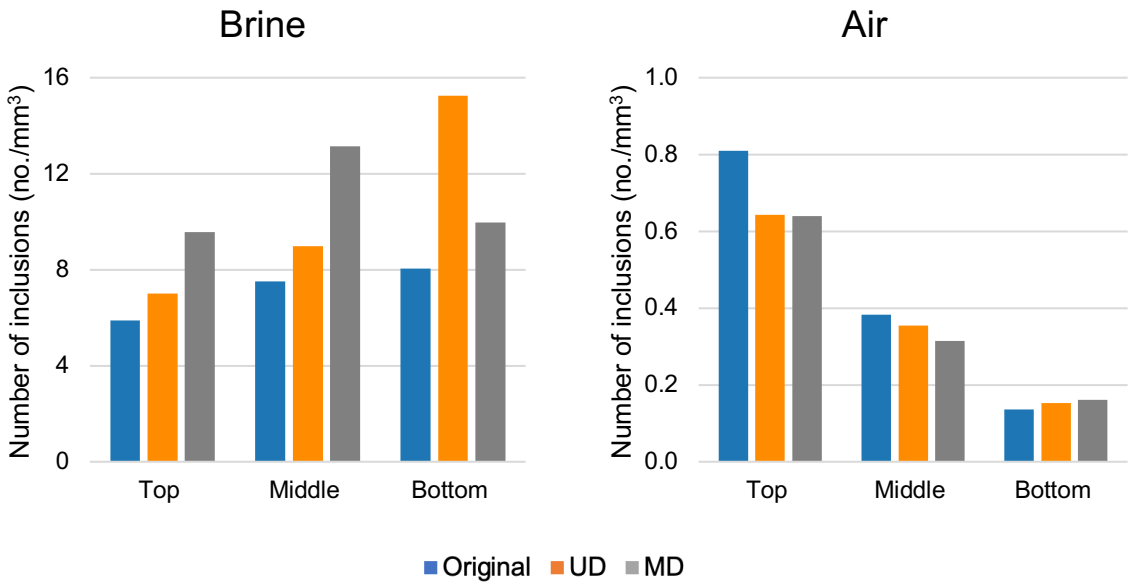


Figure 5.10: Effects of heating on the number of brine and air inclusions from a top, middle and bottom section of an ice core

The number of air inclusions is significantly lower than the number of brine inclusions, with the average number of brine inclusions being 38 times larger than the number of air inclusions within the 9 scans evaluated in this section. This is well above the range noted by Perovich and Gow (1996) at ~3 times as many brine inclusions as air inclusions near the top of artificially grown pancake ice. Salomon, Maus & Petrich (2021), with a similar resolutions and lower storage temperatures than Perovich and Gow (1996), observed air number densities between 0.2 to 1 air pores per mm^3. Values in this study are within the range observed in the top and middle samples, while the bottom sample falls slightly below the range around 0.15 air inclusions per mm^3. As mentioned previously, there are macro air inclusions in the bottom sample potentially due to brine drainage and this might have resulted in some of the air bubbles present in the brine being removed, reducing air inclusion number density. The observed air number densities in this study are lower than the air number densities near to 1.3 air inclusions per mm^3 observed by Light, Maykut & Grenfell (2003). Variations in number densities may be due to the higher measurement resolution or physical aspects of the ice such as depth, ice type or texture.

A slight decrease in the air number density is observed in the top and middle sections of the ice while the bottom sample showed a slight increase in the number of air inclusions (Figure 5.10). The observed trend in the top and middle sample coincide with Light, Maykut & Grenfell's (2003) observations of disappearing air inclusions during cooling and no nucleation during a heating sequences. The bottom sample shows an increasing number density trend which could suggest that gas saturation is a factor influencing air number densities. The upper regions of the ice would experience supersaturation of gas, inferring that bubble nucleation is less likely during cooling (Grenfell, 1983; Crabeck et al., 2016). Nucleation of air inclusions in samples with lower saturation factors (associated with lower regions of sea ice) during temperature reduction is more likely. This could potentially explain the slight increase in air number densities observed in the bottom sample after low temperature cycles as opposed to the higher regions.

Despite postulating justifications for the marginal inconsistencies of air number densities through a low temperature cycle, a statistical analysis determined the difference in air number densities to be insignificant. Therefore, further investigation would be required to determine the effect of storage conditions of the air number densities of different gas saturation levels as this is beyond the scope of this investigation.

Delving further into the geometric properties of brine inclusions, Figure 5.11 shows the changes to the volume distributions of brine inclusions preceding and subsequent to the low temperature cycles. (Figure 5.11 displays a stepwise representation of brine volume distribution, employing progressively increasing bin sizes while maintaining logarithmically uniform intervals. This was chosen to mitigate erratic fluctuations associated with a fixed bin sizes, that was particularly evident in the larger volume region. The selection of the number of bins was determined in order to maintain the observed trend in number density with a constant bin size.) A noticeable decrease in the number density of the inclusions with larger volumes (~>0.0004 mm^3) is observed and significantly larger number densities of smaller inclusions are seen across all three depths. While the number of brine inclusions increases, there is a decrease in to total brine volume through the thermal cycles, due to the reducing number of larger brine inclusions (~>0.0004 mm^3, excluding a few of the largest inclusions) and increasing number of smaller inclusions (Figure 5.11).

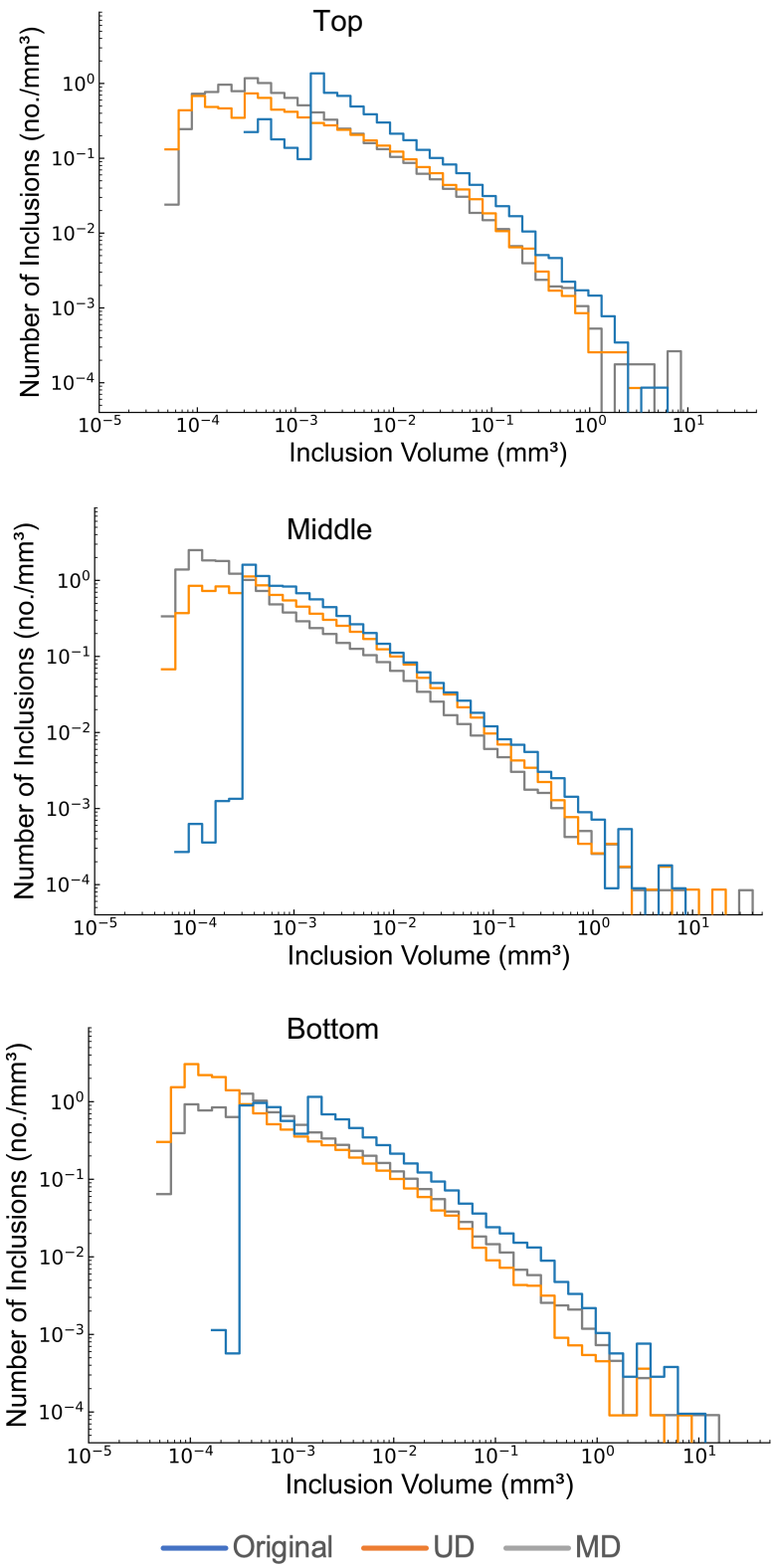


Figure 5.11: Histograms of brine inclusion volume distributions for the top, middle and bottom sections with different heating methods

The data in Figure 5.12 illustrates the identical data set depicted in Figure 5.11, but its utilisation of a boxplot format effectively highlights the changes in the interquartile ranges and inclusions with the largest brine volumes. The number densities and volume of inclusions

larger than 1 mm^3 do not show a consistent trend before or after the low temperature thermal cycles. In the top and bottom sections showed a slight decrease in the upper brine inclusion volume limit for the UD samples followed by an increase brine inclusion upper volume limit for the MD samples. The middle sample showed an increase in the brine inclusion volume upper limit through each thermal cycle that was larger than both the top and bottom sample. This in addition to the formation of the macro air inclusion in the middle sample could suggest this sample may have experienced melting the during sample handing resulting is the macro air inclusion forming.

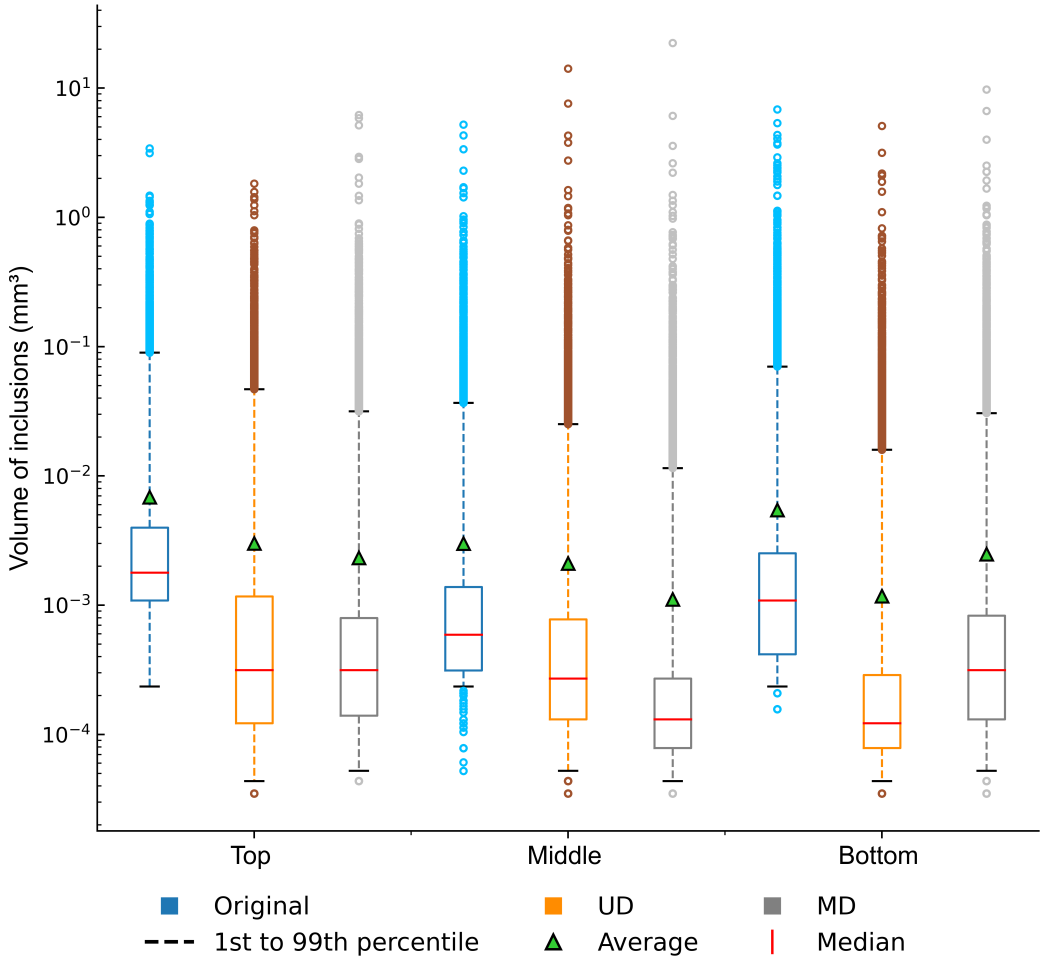


Figure 5.12: Box and whisker diagram of brine inclusion volume distribution

In order to test the effects of UD and MD heating, the projected x and y dimensions were averaged since both the x and y axes are in the transverse plane and unidirectional heating promotes a heat flux along the vertical (z) axis. Therefore averaging the two x and y dimensions would provide a general view of the properties in the horizontal plane such as the changes in the vertical and horizontal planes.

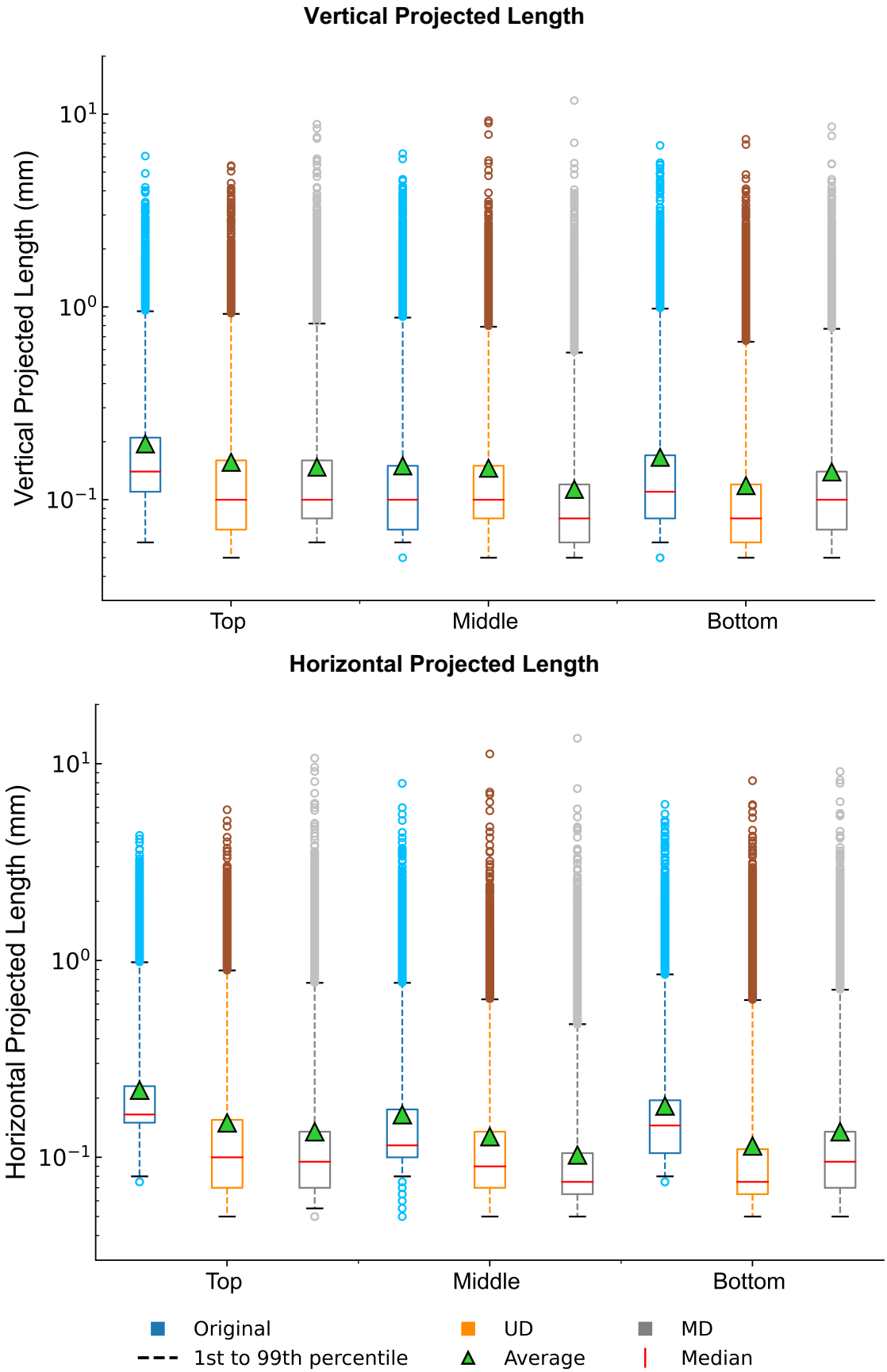


Figure 5.13: Box and whisker diagrams of brine inclusion projected length distributions

It has been hypothesized that elongated brine inclusions break down into smaller more spherical inclusions from non-uniform shrinking of the radii of cylindrical shaped brine inclusions due to thermodynamic instabilities (Grenfell, 1983). The samples used in this study contains ice dominated with granular-textured which does not contain the typical brine tube like structures elongated along the vertical axis that is associated with columnar-textured ice (Büttner, 2011; Oggier & Eicken, 2022). The low temperature thermal cycles showed a shift in the dimensions of the inclusions compared to the distributions prior to the low temperature cooling. There is an observed differential shift in the horizontal which shows a statistically significant difference in the average horizontal dimensions over the thermal sequence (Figure 5.13). However, there is no visual or statistically significant difference between the two heating methods.

Light, Maykut & Grenfell (2003) noted during a heating sequence the vertical dimension increased faster than the horizontal dimensions in columnar dominated landfast ice. Though the samples in this study only contain granular ice, the vertical dimension showed the smallest length reduction. This could suggest the dimensional changes of inclusions may be linked to the sample dimensions, thermal cycle temperatures or heating resulted in the greatest changes in the vertical dimension resulting in those dimensions showing the smallest change through a thermal cycle while the horizontal dimension did not increase to the same extent during heating.

The differential shift in the vertical and horizontal dimensions corresponds to a decreasing sphericity in the bulk of the inclusions throughout all depths (Figure 5.14). The brine inclusions showed a decrease of 15% in sphericity after the low temperature thermal cycles with only a 0.02% difference between the heating methods. This further supports previous results that the low temperature cycle had a greater impact than the different heating methods within this study. As previously mentioned, Grenfell (1983) hypothesized the non-uniform shrinkage of cylindrical brine inclusions forming smaller and more spherical inclusions. While the increased brine number densities indicate a breakdown of inclusions, there sphericity shift suggests the thermal cycle used in this study falls within the phase of decreasing sphericity with an incomplete breakdown of brine inclusions. A total breakdown to only smaller inclusions did not occur in within the temperatures or storage period used in this study.

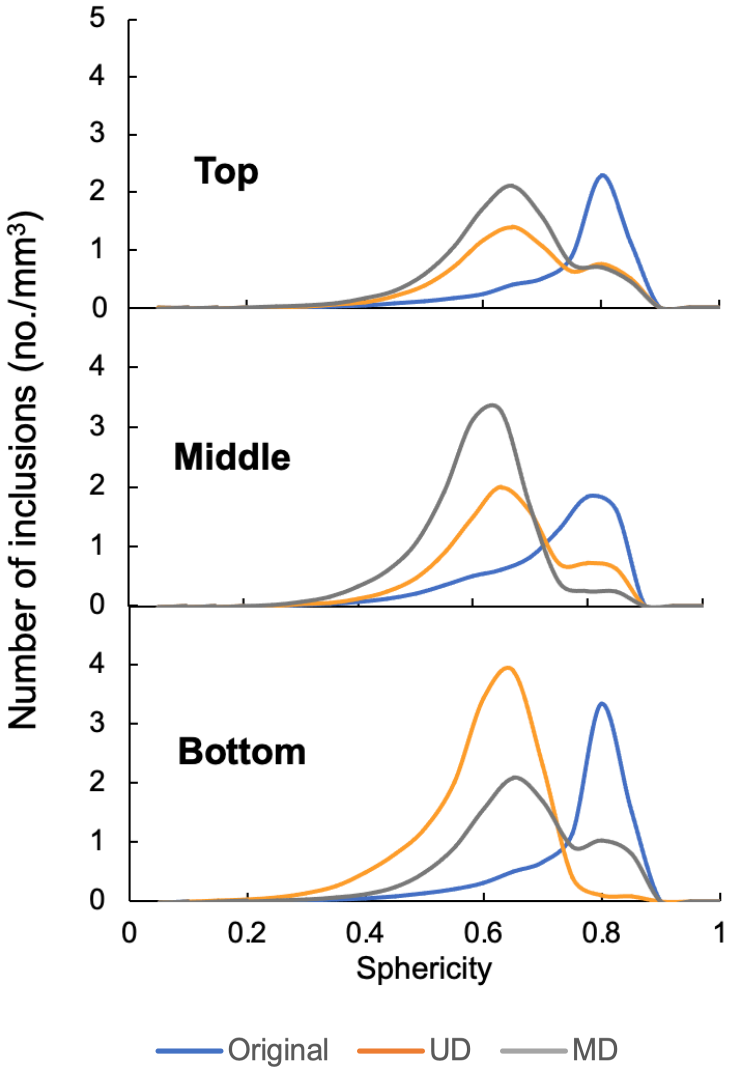


Figure 5.14: Effects of heating on the sphericity of all the brine inclusions from a top, middle and bottom section of an ice core

Air porosity is dependent on the brine porosity (Crabeck et al., 2016), therefore the impact of low temperature thermal cycles on the size distribution of air inclusions is also a key aspect to investigate within this study. The air inclusions as previously mentioned show smaller changes in comparison to the brine phase. Micro air inclusion are the most abundant size category with the total air inclusions reflecting that of the micro air inclusions (Figure 5.10 and Figure 5.15). Consequently, the previously discussed impact of saturation profiles on air inclusions number densities would apply to the micro air inclusions with the air volumes of the micro air inclusions following the trend of the micro air number densities. The large air inclusion volumes and number densities are relatively constant with the slight variations in number densities at this scale could potentially be attributed to the inclusions within the FOV. The air volumes show almost no change in the top sample with a slight variation in the bottom sample and an increase in the air volume of middle sample due to the appearance of a macro air inclusion after low temperature storage. The samples on average contain 2-3 macro air inclusions per

sample thus variations at this scale in the number densities can be considered negligible as the FOV may be a limiting factor determining the connection of macro inclusions.

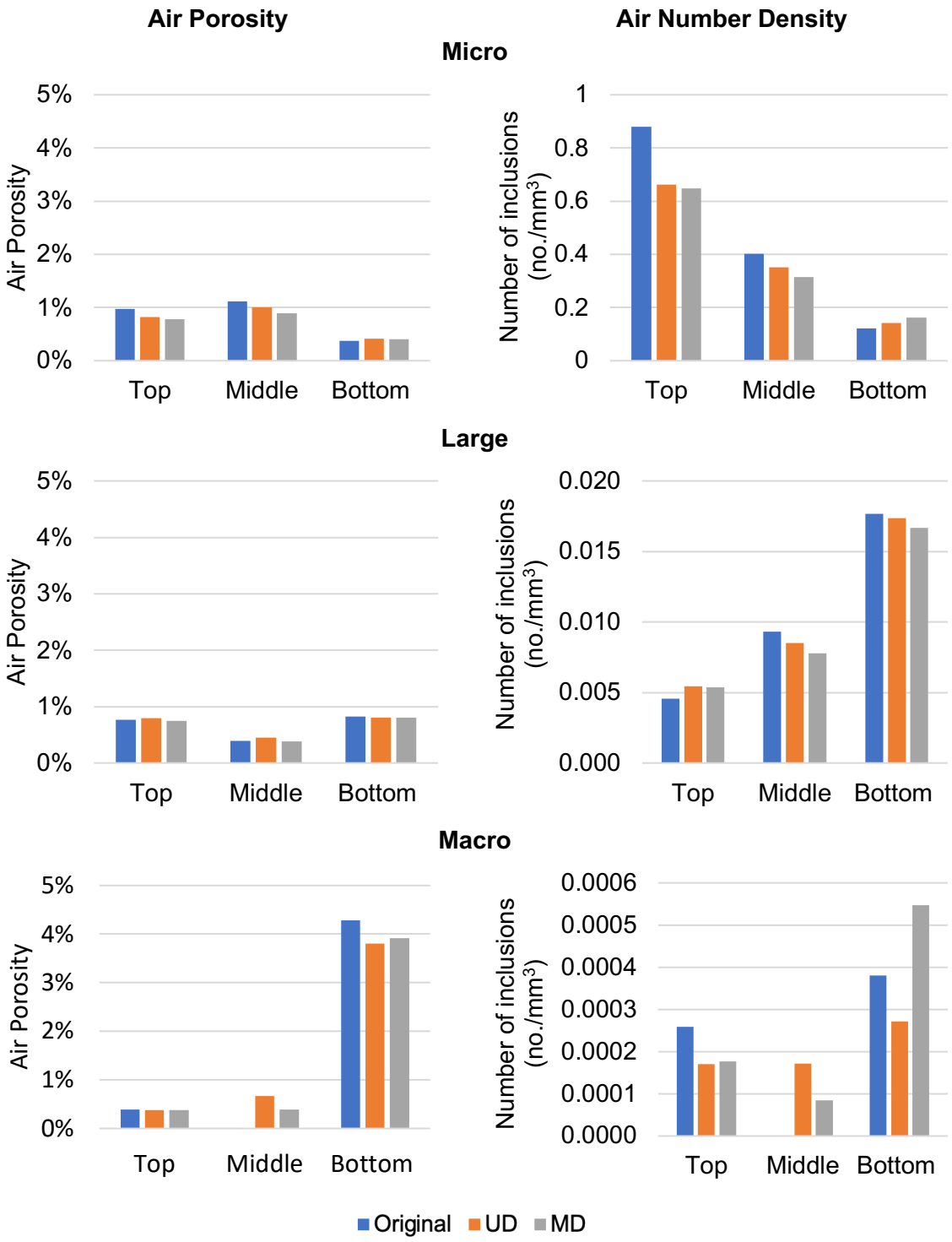


Figure 5.15: Effects of heating on the air porosity and number densities of the micro, large and macro air inclusions from a top, middle and bottom section of an ice core

This suggests that the low temperature cycles mainly effect the micro air inclusion number densities which are is not statistically significant with a minimal impact on the air porosity.

Furthermore there is no significant change in the shape or sphericity of air inclusions unlike the brine inclusions (Figure E.4).

The impact of low temperature storage conditions and different heating methods on the brine porosity and interrelated factors of sea ice samples shows compelling evidence that brine porosity is significantly affected by low storage temperatures. These impacts are greater than those predicted by Cox & Weeks (1986). The brine volumes show a range of 16% to 59% reductions across the samples with an average reduction of 41% in brine porosity from the original samples to the ones after experiencing lower temperature storage. The number of brine inclusions was observed to increase, although not statistically significantly, which could be attributed to the high variance across the depths for each sample, however, studies with lower temperature storage have noted higher brine number densities (Light, Maykut & Grenfell, 2003; Salomon, Maus & Petrich, 2021). However, the influences of UD and MD heating from -18°C to -10°C show no distinct differences in granular-textured ice between these heating methods.

In contrast, the low temperature cycles appears to have a small but not statistically significant effect on the air porosity and air number densities. The air inclusion showed small decreases in the air number densities of the top and middle sample while the bottom sample showed a slight increase, with the differences potentially being attributed to the gas saturation due to the variation in depth the samples.

A statistically significant difference is noted in the average horizontal dimensions of the brine inclusions over the thermal sequence. This differential shift in the horizontal and vertical dimension is further supported by an observed decrease in sphericity of the brine inclusions after the low temperature cycle due to the dimensional reductions not being similar. In a schematic by Grenfell (1983) illustrates the non-uniform shrinkage of the radius of cylindrical inclusions resulting in a period of decreased sphericity. This study suggest there is some breakdown of inclusions but the temperatures used in these low storage temperature cycles and the duration of these low temperature cycles does not result in the total breakdown of inclusions into more spherical inclusions.

The presence of a statistically significant difference in the average horizontal dimensions may stem from methodological constraints due to the dimensions of the CT samples chosen as the length and width of the samples are shorter than the height and the initial cooling sequence had no insulation around the samples prior to the UD heating. These horizontal dimension alterations through the first cooling sequence may have led to changes in the samples that

rendered the subsequent heating methods to show similar results. The alternations were irreversible through the first cooling and UD heating sequence due to the reduction in the brine volume being significantly greater than expected. While the reduction the brine porosity may be a function of the sample size, the significant reductions are well above the changes predicted by Cox & Weeks (1986).

These results are comparable to studies on the impact of low temperature cycles on ice-cream. Low temperature cycles on ice-cream have shown a greater effect on microstructure than ice-cream maintained at higher temperature conditions. Additionally, the microstructural changes began diminished over a series of low temperature cycles (Flores & Goff, 1999). Sutton, Lips & Piccirillo (1996), using aqueous fructose solutions, showed the recrystallisation rates of the unfrozen phase were dependent on the ice-phase volume and temperature. This supports the results of this study where lower initial brine volumes in sea ice samples had smaller brine porosity reductions and could explain why the MD results showed similarities to the UD results due to the greatest impact occurring in the first low temperature thermal half cycle.

These results allude to the notion that the brine porosity is more affected by simply decreasing storage temperatures than heating methods, however this theory warrants caution based on methodological constraints within this study. The significant reduction in brine porosity is greater than previously predicted, but the extent of the salt expulsion from samples could be linked to the size of the sample and larger samples may show smaller proportional reductions. The duration of storage, samples sizes, and cooling methods may all also influence the degree of alteration and further investigation will be necessary to quantify these factors.

5.2.3 Comparison of Winter 2019 and 2022 Protocols and Results

The Antarctic MIZ is a highly dynamic region expressing a high degree of spatial and temporal variability (Hobbs, Bindoff & Raphael, 2015; Vichi et al., 2019). Evaluating the microstructural properties of Antarctic ice samples is challenging due to this high variably, especially when the conditions of the ice growth are unknown. There are methods to back-track the synoptic conditions during the sea ice growth to relate to the smaller (centimetre-millimetre) scale properties of the ice (Johnson et al., 2023), however, this is beyond the scope of this investigation. This section will provide a comparison between ice cores from two different years that were subjected to different storage conditions by analysing the differences in brine and air porosities, the number density of inclusions, volume and sphericity distributions of the cores collected during the winter 2019 and 2022 expeditions.

The most prominent disparity between the 2019 and 2022 samples is depth of the cores with A1 and B1 being 20 and 50 cm long respectively. This suggests that the pancake from winter 2022 had a longer growth period before sampling or was subjected to colder growth temperatures. Figure 5.16 shows the temperature profiles of cores collected from the winter 2019 (A3-A5) and winter 2022 (B6-B8) pancakes, with noticeably higher temperature in the 2022 cores. The winter 2019 temperature cores showed a linear profile with the bottom of the ice just below the freezing point of the ocean water. The winter 2022 cores showed C-shaped profiles of warming ice which correlates to the higher atmospheric temperatures at the time the samples were collected (Table 4.1). Although the B1 core was collected during the winter growth period, the relatively high atmospheric temperatures near the melting point of sea ice occur in regions where polar cyclones pass over the ice (Vichi et al., 2019; Johnson et al., 2023). The pancake from station 22WIN3 was collected during a melting period of the ice after the passing of a polar cyclone as evident by the atmospheric temperature profiles of the winter 2022 B6, B7 and B8 cores.

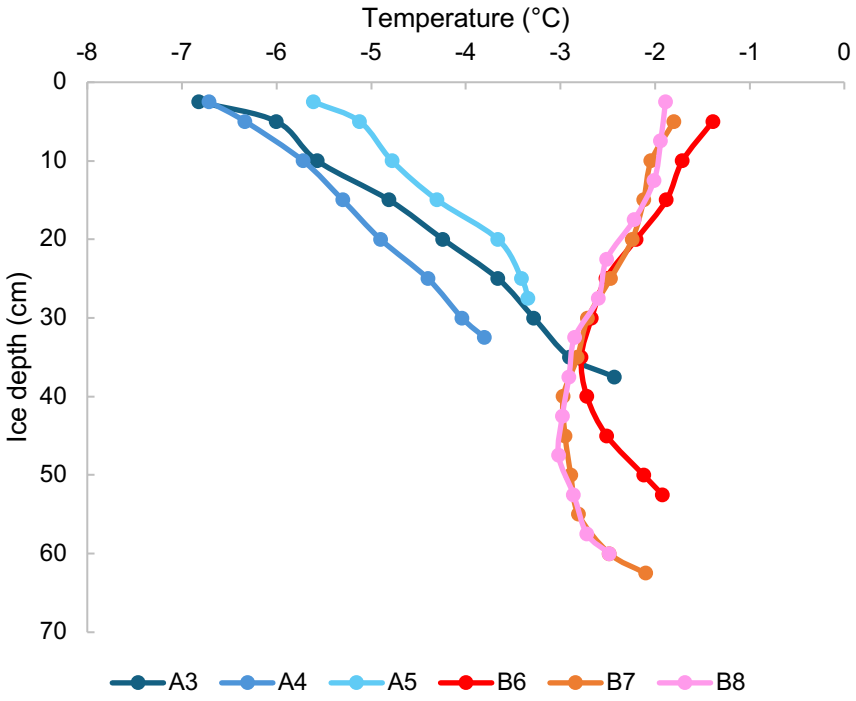


Figure 5.16: Temperature profiles of cores collected from the winter 2019 (A3-A5) and winter 2022 (B6-B8) pancakes

A similarity in the cores collected for textural analysis (A2, B4, B5) from both years show only granular-textured ice. This is attributed to the dynamic nature of the MIZ leading to the formation of pancake ice (Wadhams, Lange & Ackley, 1987; Weeks, 2010). The pancake floes

collected from both 2019 and 2022 were unlikely to have experienced quiescent environments, which would have been evident if columnar-textured ice was present (Petrich & Eicken, 2017). The morphology of brine inclusions is influenced by the ice texture, therefore, differences in brine inclusions characteristics would not be attributed to the texture profile of the sea ice.

The winter 2019 and 2022 CT samples where all scanned at -10°C, however, the 2019 brine porosity profile is generally lower compared to the brine porosity of the winter 2022 core (Figure 5.17). As discussed in section 5.2.2, brine porosity has been shown to reduce by an average of 41% after low temperature storage, indicating the A1 core may have had a higher brine porosity if it was maintained at higher temperatures prior to CT analysis as was conducted for the winter 2022 samples. The average brine porosities of the A1 (winter 2019) and B1 (winter 2022) cores showed similar values with over lapping confidence intervals (Table 5.2). This is due to the higher brine porosity in the bottom region of the core and significantly fewer CT scans associated with the A1 core that inflated the average brine porosity of the A1 core. Visually the A1 core shows lower brine porosity values with both cores showing an increase in brine porosity in the sections at the bottom of the cores (Figure 5.17). With the exception of the bottom section of the A1 core, the A1 core showed an average 42% lower brine porosity compared to the B1 core. The sections at the bottom of the A1 and B1 cores (winter 2019 and 2022 respectively) had the highest brine porosities. This is expected as the skeletal layer at the bottom of the ice is a highly porous region allowing for advective brine exchange (Petrich & Eicken, 2017). The A1 bottom section had a higher brine porosity but lower total porosity compared to the section at the bottom of the B1 core. The bottom of core B1 might have had a larger brine porosity *in situ* but the lower brine porosity during analysis that can be attributed to brine drainage. This is evident by the large air porosity in this section, atypical of ice near the ice-ocean interface (Crabeck et al., 2016).

Table 5.2: Average brine and air porosities of cores from winter 2019 (A1) and winter 2022 (B1)

Core	Average brine porosity (%)	95% Brine porosity confidence interval	Average air porosity (%)	95% Air porosity confidence interval
A1	2.29	1.59	2.02	1.06
B1	2.63	0.58	3.86	1.33

It is apparent that the air porosity of the A1 core is lower than what is seen in B1 (Figure 5.17) with the A1 core having an air porosity 48% lower than the B1 core. The air porosity has not shown a significant change after low temperature storage therefore this sample, the A1 core may have a lower air porosity due to the specific nature of that core's ice growth. This being said it should be noted that there is a possibility of greater brine drainage, especially above

the freeboard, in samples maintained at higher temperature due to the higher permeability associated higher temperatures (Perovich & Gow, 1996; Petrich, Langhorne & Sun, 2006; Golden et al., 2007). The B1 core was significantly longer than the A1 core, thus the ice depth of freeboard would be larger which could account for the higher air porosities in the upper region of the ice. The lower region (with the exception of the very bottom section) of the B1 core showed similar air porosity ranges to those in the A1 core. This suggest the freeboard could account for the higher air porosity in the B1 core compared to the A1 core, since the air porosity did not show a significant change through low temperature storage cycles. (section 5.2.2)

Storage conditions influence properties of the ice as seen in section 5.2.2, however, there are other factors during sea ice growth that influence these properties which cannot be decoupled within the scope of this investigation. The generally lower brine porosity measurements in the A1 core may be attributed the colder conditions in which the samples were collected. The lower brine porosity can also potentially be attributed to a number of environmental factors prior to the potential impacts of storage such as a lower growth rate or lower *in situ* temperatures (Figure 5.16) resulting in greater brine expulsion. Salomon, Maus & Petrich (2021) noted higher brine porosity profiles on sampling days with higher atmospheric temperatures. The B1 core showed a distinctive upper region of larger air porosity most likely due to freeboard conditions more distinctive in thicker ice, which may also play a role in the air porosities observed. The pancake from winter 2019 was thinner, therefore the region for brine drainage is smaller with no apparent freeboard compared to the winter 2022 B1 core.

The number of brine inclusions within the A1 and B1 cores are fairly consistent with no distinctive depth trend, similarly to Salomon, Maus & Petrich (2021). As discussed previously in section 5.2.2, there is an increase in the average number of brine inclusions after low temperature storage, however the high variability in the number densities statistically concludes no differences in the brine number densities. Despite the A1 core generally having a lower brine volume to the B1 core, the average number of brine inclusions in the A1 core are slightly lower than the B1 core (Table 5.3). However, the confidence intervals for the number of brine inclusions in the A1 and B1 cores are overlapping suggestive of similar number densities. The slightly lower number of brine inclusions in the A1 core may be attributed to the storage time period as more salt may have been expelled over time. Hambrock (2021) noted decreasing salinities of sea ice cores within increasing storage periods. The lower brine porosities observed in core A1 and lower number densities compared to the B1 core, suggest the greater extent of salt expulsion during long storage periods, thus reduced number of brine inclusions. Since the A1 core was stored over a longer period, for

which greater reductions in salinity have been observed (Hambrock, 2021), there is a greater possibility that a number of smaller inclusions below the spatial resolution could be present. This coupled with the filtering method could result in a greater possibility of underestimating the brine porosity of the A1 core in comparison to the B1 core, accounting for the lower porosity in the A1 core.

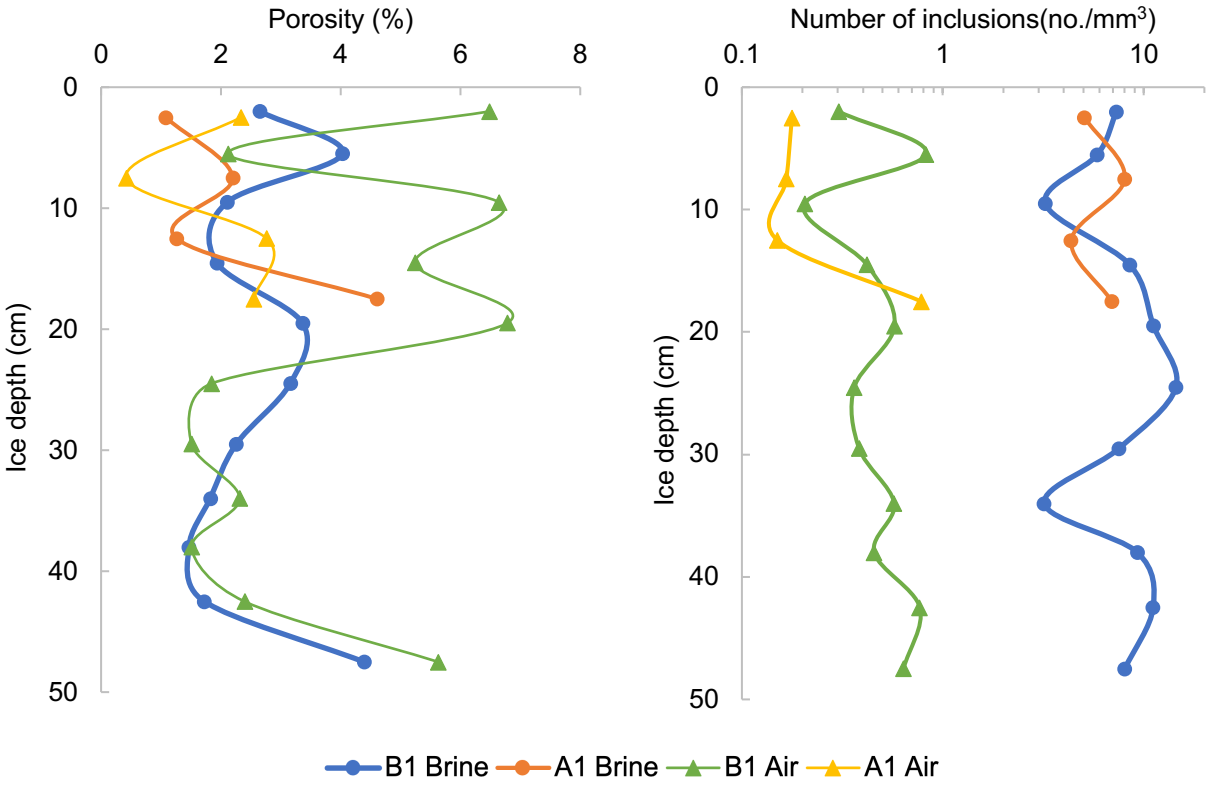


Figure 5.17: Brine and air porosity (left) and number density (right) profiles of cores collected from the winter 2019 (A1) and winter 2022 (B1) pancakes

The number of air inclusions within the B1 core remained relatively constant, with a slightly larger range of values at the top of the core, which is within a similar range to Salomon, Maus & Petrich (2021). The A1 core has a lower average air number density but relatively wide confidence interval due to bottom section of the core having a significantly higher air number density and the core consisting on significantly fewer scan in comparison to the B1 core (Table 5.3). While there is overlapping confidence intervals for the air number densities (Table 5.3), only the bottom section of the A1 core has an air number density within the range of the B1 core (Figure 5.17). Factors that may have influenced this observation include the higher temperatures in the B3, B4 and B5 cores that may have resulted in higher air numbers due to the higher permeability of sea resulting in more brine drainage, thus increased number of air inclusions. The A1 core showed the highest air number density at the bottom of the core with lower number densities towards the ice-atmosphere interface (Figure 5.17). As noted in

section 5.2.2, the upper sections of ice showed a slight decrease in the number of air inclusions but the opposite trend in the bottom region, hypothesising a possible link between the gas-saturation, temperatures and the air number densities. The majority of air inclusions consist of micro inclusions, therefore the greater difference in air number densities in the upper section of the A1 and B1 cores could be a result of a longer storage period of the winter 2019 core (A1). While the bottom section of the A1 core with the highest brine porosity has the highest air number density due to the nucleation of air bubbles in colder temperatures (Tsurikov, 1979) of sub-saturated regions in the ice. Several factors may have contributed to the differences in the air number densities trends of the A1 and B1 cores, these include the storage period, storage temperatures and sea ice growth conditions.

Table 5.3: Average brine and air number densities through the depth of cores from winter 2019 (A1) and winter 2022 (B1)

Core	Average Brine Number Density (no./mm^3)	95% Brine Number Density confidence interval	Average Air Number Density (no./mm^3)	95% Air Number Density confidence interval
A1	6.10	1.65	0.32	0.30
B1	8.15	1.99	0.50	0.11

The brine porosity profile of the core is generally lower in the A1 core but the brine number density profiles are similar between the A1 and B1 cores. The sphericity distributions of the A1 and B1 cores are dissimilar (Figure 5.18). The texture of the cores are both granular, thus, dissimilarities are not due to ice-texture differences. Section 5.2.2 discussed the impacts of low temperatures storage and heating methods on brine inclusions, showing a decrease in the sphericity of inclusions after lower temperature storage irrespective of heating methods. This trend is further expressed in a comparison of the sphericity distributions in the A1 and B1 cores. The A1 core had generally lower sphericities than what was seen in the UD and MD samples. The differences in the sphericity distribution of the A1 and B1 cores further supports the theory that low temperature storage reduces the sphericity of the brine inclusions in granular-textured ice. Hambrock (2021) observed not only a general decrease in salinity of ice cores with longer storage periods, but also the deformation of ice cores with time. The cores become less cylindrical with time. The deformation of the cores may have been a result of the changing shape of the brine inclusions over time resulting brine migration and structural changes in the sea ice samples as seen by the reducing sphericity of samples with low temperature storage. Therefore, the extent to which the inclusions change could be related to the size of the CT samples and the storage period. The A1 core was stored in -18°C conditions prior to cutting the core into cuboids for CT analysis, which may also account for some of the variations between the sphericities observed in the UD and MD samples and the A1 core.

The difference between the brine volume distributions of the A1 and B1 cores shows a similar trend to samples analysed before and after low temperature storage. The volume distribution shows larger numbers of the smaller inclusions (~>0.0003 mm^3) in the A1 core compared to B1 core (Figure 5.19), further supporting the suggestion that there is a breakdown into smaller brine inclusion through low temperature storage. The A1 and B1 core show a similar range of brine number densities (Figure 5.17) with the A1 core showing larger numbers of the smaller brine inclusions (~>0.0003 mm^3), the lower brine porosity of the core may contribute to why the A1 core does not have a higher range of brine number densities than the B1 core.

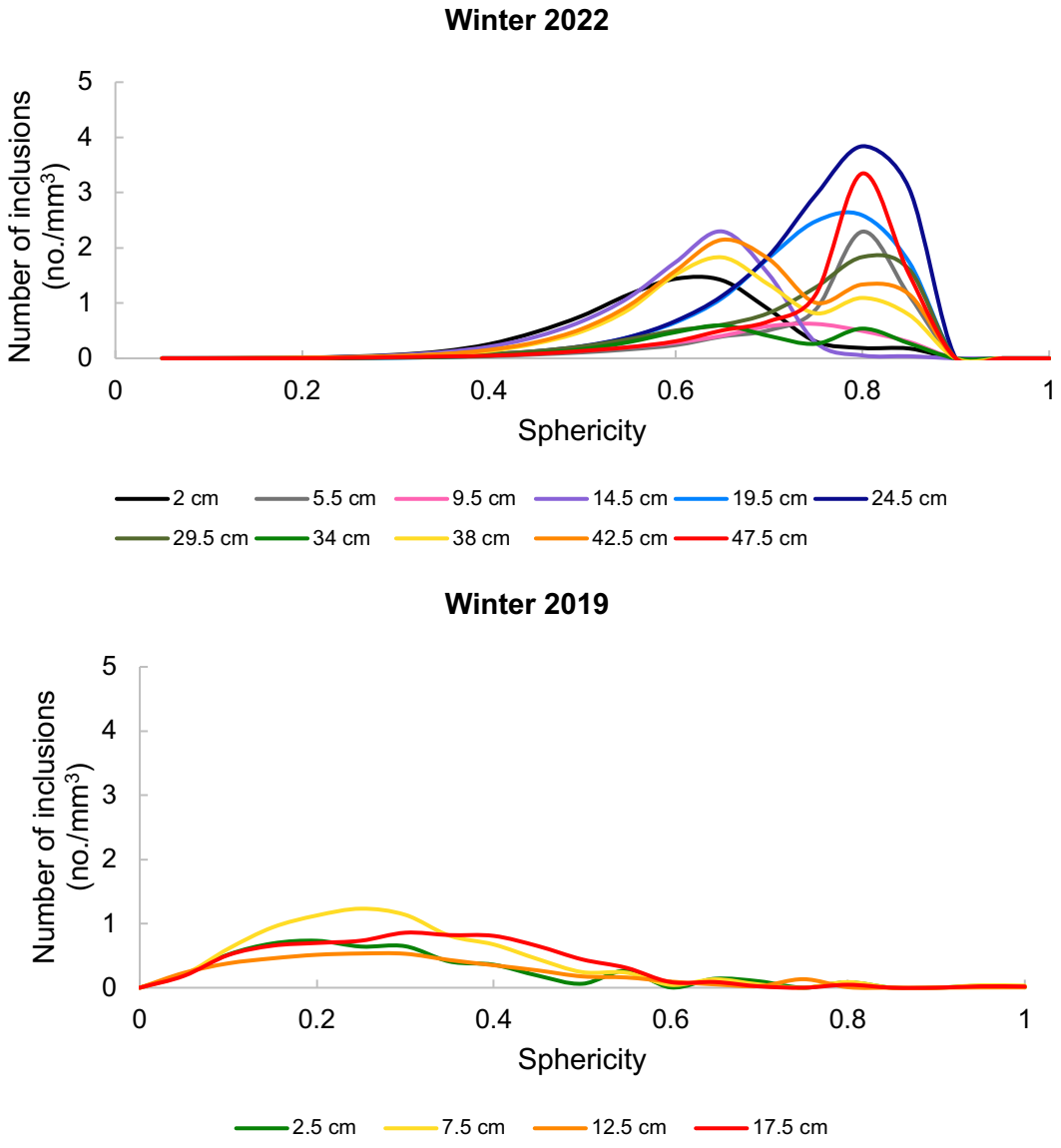


Figure 5.18: Sphericity distribution of brine inclusions within the B1 (top) winter 2022 core and A1 (bottom) winter 2019 core at varying depths

A comparison of the CT analysis results of ice cores from pancake floes collected during winter 2019 and winter 2022, show similar trends to the results observed before and after the low temperature cycles in section 5.2.2. The winter 2019 (A1) core was stored in -18°C conditions prior to CT scanning at -10°C, while the winter 2022 (B1) samples remained in -10°C prior to scanning. The difference in storage protocols is evident in a comparison of the brine porosities, volume distributions and sphericity distributions, that are comparable to the trends seen on the samples analysed before and after low temperature cycles.

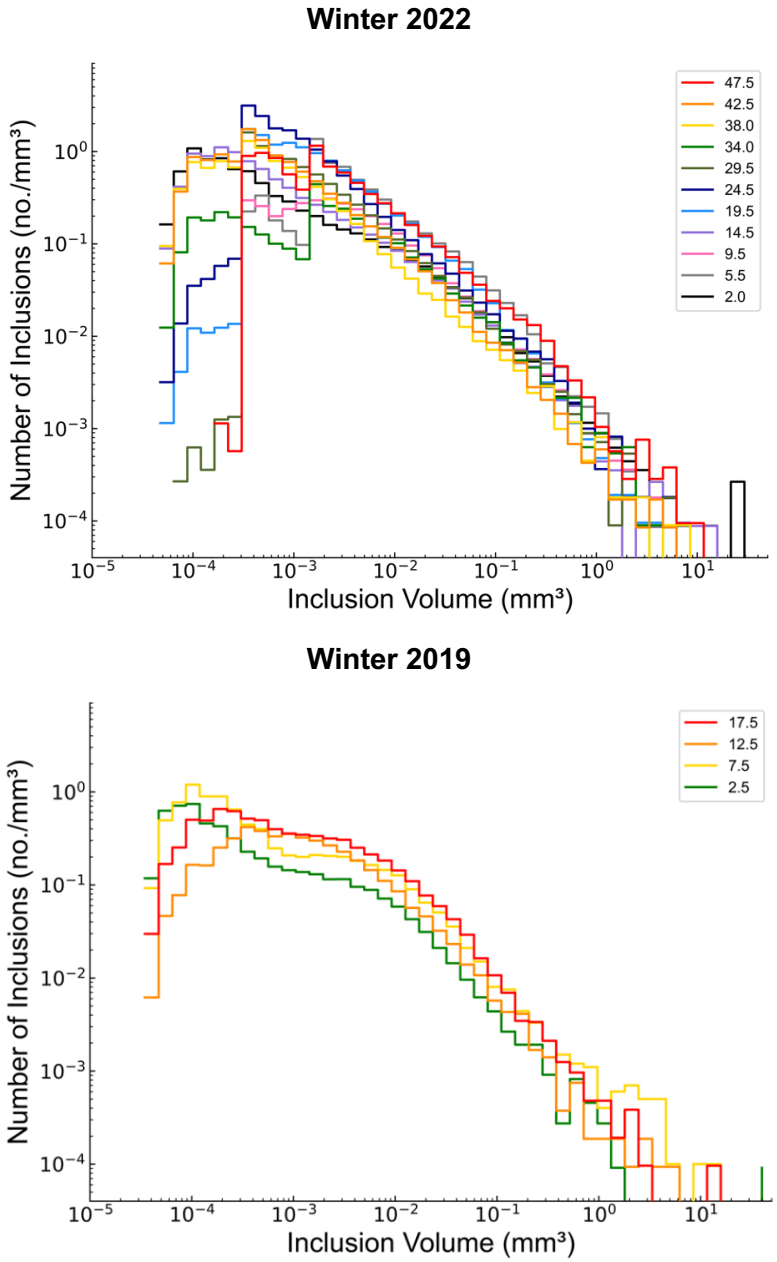


Figure 5.19: Histograms of brine inclusion volume distributions for the winter 2022 (top) and winter 2019 (bottom) at varying depths (cm)

The average brine reductions observed through the low temperature storage can be used to correct the brine porosities to values expected prior to low temperature storage and allow for a comparison between 2019 and 2022 microstructures of the ice. The extent to which the sphericity and brine porosities change with the size of sample and the time period in lower temperature storage is not determined in the scope of this study. However, section 5.2.2 can be used to calibrate the 2019 brine volumes for a more accurate comparison sea ice microstructural properties between winter 2019 and 2022. In addition, it is recommended analysis of the synoptic history of the ice be conducted as these conditions would have an influence over the structural properties of the ice for a more in-depth analysis of the effect of environmental conditions .

5.2.4 Spatial variability of inclusions profiles in a pancake floe

A comparison of the brine and air properties within ice cores from the winter 2022 expedition were based on the cores from a single pancake floe collected at station 22WIN3. The cores were collected at varying locations in order to observe the impact of spatial distribution on the inclusion volume profiles within a single pancake floe. The temperature profiles of cores collected from the 22WIN3 pancake are illustrated in Figure 5.16 with C-shaped profiles, reflective of warming ice. This is indicative of the atmospheric temperatures during the time of collection (Table 4.1). The texture of both cores analysed showed granular-textured ice, corresponding to the dynamic growth conditions of sea ice in the Antarctic MIZ.

The B2 and B3 cores noted soft snow that was not taken into account for when measuring the depths of brine and air inclusion profiles due to the snow's malleability. These cores, which were located closer to the edge of the pancake floe (Figure 4.3), were ~5-10cm longer than the B1 core located further from the edge of the pancake. This slight difference in height can be attributed to the dynamic growth conditions and ridging of the pancake near its edges (Wadhams, Lange & Ackley, 1987; Lange et al., 1989).

The B3 core is located nearest the edge of the pancake floe, thus within the ridging region of the pancakes near the perimeter, which could account for the highest air porosity at the ice-atmosphere interface. The B3 core showed a 23% air porosity at the ice-atmosphere interface, while all other CT analysis of the winter 2022 cores showed air porosities below 13% and brine porosities reaching a maximum of 4.6%. The highly air porous region near the ice-atmosphere interface of the B3 core is attributed to a large portion of macro air inclusions (Figure G.4), suggesting the consolidation of snow based on the 3D reconstruction of the air phase in this section (Figure G.4). However, it may also have been a result of brine drainage above the

freeboard (which can be distinguished by the $\delta^{18}O$ values, which were unavailable at the time of this dissertation).

All three (B1, B2 and B3) cores had macro air inclusions throughout the depth of the cores (Figure G.2, Figure G.3 and Figure G.4), with larger air volumes than observed in winter 2019 (Figure G.1) and typical air volume profiles in sea ice (Crabeck et al., 2016; Salomon, Maus & Petrich, 2021). These higher volumes could have resulted from the non-linear temperature profile with temperatures close to the melting point of sea ice (Figure 5.16), atypical of first year ice during winter conditions (Figure 2.3). The increasing air porosity in the bottom sections of the B1 and B3 cores is most likely due to brine drainage in those regions. The B2 core showed relatively higher air porosities in the bottom ~30 cm of the ice, suggesting this region was highly permeable while the B1 and B3 core had more permeable regions at lower depths. This is based on a comparison of the shape of the macro air inclusions in these regions (Figure G.2, Figure G.3 and Figure G.4).

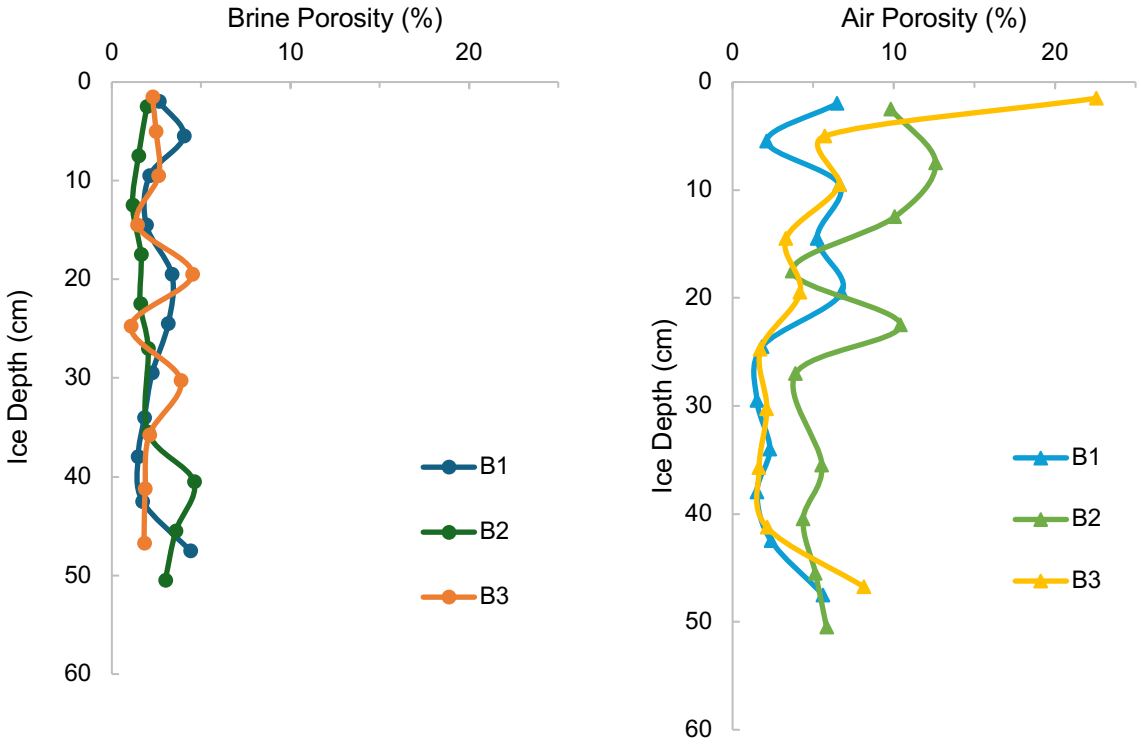


Figure 5.20: Profile of brine (left) and air porosities (right) from a single pancake floe at varying locations within the floe collected during winter 2022

The B1, B2 and B3 cores all generally appear to have a region of higher air porosities above ~25cm (Figure 5.20). While it cannot be determined which air inclusions are due to brine drainage after the floe was removed from the ocean, the macro air inclusions in the upper

regions of the ice above ~25cm are more likely formed due to brine drainage above the freeboard. B1 and B3 show regions of lower air porosities with a small numbers of macro air inclusions present in the lower regions except for the very bottom section (Figure G.2 and Figure G.4). The average air porosity of core of core B2 and B3 was within the 95% confidence interval of each other (Table 5.4). However, the B1 average air porosity for the core was below the confidence interval of the B2 core with only a 0.06% overlap between these confidence intervals. This suggests the average air porosity, and to some extent the visual profile of the air porosities, differ with spatial variability of cores collected in a single pancake floe.

Table 5.4: Average brine and air porosities of cores from a single pancake flow collected during winter 2022

Core	Average brine porosity (%)	95% Brine porosity confidence interval	Average air porosity (%)	95% Air porosity confidence interval
B1	2.63	0.58	3.86	1.33
B2	2.30	0.67	7.14	2.01
B3	2.40	0.66	5.82	3.91

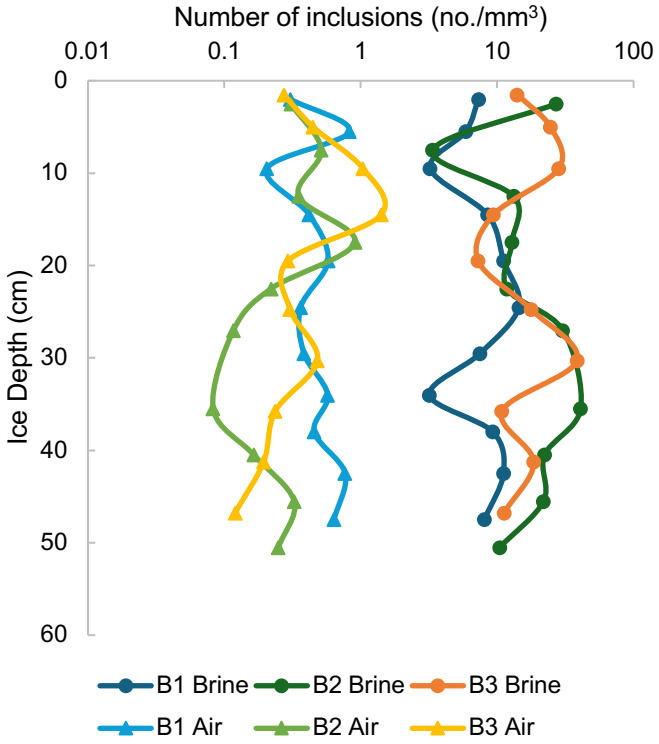


Figure 5.21: Inclusion number density profiles of brine and air of ice cores from the winter 2022 at varying locations within a pancake floe

The average brine porosities of each core were within a 95% confidence interval of each other. The profile shapes of the brine porosities varied slightly (Figure 5.20) where the B3 core showed the greatest variation through the depth of the profile. The B2 core showed the most

consistent profile with more variation in the brine porosity near the ice-ocean interface. The B2 brine porosity profile showed the least variation with depth which may be linked to the air porosity profile. Except for the very top section in the B3 core, the B3 air porosity profile showed smaller fluctuation with depth but the most variation in brine volume. The brine porosity profiles do not show a definitive trend with depth, suggesting unlike the air porosity, brine porosity profiles do not show definitive spatial variability within a pancake floe.

Table 5.5: Average brine and air number densities through the depth of cores from winter 2022

Core	Average Brine Number Density (no./mm^3)	95% Brine Number Density confidence interval	Average Air Number Density (no./mm^3)	95% Air Number Density confidence interval
B1	8.15	1.99	0.50	0.11
B2	19.41	6.95	0.32	0.15
B3	18.05	6.11	0.48	0.26

Figure 5.21 shows that the inclusion density profiles with brine number densities is significantly higher than the air number densities throughout all cores (B1, B2 and B3). B1 shows the lowest average brine number density and the highest air number density (Table 5.5). This may be influenced by the location of the B1, which is the furthest from the edge of the pancake floe. The average number of brine inclusions is more similar to the range observed for ice where thermodynamic drivers are dominant, with CT scan resolutions and scanning temperatures similar to this study (Salomon, Maus & Petrich, 2021). The B2 and B3 cores showed significantly higher brine number densities which may be influenced by the coring location on the pancake floe as being closer to the pancake edge. There is no consistent profile shape of the brine number densities across the three cores.

The average air number densities for each core show overlapping confidence intervals across the three cores. B2, which had a generally higher air porosity profile compared to B1 and B3 (Figure 5.20) have a lower air number densities between ~20-40cm depths, with relatively higher air volumes. This illustrates fewer air inclusions within this region but these are larger in size, as evident by the presence of the macro air inclusions (Figure G.3). B1 and B3 core have higher air number densities within this region, with smaller portions of macro air inclusions (Figure G.2 and Figure G.4).

The spatial variability of the cores shows relatively small differences with regards to properties of the air and brine porosities. It is recommended for that CT, textural and temperature cores be collected in-line with each other from the edge to the centre of pancake floes in order to get a linear coring profile. This will allow for investigations into the spatial development of the

porosity profiles within single pancake floes and provide further understanding into the spatial variability of brine and air properties in single pancake floes. This can provide further understanding of the microscale properties of brine and air inclusions on larger scale properties and systems.

6 Overall Discussion

Sea ice samples are typically subjected to low temperature storage conditions prior to analysis, the effects of which have historically been considered negligible. However, this study shows significant reductions in the brine porosities after low temperature storages due to salt expulsion attributed to the different densities between ice and liquid water. Lower brine porosities are observed in samples that experience low temperature storage compared to samples that are maintained at higher temperatures. Air porosities however do not show significant changes through low temperature cycles, although the winter 2022 samples maintained in higher temperature conditions have higher air volumes. This could be attributed the atmospheric temperatures near the melting point of sea ice during winter 2022 sample collection or the higher potential for brine drainage of samples maintained at higher storage temperatures. There is no statistically significant difference between the UD and MD heating methods on the brine or air inclusions within sea ice samples.

The number of brine inclusions increases after low temperature storage, while air number densities have shown a decrease in upper regions of the ice while there is an increase in the lower regions of the ice, all of which are not statistically significant. There is a statistically significant difference in the average horizontal dimensions but not the vertical dimensions of brine inclusions, which corresponds to a decreasing sphericity of brine inclusions for cuboid-shaped ice segments that experience low temperature cycles. The reduction in only the horizontal dimensions can be attributed to the size of the samples with a greater vertical length than width. Air inclusions by comparison do not show a change in sphericity through low temperature thermal cycles. The extent of the changing sphericity may be attributed to the shape of the ice samples analysed and the storage period.

The properties of brine and air inclusions show slight variations between cores collected from varying locations within a single pancake floe. The differences are mainly attributed to the air porosities and number of brine inclusions. The differences may be due to the ridging behaviour of pancake ice due to the turbulent conditions in the Antarctic MIZ, thus the impact of pancake floes bumping against one another will have greater effect towards the edges of the pancake. Therefore, the locations of cores may be important.

This study shows that the sampling protocols for pancake ice influences the microstructural properties and therefore the most accurate representation of these properties would be *in situ* analysis. In the absence of this due to logistical considerations, the impact of these sampling

protocols need to be understood. It is evident that temperature greatly influences the brine inclusions within sea ice samples, therefore, changes would have occurred from the *in situ* conditions to storage conditions even if samples are maintained in higher temperature conditions of -10°C prior to analysis. In the absence of methods that maintain the thermal gradient of ice cores, sea ice samples should be maintained at temperatures closer to *in situ* temperatures rather than lower temperature storage prior to CT analysis and samples should be analysed as soon as possible in order to reduce the microstructural changes from *in situ* conditions.

7 Conclusions and Recommendations

7.1 Conclusions

With the aim of investigating the effects of sample collection methods and storage conditions on sea ice porosity using CT analysis, the following conclusions were reached:

- Optimisation of sample protocols during the winter 2022 expedition was successfully conducted. Sea ice samples were maintained in higher temperatures conditions that are the same as the CT scan analysis temperatures (-10°C), thereby mitigating the effects of low temperature storage (-18°C) and heating methods on the brine and air inclusions in sea ice.
- Localised thresholding computational algorithms with visual inspection for the removal of scan artifacts are best suited for CT analysis of sea ice with volumes, diameters, projected dimensions, sphericities and number of inclusions encompassing the 3D nature of the brine and inclusions.
- Python code was utilised as a data engineering tool for the optimisation of the analysis of CT scan data. This was conducted for the selection of the relevant properties that include volumes, diameters, sphericities, projected dimensions and number of inclusions within sea ice to be analysed. Furthermore, the selection of parameters for defining the subcategories of brine and air inclusions were proposed. This incorporates the 3D nature and properties of these inclusions with respect to granular-textured ice. Additional properties such as salinity and density could then be compared to CT-based predictions. These comparisons revealed an average 37% and 6% difference between measured and CT-based predictions of the salinity and density, respectively.
- Low temperature storage significantly affects the microstructure of sea ice. Brine porosity of sea ice samples showed an average reduction of 41% after low temperature storage of -18°C in CT samples with dimensions of 2x2x5 cm. The number of brine inclusions increases after low temperature storage and the sphericity of the brine inclusions decreases which coincide with only a significant reduction in the horizontal dimensions. Air porosity is not significantly impacted by low temperature cycles with slight increases the air number densities in the upper supersaturated regions of the ice while slight decreases are observed in the lower subsaturated regions of the ice. The effects of UD and MD heating showed no differences between the heating methods.
- A comparison of the winter 2022 samples, that were maintained at -10°C prior to CT analysis, to the winter 2019 samples, that were stored in -18°C prior to CT analysis, showed significant differences in the brine and air porosities. The results show

similarities to the sea ice samples analysed before and after low temperature cycles. The environmental conditions may have attributed to some disparities, however, the results elude to more complex dynamics particularly within the brine inclusions of sea ice samples.

- The properties of brine and air inclusions show a slight dependency on the location of cores within a pancake floe. The brine number densities and air porosities showed the greatest variation with spatial variability of core, however the extent of the differences could not be thoroughly determined due the cores being of similar distances from the edge of the pancake.

7.2 Recommendations

The following recommendations are proposed for future work on the impact of collection and storage protocols on inclusions within sea ice to distinguish the influences of environmental and storage conditions:

- Optimise the method for measuring the bulk density of sea ice samples for more accurate comparison to CT-based quantities.
- Measure the salinity of sample used in CT analysis for a more accurate comparison of salinity to CT-based quantities.
- Investigate the impact of storage periods to provide insight into the effects of long term storage on the brine and air inclusions.
- Investigate the impact of UD and MD cooling and heat in a non-sequential manner.
- Investigate the impact of initial brine volume and samples size on the extent of brine volume reduction.
- Investigate the impact of gas saturation factor on air number densities through low temperature thermal cycles.
- Investigate the spatial variability of brine and air of cores collected in a linear profile from the edge to the centre within a single pancake floe.
- Investigate the impacts of storage on columnar-textured sea ice sampling.

The results of these recommended studies, should these come to pass, in conjunction with this dissertation could aid in identifying the chemical and physical drivers of these changes. With such knowledge, the handling procedures for sea ice cores can be better specified and ultimately aid in improving these measurements and more accurately determine the properties of sea ice as it is *in situ*.

8 References

Allison, I. 1997. Physical processes determining the Antarctic sea ice environment. *Australian Journal of Physics*. 50(4):759–771.

Allison, I. & Worby, A. 1994. Seasonal changes of sea-ice characteristics off East Antarctica. *Annals of Glaciology*. 20:195–201.

Anderson, D.L. & Weeks, W.F. 1958. A theoretical analysis of sea-ice strength. *Eos, Transactions American Geophysical Union*. 39(4):632–640.

Assur, A. 1960. *Composition of Sea Ice and its Tensile Strength*. Wilmette, Illinois.

Audh, R.R., Fawcett, S.E., Johnson, S., Rampai, T. & Vichi, M. (in press). Rafting of Growing Antarctic Sea Ice Enhances In-Ice Biogeochemical Activity in Winter. *Journal of Geophysical Research: Oceans*. 128(12):e2023JC019925.

Büttner, J. 2011. Permeability of young sea ice from microtomographic images. University in Bergen. Available: https://bora.uib.no/bora-xmlui/handle/1956/5633.

Cox, G.F.N. & Weeks, W.F. 1983. Equations for Determining the Gas and Brine Volumes in Sea-Ice Samples. *Journal of Glaciology*. 29(102):306–316. Available: https://www.cambridge.org/core.

Cox, G.F.N. & Weeks, W.F. 1986. Changes in the salinity and porosity of sea-ice samples during shipping and storage. *Journal of Glaciology*. 32(112):371–375. DOI: 10.3189/S0022143000012065.

Cox, G.F.N. & Weeks, W.F. 1988. Numerical simulations of the profile properties of undeformed first-year sea ice during the growth season. *Journal of Geophysical Research: Oceans*. 93(C10):12449–12460.

Crabeck, O., Delille, B., Rysgaard, S., Thomas, D.N., Geilfus, N.X., Else, B. & Tison, J.L. 2014. First “in situ”’ determination of gas transport coefficients (DO2, DAr, and DN2) from bulk gas concentration measurements (O2, N2, Ar) in natural sea ice”. *Journal of Geophysical Research: Oceans*. 119(10):6655–6668. DOI: 10.1002/2014JC009849.

Crabeck, O., Galley, R., Delille, B., Else, B., Geilfus, N.X., Lemes, M., Roches, M. Des, Francus, P., et al. 2016. Imaging air volume fraction in sea ice using non-destructive X-ray tomography. *Cryosphere*. 10(3):1125–1145. DOI: 10.5194/tc-10-1125-2016.

Delille, B., Vancoppenolle, M., Geilfus, N., Tilbrook, B., Lannuzel, D., Schoemann, V., Becquevort, S., Carnat, G., et al. 2014. Southern Ocean CO2 sink: The contribution of the sea ice. *Journal of Geophysical Research: Oceans*. 119(9):6340–6355.

Eayrs, C., Holland, D., Francis, D., Wagner, T., Kumar, R. & Li, X. 2019. Understanding the Seasonal Cycle of Antarctic Sea Ice Extent in the Context of Longer-Term Variability. *Reviews of Geophysics*. 57(3):1037–1064. DOI: 10.1029/2018RG000631.

Eicken, H. 1993. Automated image analysis of ice thin sections—instrumentation, methods and extraction of stereological and textural parameters. *Journal of Glaciology*. 39(132):341–352.

Eicken, H. 2003. From the microscopic, to the macroscopic, to the regional scale: growth, microstructure and properties of sea ice. In *Sea ice: an introduction to its physics, chemistry, biology and geology*. Wiley Online Library. 22–81.

Eicken, H. & Lange, M.A. 1989. Development and properties of sea ice in the coastal regime of the southeastern Weddell Sea. *Journal of Geophysical Research: Oceans*. 94(C6):8193–8206. DOI: 10.1029/JC094IC06P08193.

Eicken, H., Reimnitz, E., Alexandrov, V., Martin, ~ T, Kassens, H. & Viehoff, T. 1997. Sea-ice processes in the Laptev Sea and their importance for sediment export. *Continental Shelf Research*. 17(2):205–233.

Eicken, H., Bock, C., Wittig, R., Miller, H. & Poertner, H.-O. 2000. Magnetic resonance imaging of sea-ice pore fluids: methods and thermal evolution of pore microstructure. *Cold Regions Science and Technology*. 31:207–225. Available: www.elsevier.comrlocatercoldregions.

European Space Agency. 2016. Available: https://earth.esa.int/eogateway/documents/20142/1227611/Introduction-sea-ice-Process-Observations-and-Model.pdf [2023, October 17].

Feltham, D.L., Untersteiner, N., Wettlaufer, J.S. & Worster, M.G. 2006. Sea ice is a mushy layer. *Geophysical Research Letters*. 33(14). DOI: 10.1029/2006GL026290.

Flores, A.A. & Goff, H.D. 1999. Recrystallization in Ice Cream After Constant and Cycling Temperature Storage Conditions as Affected by Stabilizers. *Journal of Dairy Science*. 82(7):1408–1415. DOI: https://doi.org/10.3168/jds.S0022-0302(99)75367-1.

Frankenstein, G. & Garner, R. 1967. Equations for determining the brine volume of sea ice from − 0.5° to −22.9°C. *Journal of Glaciology*. 6(48):943–944. Available: https://www.cambridge.org/core.

Frantz, C.M., Light, B., Farley, S.M., Carpenter, S., Lieblappen, R., Courville, Z., Orellana, M. V. & Junge, K. 2019. Physical and optical characteristics of heavily melted “rotten” Arctic sea ice. *Cryosphere*. 13(3):775–793. DOI: 10.5194/TC-13-775-2019.

Freitag, J. 1999. Untersuchungen zur Hydrologie des arktischen Meereises-Konsequenzen für den kleinskaligen Stofftransport. The hydraulic properties of Arctic Sea-Ice-Implications for the small scale particle transport. *Ber. Polarforsch*. 325.

Galley, R.J., Else, B.G.T., Geilfus, N.-X., Hare, A.A., Isleifson, D., Barber, D.G. & Rysgaard, S. 2015. Imaged brine inclusions in young sea ice—Shape, distribution andformation timing. *Cold Regions Science and Technology*. 111:39–48. DOI: http://dx.doi.org/10.1016/j.coldregions.2014.12.011.

Golden, K.M., Ackley, S.F. & Lytle, V.I. 1998. The percolation phase transition in sea ice. *Science*. 282(5397):2238–2241.

Golden, K.M., Eicken, H., Heaton, A.L., Miner, J., Pringle, D.J. & Zhu, J. 2007. Thermal evolution of permeability and microstructure in sea ice. *Geophysical Research Letters*. 34(16). DOI: 10.1029/2007GL030447.

Gonzalez, R. 2015. *Getting started with thresholding*. Available: https://campus.datacamp.com/courses/image-processing-in-python/introducing-image-processing-and-scikit-image?ex=7 [2022, March 04].

Gosink, T.A., Pearson, J.G. & Kelley, J.J. 1976. Gas movement through sea ice. *Nature*. 263(5572):41–42.

Gow, A.J., Ackley, S.F., Weeks, W.F. & Govoni, J.W. 1982. Physical and structural characteristics of Antarctic sea ice. *Annals of Glaciology*. 3:113–117.

Grenfell, T.C. 1983. A theoretical model of the optical properties of sea ice in the visible and near infrared. *Journal of Geophysical Research*. 88(C14):9723–9735. DOI: 10.1029/JC088IC14P09723.

Haas, C. 2003. Dynamics versus thermodynamics: The sea ice thickness distribution. In *Sea ice: An introduction to its physics, chemistry, biology and geology*. Wiley Online Library. 82–111.

Hambrock, M. 2021. Exploring the effects of single and dual phase culturing on the concentrations of Southern Ocean sea-ice algae and transporting living sea-ice algae from the Southern Ocean to land-based research facilities. Master's Dissertation. University of Cape Town.

Hobbs, P. V. 2010. *Ice Physics*. Oxford university press.

Hobbs, W.R., Bindoff, N.L. & Raphael, M.N. 2015. New perspectives on observed and simulated Antarctic sea ice extent trends using optimal fingerprinting techniques. *Journal of Climate*. 28(4):1543–1560.

Islam, M.R. 2018. Sample size and its role in Central Limit Theorem (CLT). *Computational and Applied Mathematics Journal*. 4(1):1–7.

Johnson, S. 2020. Evaluation of the Changes in the Crystal Structure of Antarctic Sea Ice from the Marginal Ice Zone during Winter and Spring. Masters Dissertation. University of Cape Town.

Johnson, S., Audh, R.R., Jager, W. de, Matlakala, B., Vichi, M., Womack, A. & Rampai, T. 2023. Physical and morphological properties of first-year Antarctic sea ice in the spring marginal ice zone of the Atlantic-Indian sector. *Journal of Glaciology*. (April, 17):1–14. DOI: 10.1017/JOG.2023.21.

Kawamura, T. 1988. Observations of the Internal Structure of Sea Ice by X Ray Computed Tomography. *Journal of Geophysical Research* . 93(3):2343–2350.

Keeling, R.F. & Stephens, B.B. 2001. Antarctic sea ice and the control of Pleistocene climate instability. *Paleoceanography*. 16(1):112–131. DOI: 10.1029/2000PA000529.

Kožíšek, Z., Demo, P. & Sato, K. 2000. Nucleation on active sites: Evolution of size distribution. *Journal of crystal growth*. 209(1):198–202.

Lange, M.A. & Eicken, H. 1991. Textural characteristics of sea ice and the major mechanisms of ice growth in the Weddell Sea. *Annals of Glaciology*. 15:210–215. DOI: 10.3189/1991AoG15-1-210-215.

Lange, M.A., Ackley, S.F., Wadhams, P., Dieckmann, G.S. & Eicken, H. 1989. Development of Sea Ice in the Weddell Sea. *Annals of Glaciology*. 12:92–96. DOI: 10.3189/S0260305500007023.

Lange, M.A., Schlosser, P., Ackley, S.F., Wadhams, P. & Dieckmann, G.S. 1990. 18O concentrations in sea ice of the Weddell Sea, Antarctica. *Journal of Glaciology*. 36(124):315–323.

Lecomte, O., Goosse, H., Fichefet, T., Holland, P.R., Uotila, P., Zunz, V. & Kimura, N. 2016. Impact of surface wind biases on the Antarctic sea ice concentration budget in climate models. *Ocean Modelling*. 105:60–70.

Li, X. & Yortsosa, Y.C. 1994. Bubble Growth and Stability in an Effective Porous Medium. *Article in Physics of Fluids*. 6(5). DOI: 10.1063/1.868229.

Lieb-Lappen, R.M., Golden, E.J. & Obbard, R.W. 2017. Metrics for interpreting the microstructure of sea ice using X-raymicro-computed tomography. *Cold Regions Science and Technology*. 138:24–35.

Light, B., Maykut, G.A. & Grenfell, T.C. 2003. Effects of temperature on the microstructure of first-year Arctic sea ice. *Journal of Geophysical Research: Oceans*. 108(C2):3051. DOI: 10.1029/2001JC000887.

Lin, X. 2022. Permeability of winter and spring first-year ice in the Antarctic marginal ice zone. MSc Dissertation. University of Cape Town.

Lofgren, G. & Weeks, W.F. 1969. Effect of growth parameters on substructure spacing in NaCl ice crystals. *Journal of Glaciology*. 8(52):153–164.

Loose, B., Schlosser, P., Perovich, D., Ringelberg, D., Ho, D.T., Takahashi, T., Richter-Menge, J., Reynolds, C.M., et al. 2011. Gas diffusion through columnar laboratory sea ice: Implications for mixed-layer ventilation of CO2 in the seasonal ice zone. *Tellus, Series B: Chemical and Physical Meteorology*. 63(1):23–39. DOI: 10.1111/J.1600-0889.2010.00506.X.

Maksym, T. 2019. Arctic and Antarctic Sea ice change: contrasts, commonalities, and causes. *Annual Review of Marine Science*. 11:187–213.

Matsumura, Y. & Ohshima, K.I. 2015. Lagrangian modelling of frazil ice in the ocean. *Annals of glaciology*. 56(69):373–382.

Maus, S., Huthwelker, T., Enzmann, F., Miedaner, M., Stampanoni, M., Marone, F., Hutterli, M.A., Hintermüller, C., et al. 2009. *Synchrotron-based X-ray micro-tomography:Insights into Sea Ice Microstructure*.

Maus, S., Schneebeli, M. & Wiegmann, A. 2021. An X-ray micro-tomographic study of the pore space, permeability and percolation threshold of young sea ice. *Cryosphere*. 15(8):4047–4072. DOI: 10.5194/TC-15-4047-2021.

McPhee, M.G. 2017. The sea ice–ocean boundary layer. In *Sea ice*. Wiley Online Library. 138–159.

Middleton, C.A., Thomas, C., De Wit, A. & Tison, J.L. 2016. Visualizing brine channel development and convective processes during artificial sea-ice growth using Schlieren optical methods. *Journal of Glaciology*. 62(231):1–17. DOI: 10.1017/JOG.2015.1.

Nakawo, M. & Sinha, N.K. 1984. A note on brine layer spacing of first-year sea ice. *Atmosphere - Ocean*. 22(2):193–206. DOI: 10.1080/07055900.1984.9649193.

Nelson, K.H. & Thompson, T.G. 1954. Deposition of salts from sea water by frigid concentration.

Nomura, D., Yoshikawa-Inoue, H. & Toyota, T. 2006. The effect of sea-ice growth on air-sea CO2 flux in a tank experiment. *Tellus, Series B: Chemical and Physical Meteorology*. 58(5):418–426. DOI: 10.1111/J.1600-0889.2006.00204.X.

Notz, D. 2005. Thermodynamic and fluid-dynamical processes in sea ice. University of Cambridge.

Notz, D. & Worster, M.G. 2009. Desalination processes of sea ice revisited. *Journal of Geophysical Research: Oceans*. 114(5). DOI: 10.1029/2008JC004885.

Notz, D., Wettlaufer, J.S. & Worster, M.G. 2005. A non-destructive method for measuring the salinity and solid fraction of growing sea ice in situ. *Journal of Glaciology*. 51(172):159–166. DOI: 10.3189/172756505781829548.

Oggier, M. & Eicken, H. 2022. Seasonal evolution of granular and columnar sea ice pore microstructure and pore network connectivity. *Journal of Glaciology*. (February, 18):1–16. DOI: 10.1017/JOG.2022.1.

OpenCV. 2022. *Image Thresholding*.

OSIL. 2020. *Guideline Portasol Salinometer*. Available: https://osil.com/product/portasal-salinometer-8410a/ [2023, May 24].

Paul, F., Mielke, T., Audh, R. & Lupascu, D.C. 2022. Sea ice strength development from freezing to melting in the Antarctic marginal ice zone. In *Proceedings of the YIC 2021-VI ECCOMAS Young Investigators Conference*. Editorial Universitat Politècnica de València. 375–385.

Perovich, D.K. 2017. Sea ice and sunlight. *Sea ice*. 110–137.

Perovich, D.K. & Gow, A.J. 1996. A quantitative description of sea ice inclusions. *Journal of Geophysical Research: Oceans*. 101(C8):18327–18343. DOI: 10.1029/96JC01688.

Perovich, DK. & Grenfell, TC. 1981. Laboratory studies of the optical properties of young sea ice. *Journal of Glaciology*. 27(96):331–346. Available: https://web.archive.org/web/20180722113531id_/https://www.cambridge.org/core/services/aop-cambridge-core/content/view/E2B5AE1551429D957D0699AA00E234DF/S0022143000015410a.pdf/div-class-title-laboratory-studies-of-the-optical-properties-of-young-sea-ice-a-href-fn1-ref-type-fn-span-class-sup-span-a-div.pdf [2023, July 22].

Petrich, C. & Eicken, H. 2017. Overview of sea ice growth and properties. In *Sea Ice*. 3rd ed. 1–41.

Petrich, C., Langhorne, P.J. & Sun, Z.F. 2006. Modelling the interrelationships between permeability, effective porosity and total porosity in sea ice. *Cold Regions Science and Technology*. 44(2):131–144. DOI: 10.1016/J.COLDREGIONS.2005.10.001.

Pounder, E.R. 1965. *The Physics of Ice*. Oxford, UK: Pergamon Press.

Rasband, W.S. 2018. *ImageJ*. Available: https://imagej.nih.gov/ij/ [2023, July 06].

Ringer, W.E. 1928. *Über die Veranderingen in samenstelling van zeewater bij het bevriesen (Changes in the composition of sea water upon freezing)*.

Roedder, E. 1972. Composition of Fluid Inclusions: Reviews of World Literature. In *Data of Geochemistry*. 6th ed. M. Fleischer, Ed. Washington: United States Government Printing Office. Available: https://books.google.co.za/books?hl=en&lr=&id=SCMlAQAAIAAJ&oi=fnd&pg=PA1&dq=related:tJQTtWL757AJ:scholar.google.com/&ots=luTiqYH3X3&sig=3m26cFuRakK3i6y23BU4Esmo6L4#v=onepage&q=ice&f=false [2023, August 02].

Ryan-Keogh, T. & Vichi, M. 2022. *SCALE-WIN19 & SCALE-SPR19 Cruise Report*. DOI: 10.5281/ZENODO.5906324.

Salomon, M.L., Maus, S. & Petrich, C. 2021. Microstructure evolution of young sea ice from a Svalbard fjord using micro-CT analysis. *Journal of Glaciology*. 1–20. DOI: 10.1017/JOG.2021.119.

Sandven, S. & Johannessen, O.M. 2006. Sea ice monitoring by remote sensing. The American Society for Photogrammetry & Remote Sensing.

Scott, M. & Hansen, K. 2016. *Sea Ice*. Available: https://earthobservatory.nasa.gov/features/SeaIce [2024, May 01].

Semiletov, I., Makshtas, A., Akasofu, S.I. & Andreas, E.L. 2004. Atmospheric CO2 balance: The role of Arctic sea ice. *Geophysical Research Letters*. 31(5). DOI: 10.1029/2003GL017996.

Skatulla, S., Audh, R.R., Cook, A., Hepworth, E., Johnson, S., Lupascu, D.C., MacHutchon, K., Marquart, R., et al. 2022. Physical and mechanical properties of winter first-year ice in the Antarctic marginal ice zone along the Good Hope Line. *The Cryosphere*. 16(7):2899–2925. Available: https://tc.copernicus.org/articles/16/2899/2022/tc-16-2899-2022.pdf [2023, May 24].

Smedsrud, L.H. & Skogseth, R. 2006. Field measurements of Arctic grease ice properties and processes. *Cold regions science and technology*. 44(3):171–183.

Sutton, R.L., Lips, A. & Piccirillo, G. 1996. Recrystallization in aqueous fructose solutions as affected by locust bean gum. *Journal of food science*. 61(4):746–748.

Thomas, D.N., ed. 2017. *Sea Ice*. Third ed. John Wiley & Sons.

Tison, J.-L., Haas, C., Gowing, M.M., Sleewaegen, S. & Bernard, A. 2002. Tank study of physico-chemical controls on gas content and composition during growth of young sea ice. *Journal of Glaciology*. 48(161):177–191.

Tsurikov, V.L. 1979. The Formation and Composition of the Gas Content of Sea Ice. *Journal of Glaciology*. 22(86):67–81.

Untersteiner, N. 1961. On the mass and heat budget of Arctic sea ice. *Archiv für Meteorologie, Geophysik und Bioklimatologie, Serie A*. 12:151–182.

Vancoppenolle, M., Meiners, K.M., Michel, C., Bopp, L., Brabant, F., Carnat, G., Delille, B., Lannuzel, D., et al. 2013. Role of sea ice in global biogeochemical cycles: Emerging views and challenges. *Quaternary science reviews*. 79:207–230.

Vichi, M. 2023. *SCALE-WIN22 Cruise Report*. DOI: 10.5281/ZENODO.7902557.

Vichi, M., Eayrs, C., Alberello, A., Bekker, A., Bennetts, L., Holland, D., de Jong, E., Joubert, W., et al. 2019. Effects of an Explosive Polar Cyclone Crossing the Antarctic Marginal Ice Zone. *Geophysical Research Letters*. 46(11):5948–5958. DOI: 10.1029/2019GL082457.

Wadhams, P., Lange, M.A. & Ackley, S.F. 1987. The ice thickness distribution across the Atlantic sector of the Antarctic Ocean in midwinter. *Journal of Geophysical Research*. 92(C13):535–549.

Weeks, W. 2010. *On Sea Ice*. University of Alaska Press.

Weeks, W.F. & Ackley, S.F. 1982. *The growth, structure, and properties of sea ice*.

Weeks, W.F. & Assur, A. 1967. *The Mechanical Properties of Sea Ice* . 2nd ed. Hanover, New Hampshire: Cold Regions Science and Engineering Part II: Physical Science Section C: Physics and Mechanics of Ice.

Weeks, W.F. & Hamilton, W.L. 1962. Petrographic characteristics of young sea ice, Point Barrow, Alaska. *American Mineralogist: Journal of Earth and Planetary Materials*. 47(7–8):945–961.

Worster, M.G. 1992. The Dynamics of Mushy Layers. *Interactive Dynamics of Convection and Solidification*. 113–138. DOI: 10.1007/978-94-011-2809-4_20.

Worster, M.G. & Wettlaufer, J.S. 1997. Natural convection, solute trapping, and channel formation during solidification of saltwater. *The Journal of Physical Chemistry B*. 101(32):6132–6136.

Zhou, J., Delille, B., Eicken, H., Vancoppenolle, M., Brabant, F., Carnat, G., Geilfus, N.X., Papakyriakou, T., et al. 2013. Physical and biogeochemical properties in landfast sea ice (Barrow, Alaska): Insights on brine and gas dynamics across seasons. *Journal of Geophysical Research: Oceans*. 118(6):3172–3189. DOI: 10.1002/JGRC.20232.

Zicus, S. 2017. *Development of sea ice – Australian Antarctic Program*. Available: https://www.antarctica.gov.au/about-antarctica/ice-and-atmosphere/sea-ice/development-of-sea-ice/ [2022, June 26].

Appendix A: Ethics Clearance

Application for Approval of Ethics in Research (EiR) Projects
Faculty of Engineering and the Built Environment, University of Cape Town

ETHICS APPLICATION FORM

Please Note:
Any person planning to undertake research in the Faculty of Engineering and the Built Environment (EBE) at the University of Cape Town is required to complete this form **before** collecting or analysing data. The objective of submitting this application *prior* to embarking on research is to ensure that the highest ethical standards in research, conducted under the auspices of the EBE Faculty, are met. Please ensure that you have read, and understood the **EBE Ethics in Research Handbook** (available from the UCT EBE, Research Ethics website) prior to completing this application form: http://www.ebe.uct.ac.za/ebe/research/ethics1

APPLICANT'S DETAILS		
Name of principal researcher, student or external applicant		Hayley Swait
Department		Chemical Engineering
Preferred email address of applicant:		swthay001@myuct.ca.za
If Student	Your Degree: e.g., MSc, PhD, etc.	Msc in Chemical Engineering
	Credit Value of Research: e.g., 60/120/180/360 etc.	180
	Name of Supervisor (if supervised):	Dr Tokoloho Rampai
If this is a researchcontract, indicate the source of funding/sponsorship		
Project Title		Investigating the air and brine porosity of Antarctic sea ice

I hereby undertake to carry out my research in such a way that:

- there is no apparent legal objection to the nature or the method of research; and
- the research will not compromise staff or students or the other responsibilities of the University;
- the stated objective will be achieved, and the findings will have a high degree of validity;
- limitations and alternative interpretations will be considered;
- the findings could be subject to peer review and publicly available; and
- I will comply with the conventions of copyright and avoid any practice that would constitute plagiarism.

APPLICATION BY	Full name	Signature	Date
Principal Researcher/ Student/External applicant	Hayley Swait	Swait	04/02/2022
SUPPORTED BY	Full name	Signature	Date
Supervisor (where applicable)	Dr Tokoloho Rampai		17/02

APPROVED BY	Full name	Signature	Date
HOD (or delegated nominee) Final authority for all applicants who have answered NO to all questions in Section 1; and for all Undergraduate research (Including Honours).	Dr Elaine Opitz		23 Feb 2022
Chair: Faculty EIR Committee For applicants other than undergraduate students who have answered YES to any of the questions in Section 1.			

Appendix B: Physical Property Results

Table B.1: Temperature measurements from the winter 2019 pancake

19 WMIZ 1 Coring Date: 28/07/2019 (Skatulla et al., 2022)					
Core A3		**Core A4**		**Core A5**	
Core Length: 40 cm		**Core Length: 35 cm**		**Core Length: 29.5 cm**	
Ice Depth (cm)	**Temperature (°C)**	**Ice Depth (cm)**	**Temperature (°C)**	**Ice Depth (cm)**	**Temperature (°C)**
2.5	-6.82	2.5	-6.71	2.5	-5.61
5	-6.00	5	-6.33	5	-5.12
10	-5.57	10	-5.72	10	-4.78
15	-4.81	15	-5.30	15	-4.30
20	-4.24	20	-4.90	20	-3.66
25	-3.66	25	-4.40	25	-3.41
30	-3.28	30	-4.04	27.5	-3.34
35	-2.90	32.5	-3.80		
37.5	-2.43				

Table B.2: Temperature measurements from the winter 2022 pancake

22 WMIZ 3 Coring Date: 24/07/2022					
Core B6 Core Length: 55 cm		**Core B7 Core Length: 65 cm**		**Core B8 Core Length: 62.5 cm**	
Ice Depth (cm)	**Temperature (°C)**	**Ice Depth (cm)**	**Temperature (°C)**	**Ice Depth (cm)**	**Temperature (°C)**
5	-1.92	5	-2.1	2.5	-1.89
10	-2.12	10	-2.48	7.5	-1.94
15	-2.51	15	-2.81	12.5	-2.01
20	-2.72	20	-2.89	17.5	-2.22
25	-2.78	25	-2.95	22.5	-2.51
30	-2.67	30	-2.97	27.5	-2.6
35	-2.52	35	-2.82	32.5	-2.85
40	-2.2	40	-2.71	37.5	-2.91
45	-1.88	45	-2.47	42.5	-2.98
50	-1.71	50	-2.24	47.5	-3.02
52.5	-1.39	55	-2.12	52.5	-2.86
		60	-2.04	57.5	-2.72
		62.5	-1.8	60	-2.48

Table B.3: Salinity measurements from the winter 2019 pancake

19 WMIZ 1 Coring Date: 28/07/2019					
Core A3		**Core A4**		**Core A5**	
Core Length: 40 cm		**Core Length: 35 cm**		**Core Length: 29.5 cm**	
Ice Depth (cm)	**Salinity (psu)**	**Ice Depth (cm)**	**Salinity (psu)**	**Ice Depth (cm)**	**Salinity (psu)**
5	19.81	4.9	20.74	4.75	12.08
15	6.37	14.8	6.94	14.5	6.98
25	6.16	27.1	6.54	23.9	5.00
35	6.64				

Table B.4: Dimension, mass and density measurements of the winter 2022 B1 core

Ice depth (cm)	**Length (cm)**	**Width (cm)**	**Height (cm)**	**Mass (g)**	**Density (kg/mm^3)**
0-4	20.74	20.82	42.03	14.87	820
4-7	21.49	21.59	33.07	12.69	827
7-12	20.77	20.99	49.14	18.11	845
12-17	21.09	21.49	49.21	18.21	817
17-22	20.07	20.68	47.36	16.2	825
22-27	20.96	21.08	49.22	18.52	852
27-32	20.78	20.91	45.48	17.2	871
32-36	21.46	21.10	32.55	12.33	837
36-40	21.17	21.06	35.17	13.27	847
40-45	21.68	21.43	48.98	18.68	821
45-50	20.61	20.24	47.25	16.57	842

Appendix C: Cross Polarisation Images

Cores used for cross polarised images were cut from the bottom up and were correspondingly labelled from one.

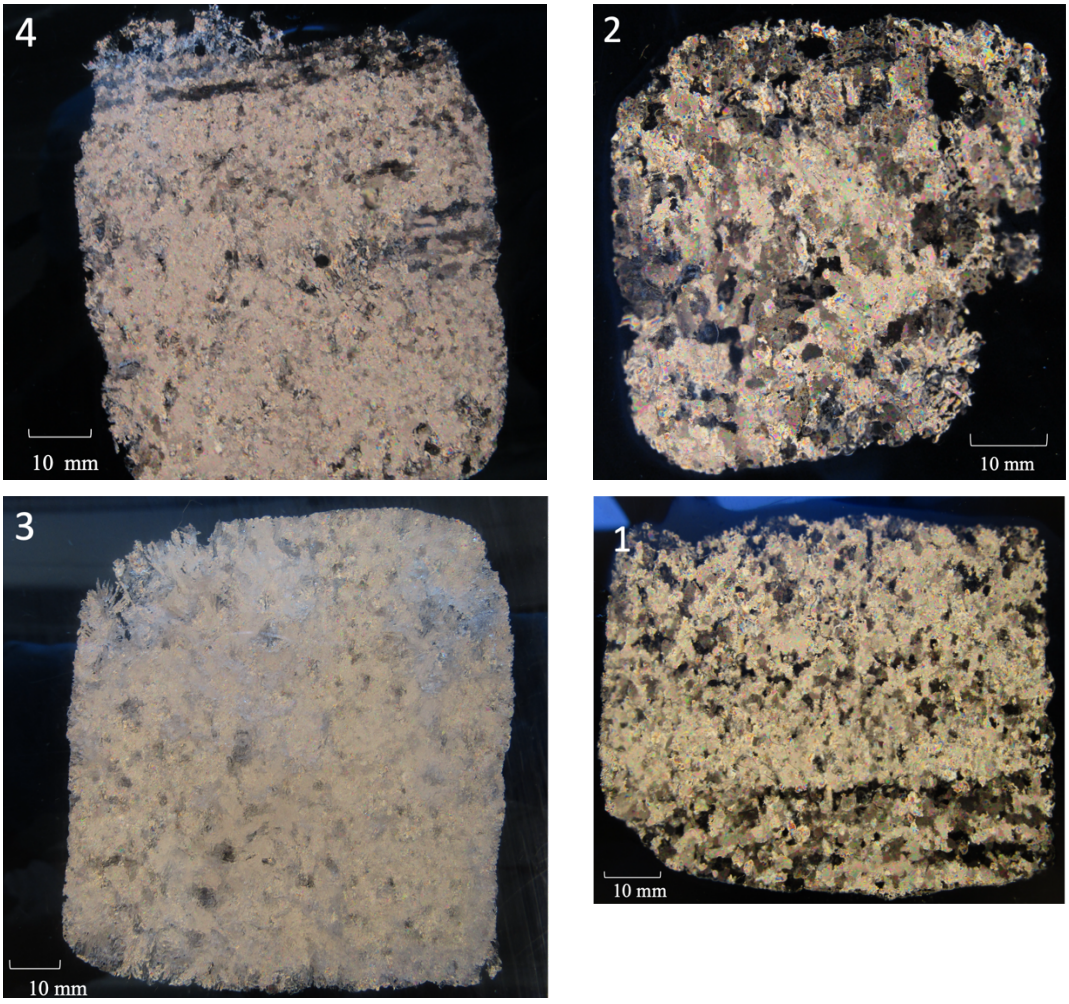


Figure C.1: Cross-polarised images from A2 core of the winter 2019 expedition, photo's ordered from 4 to 1 respectively

Table C.1: Crystal size measurements of 20 random crystals from each cross-polarised image for the winter 2019 A2 core

	Image number for cross-polarised images from the A2 core			
	4	**3**	**2**	**1**
Crystal size (mm)	1.52	2.41	3.23	2.98
	1.33	2.61	2.70	2.03
	1.33	0.96	2.34	2.29
	2.14	1.92	2.60	2.03
	1.61	2.60	1.93	2.21
	1.51	1.64	2.79	2.15
	1.31	1.86	2.28	2.30
	1.76	2.29	2.79	3.45
	1.19	1.84	3.45	2.21
	0.67	3.32	1.42	2.29
	1.15	1.95	2.16	1.92
	1.07	1.85	1.23	1.17
	1.35	3.09	1.55	1.73
	1.21	2.94	1.28	1.59
	1.54	2.27	3.20	1.29
	1.50	2.98	1.66	1.73
	1.15	2.20	2.03	2.12
	1.04	2.20	2.09	1.92
	1.46	1.88	0.85	2.19
	1.58	3.57	1.66	1.49

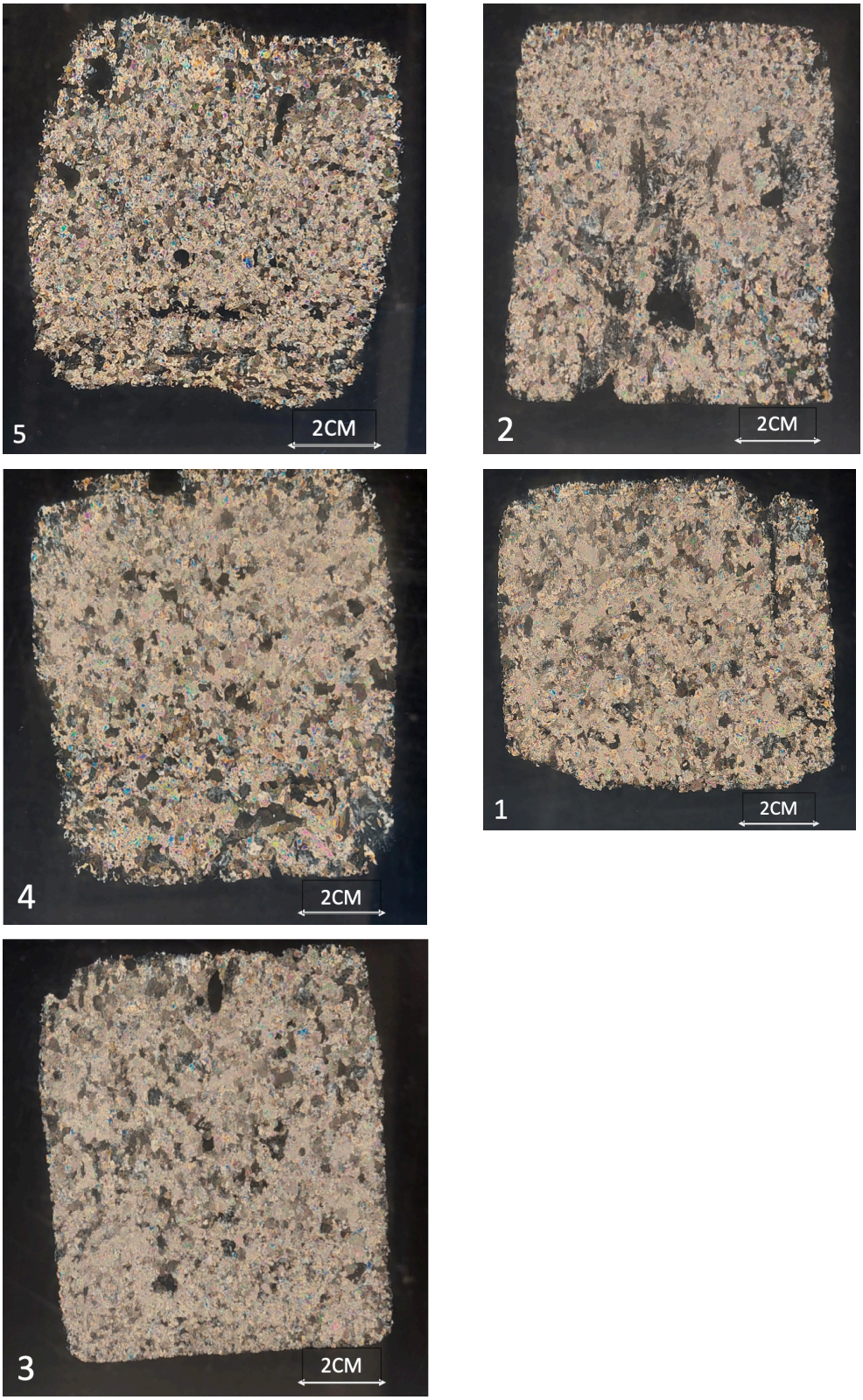


Figure C.2: Cross-polarised images from B4 core of the winter 2022 expedition, photo's ordered from 5 to 1 respectively

Table C.2: Crystal size measurements of 20 random crystals from each cross-polarised image for the winter 2022 B4 core

	Image number for cross-polarised images from the B4 core				
	5	**4**	**3**	**2**	**1**
Crystal size (mm)	1.72	2.68	1.46	1.07	3.88
	1.43	1.69	1.51	1.05	1.47
	1.17	0.98	1.32	0.69	1.9
	0.76	1.03	1.48	1.71	1.25
	1.36	2.22	2.51	1.14	1.52
	1.52	1.83	1.22	1.51	1.04
	1.24	1.29	1.8	1.82	0.8
	2.01	1.57	1.36	1.6	1.28
	1.78	1.64	2.99	1.83	2.33
	1.62	1.53	1.93	1.42	1.86
	1.6	0.9	1.47	1.26	1.1
	1.6	1.12	2.08	1.26	1.32
	1.5	1.6	1.73	1.35	2.32
	1.56	1.42	1.89	0.69	1.1
	1.22	2.65	2.36	1.05	1.79
	1.77	1.61	1.81	0.73	1.79
	0.93	1.63	2.12	2.27	1.41
	1.28	2.03	1.1	1.73	0.91
	2.38	1.85	2.75	1.87	0.91
	0.89	3.34	2.19	1.49	1.19

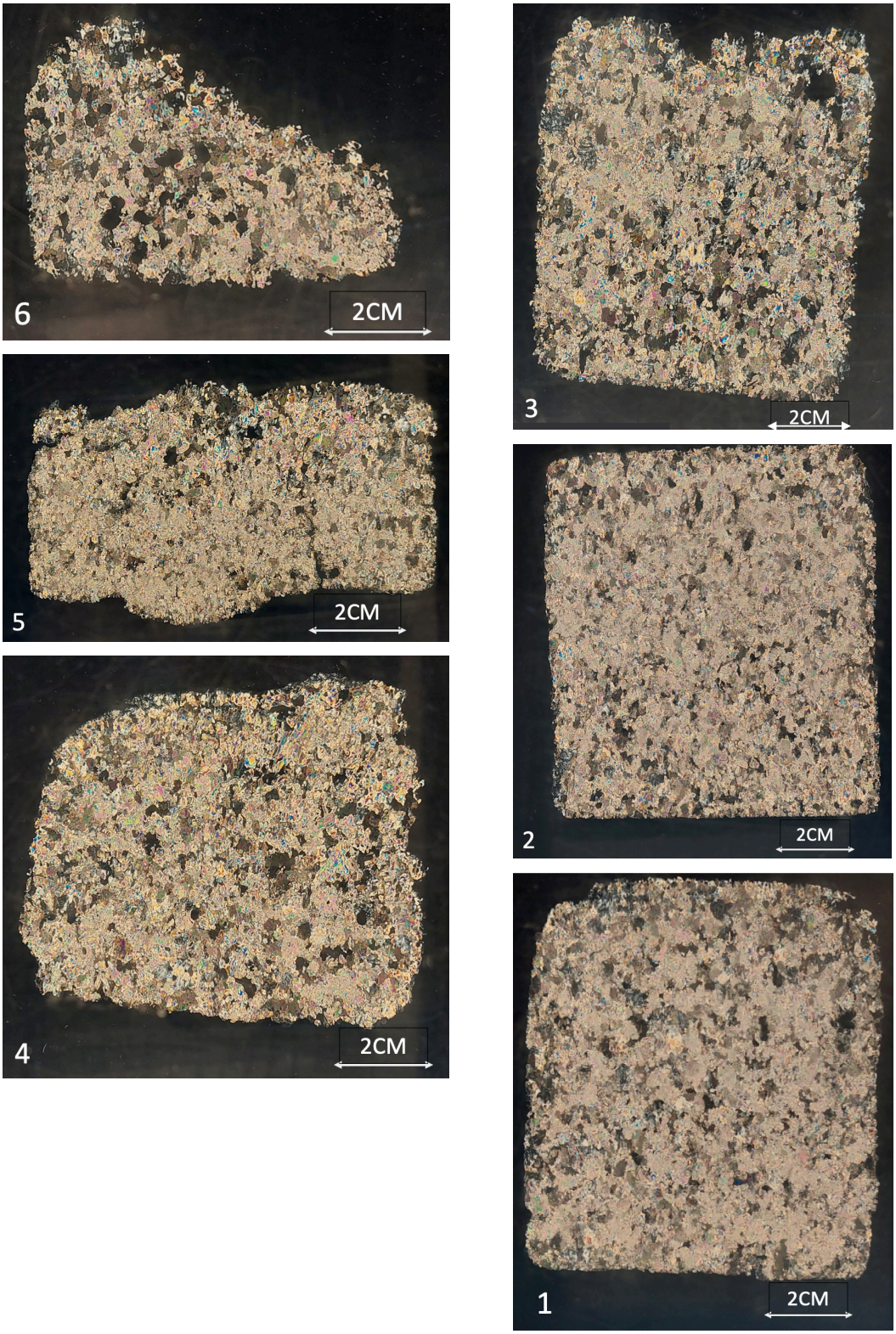


Figure C.3: Cross-polarised images from B5 core of the winter 2022 expedition, photo's ordered from 6 to 1 respectively

Table C.3: Crystal size measurements of 20 random crystals from each cross-polarised image for the winter 2022 B5 core

	Image number for cross-polarised images from the B5 core					
	6	**5**	**4**	**3**	**2**	**1**
Crystal size (mm)	2.04	1.19	2.10	4.53	2.02	2.57
	2.09	0.90	1.54	1.94	2.28	3.12
	2.15	1.25	1.26	1.86	1.36	2.90
	3.08	1.53	1.43	2.75	0.87	2.10
	2.42	1.12	1.69	3.62	1.17	2.78
	3.44	0.92	1.46	1.51	1.67	2.01
	2.98	1.36	1.71	1.78	2.13	1.31
	3.21	0.60	1.45	3.29	1.17	1.66
	2.39	1.18	1.58	1.80	1.70	1.22
	2.25	0.61	2.05	1.85	1.72	2.61
	1.19	1.37	1.77	1.55	1.41	1.69
	1.05	0.55	0.89	2.09	1.29	1.99
	1.89	1.57	1.87	1.31	1.94	2.75
	1.05	1.03	1.42	1.50	1.37	2.64
	1.53	1.72	1.47	2.29	2.29	1.94
	2.15	1.45	1.95	2.09	1.77	2.75
	1.01	1.71	1.96	3.00	2.10	2.46
	1.10	0.89	1.98	2.23	2.24	3.04
	1.49	2.86	1.07	1.27	1.70	2.59
	1.32	2.09	1.64	2.13	2.03	3.04

Appendix D: Heat Transfer Calculations for UD and MD Heating

Some basic assumptions were used to estimate the time the samples would require to heat up from -18°C to -10°C for multi- and uni-directional heating with the equations and value outlined below. The convective heat transfer coefficient, heat capacity of sea ice, mass of the samples and thermal conductivity were estimated. The area over which the heat transfer for MD heating was based on the rectangular side of the sample since they are the heat flux through those surfaces will be greater than the top and bottom of the samples (although these estimates will likely give a slightly shorter time over which the heat transfer will take place). The L was based of the half the distance between the top and bottom of the samples with the heat transfer doubled (Equation 15) to account for the transfer from both sides. Figure D.1 provided the temperature estimates of the ice over the first hour of UD and MD heating suggesting the minimum 12 hour period in which the samples were placed in -10°C environments would be sufficient for the temperature changes to occur over the various samples.

$$Q = hA(T_a - T_i) \qquad \textit{Equation 13}$$

$$Q = C_p m \frac{\partial T_i}{\partial t} \qquad \textit{Equation 14}$$

$$Q = \frac{k}{L}(T_a - T_i) \qquad \textit{Equation 15}$$

h	$15 \frac{W}{m^2.K}$
A	$MD: 0.004\ m^2$ $UD: 0.0004\ m^2$
T_a	$-10℃$
C_p	$2093 \frac{J}{kg.K}$
m	$18g$
L	$0.025\ m$
k	$1.5 \frac{W}{m.K}$

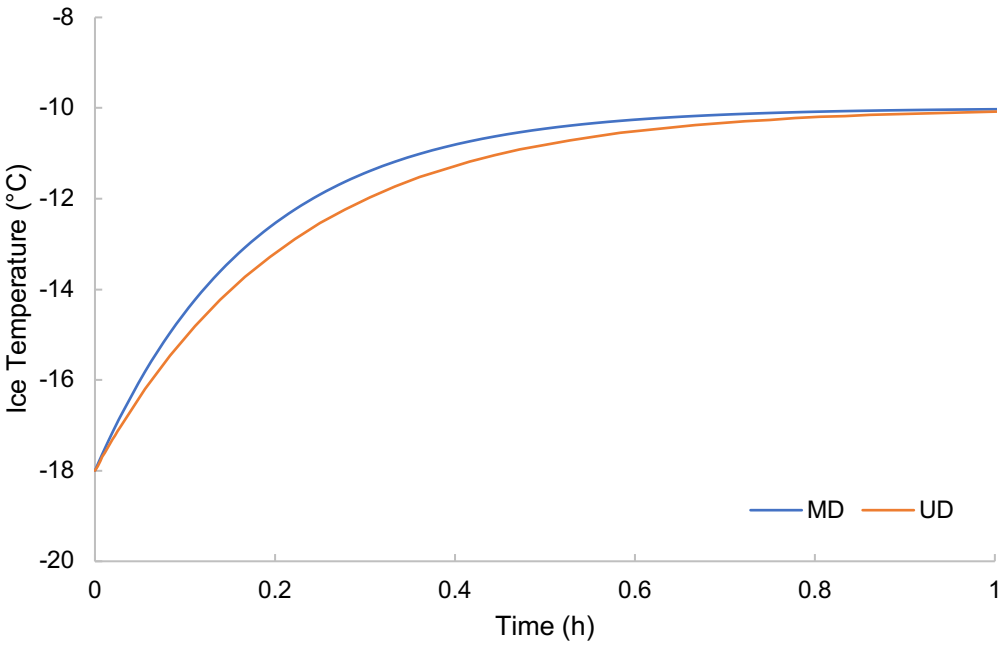


Figure D.1: Estimated temperature of the ice over the heating periods of UD and MD heating

Appendix E: UD and MD Heating Additional Results

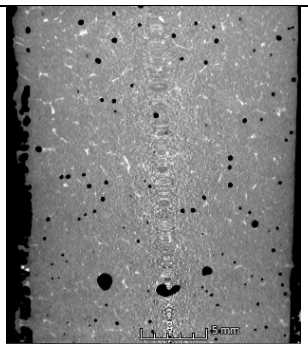
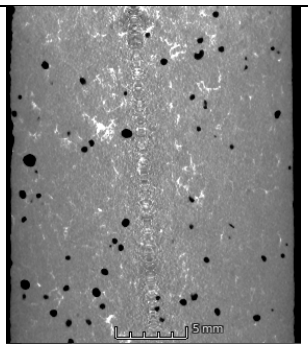
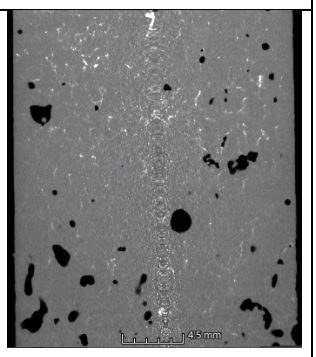
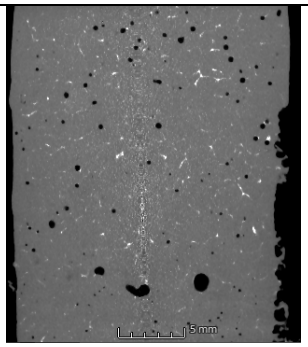
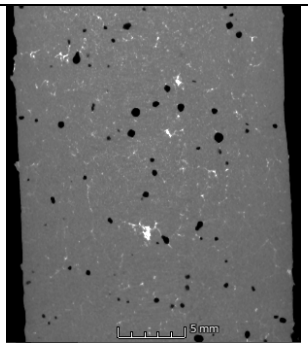
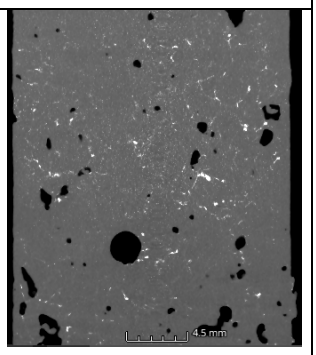
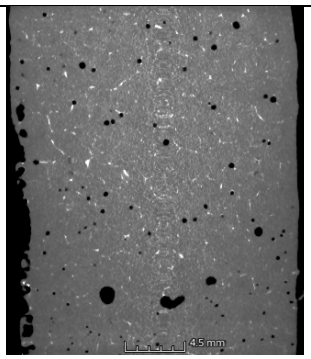
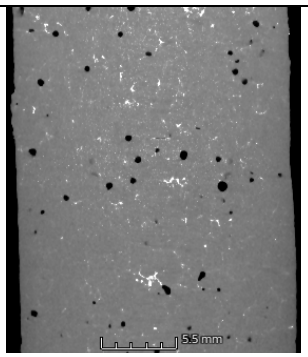
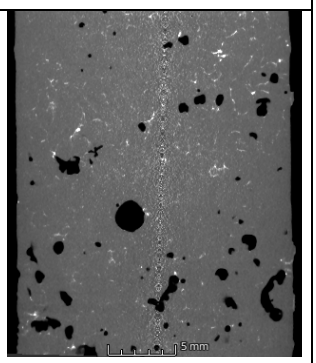
	Top	Middle	Bottom
Original			
Unidirectional heating			
Multidirectional heating			

Figure E.1: 2D Greyscale images from CT scans of the heating methods applied to ice sections

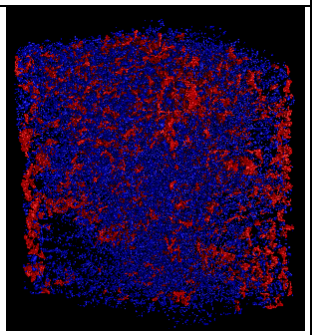
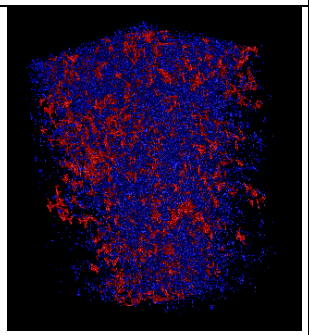
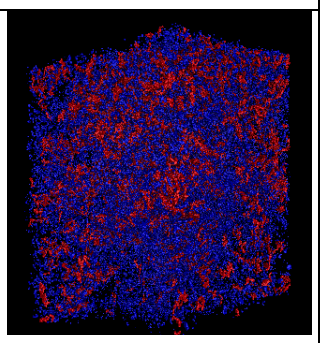
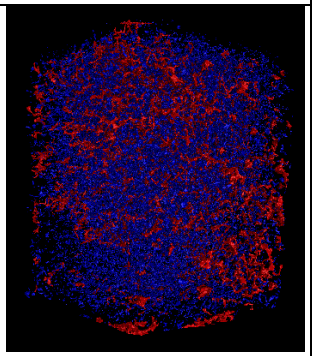
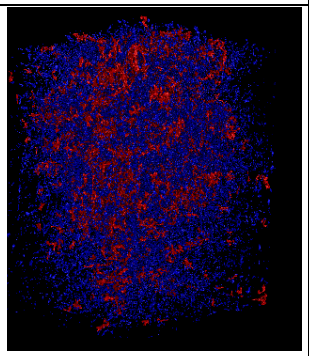
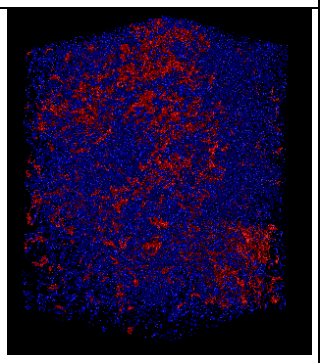
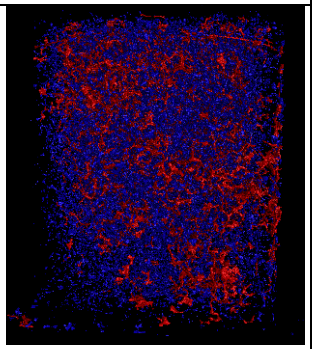
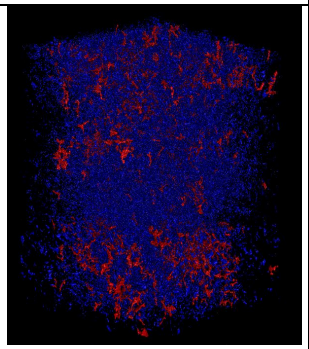
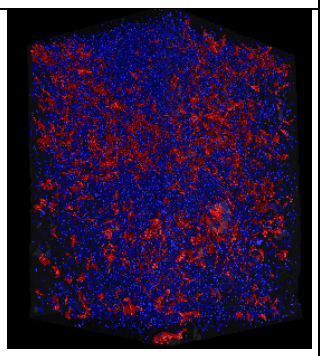
	Top	Middle	Bottom
Original			
Unidirectional heating			
Multidirectional heating			
Key:	Tubes: Pockets:		

Figure E.2: 3D reconstruction of the brine inclusions from CT scans of the heating methods applied to ice sections

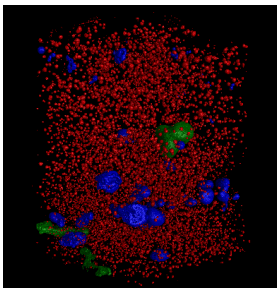
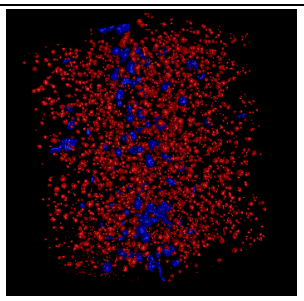
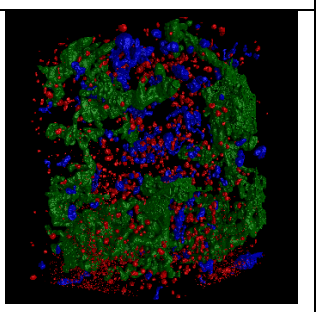
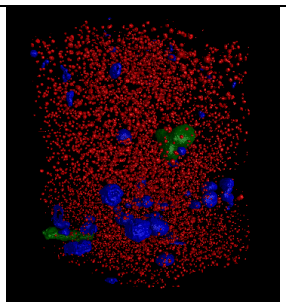
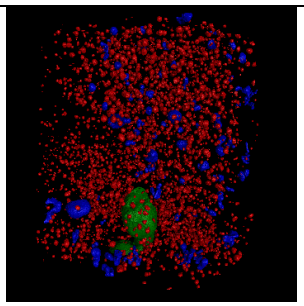
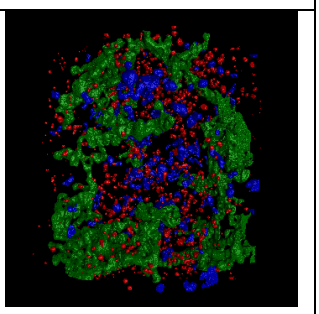
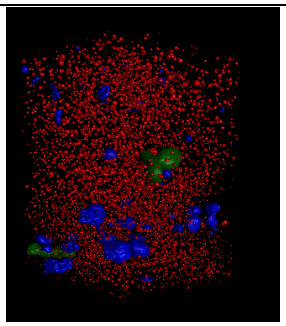
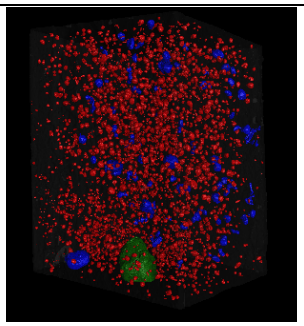
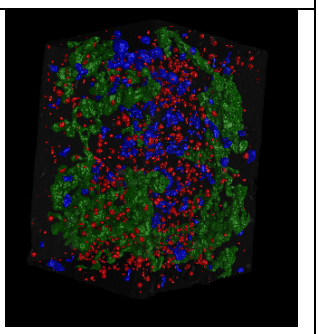
	Top	Middle	Bottom
Original			
Unidirectional heating			
Multidirectional heating			
Key:	Micro: Large: Macro:		

Figure E.3: 3D reconstruction of the air inclusions from CT scans of the heating methods applied to ice sections

Table E.1: Data generated from CT scans of the UD and MD heating study

	Brine		Air								
					Micro		Large		Macro		
Ice Sample	**Porosity (%)**	**Inclusion No. Density (no/mm³)**	**Porosity (%)**	**Inclusion No. Density (no/mm³)**	**Porosity (%)**	**Inclusion No. Density (no/mm³)**	**Porosity (%)**	**Inclusion No. Density (no/mm³)**	**Porosity (%)**	**Inclusion No. Density (no/mm³)**	**Total Porosity (%)**
Original Top	4.03	5.87	2.12	0.81	0.97	0.80	0.76	4.65E-03	0.39	2.59E-04	6.15
UD Top	2.11	7.02	1.99	0.64	0.82	0.64	0.79	5.44E-03	0.38	1.70E-04	4.10
MD Top	2.23	9.57	1.91	0.64	0.78	0.63	0.75	5.47E-03	0.38	1.76E-04	4.13
Original Middle	2.26	7.52	1.51	0.38	1.11	0.37	0.40	9.50E-03	0	0	3.77
UD Middle	1.89	8.97	2.13	0.35	1.00	0.35	0.46	8.77E-03	0.67	1.72E-04	4.02
MD Middle	1.46	13.14	1.66	0.31	0.89	0.31	0.38	7.94E-03	0.39	8.45E-05	3.12
Original Bottom	4.39	8.04	5.48	0.14	0.37	0.12	0.83	1.81E-02	4.28	3.80E-04	9.87
UD Bottom	1.79	15.24	5.02	0.15	0.40	0.13	0.81	1.80E-02	3.81	2.71E-04	6.82
MD Bottom	2.48	9.96	5.13	0.16	0.40	0.14	0.81	1.70E-02	3.92	5.47E-04	7.60

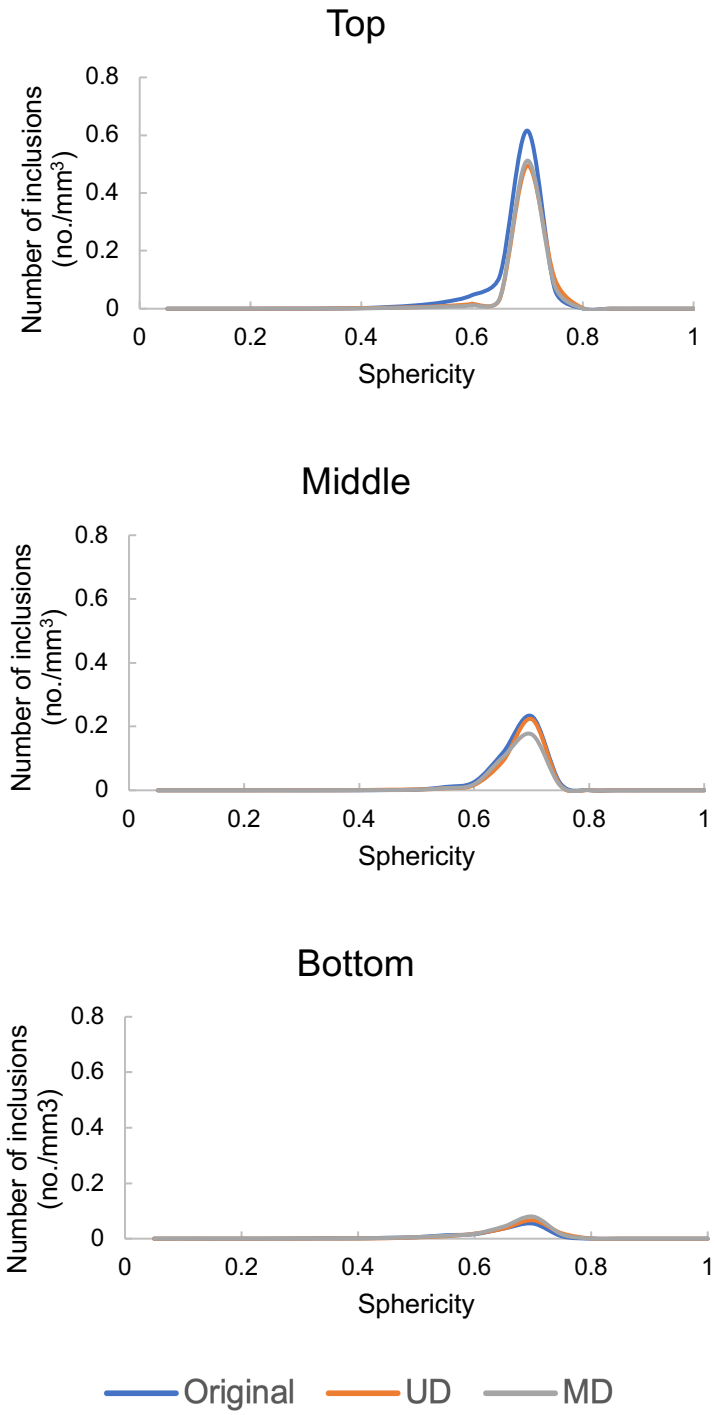


Figure E.4: Effects of heating on the sphericity of all the air inclusions from a top, middle and bottom section of an ice core

Appendix F: Statistical Analysis Results

Table F.1: Two-Factor ANOVA without replication associated with total porosity of the original, UD and MD samples of the low temperature and heating method sequence

Source of Variation	SS	df	MS	F	P-value	F crit
Heating Methods	0.000530	2	0.000265	3.65	0.125	6.94
Sample Depths	0.00321	2	0.00161	22.2	0.00685	6.94
Error	0.000290	4	7.25E-05			
Total	0.00403	8				

Table F.2: Two-Factor ANOVA without replication associated with brine porosities of the original, UD and MD samples of the low temperature and heating method sequence

Source of Variation	SS	df	MS	F	P-value	F crit
Heating Methods	0.000492	2	0.000246	7.36	0.0456	6.94
Sample Depths	0.000189	2	9.45E-05	2.83	0.172	6.94
Error	0.000134	4	3.34E-05			
Total	0.000814	8				

Table F.3: Two-Factor ANOVA without replication associated with brine porosities between the different heating methods

Source of Variation	SS	df	MS	F	P-value	F crit
Heating Methods	2.24E-06	1	2.24E-06	0.144	0.740	18.5
Sample Depths	3.02E-05	2	1.51E-05	0.973	0.507	19
Error	3.11E-05	2	1.55E-05			
Total	6.35E-05	5				

Table F.4: Two-Factor ANOVA without replication associated with air porosities of the original, UD and MD samples of the low temperature and heating method sequence

Source of Variation	SS	df	MS	F	P-value	F crit
Heating Methods	4.14E-06	2	2.07E-06	0.274	0.774	6.94
Sample Depths	0.00222	2	0.00111	147	0.000181	6.94
Error	3.03E-05	4	7.56E-06			
Total	0.00225	8				

Table F.5: Two-Factor ANOVA without replication associated with brine number densities of the original, UD and MD samples of the low temperature and heating method sequence

Source of Variation	SS	df	MS	F	P-value	F crit
Heating Methods	24.9	2	12.5	1.84	0.271	6.94
Sample Depths	20.1	2	10.0	1.48	0.330	6.94
Error	27.1	4	6.77			
Total	72.1	8				

Table F.6: Two-Factor ANOVA without replication associated with air number densities of the original, UD and MD samples of the low temperature and heating method sequence

Source of Variation	SS	df	MS	F	P-value	F crit
Heating Methods	0.00862	2	0.00431	1.36	0.354	6.94
Sample Depths	0.461	2	0.231	72.7	0.000717	6.94
Error	0.0127	4	0.00317			
Total	0.482	8				

Table F.7: Two-Factor ANOVA without replication associated with brine horizontal projected dimensions of the original, UD and MD samples of the low temperature and heating method sequence

Source of Variation	SS	df	MS	F	P-value	F crit
Heating Methods	0.00764	2	0.00382	18.4	0.00965	6.94
Sample Depths	0.00206	2	0.00103	4.95	0.0828	6.94
Error	0.000833	4	0.000208			
Total	0.0105	8				

Table F.8: Two-Factor ANOVA without replication associated with brine horizontal projected dimensions between the different heating methods

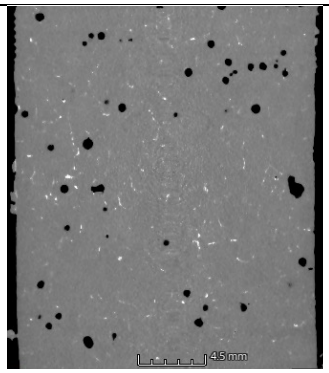
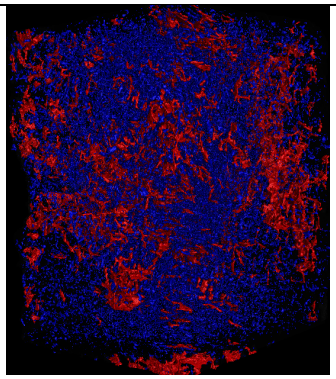
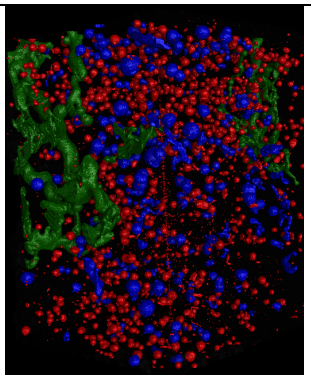
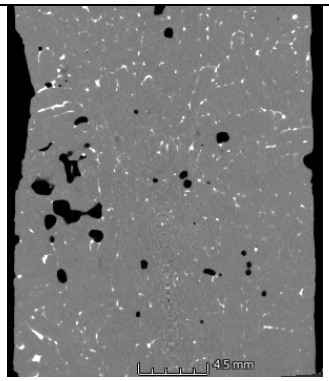
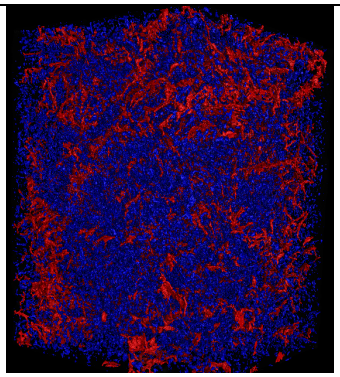
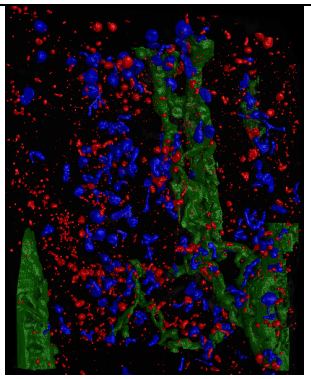
Source of Variation	SS	df	MS	F	P-value	F crit
Heating Methods	5.72E-05	1	5.72E-05	0.201	0.698	18.5
Sample Depths	0.000767	2	0.000383	1.35	0.426	19
Error	0.000568	2	0.000284			
Total	0.00139	5				

Table F.9: Two-Factor ANOVA without replication associated with brine vertical projected dimensions of the original, UD and MD samples of the low temperature and heating method sequence

Source of Variation	SS	df	MS	F	P-value	F crit
Heating Methods	0.00231	2	0.00116	5.17	0.0778	6.94
Sample Depths	0.00156	2	0.000781	3.49	0.132	6.94
Error	0.000894	4	0.000223			
Total	0.00477	8				

Appendix G: Images and Additional Results from CT Scans

The A1 and B1 cores noted no snow on the cores, however, it was noted on the B2 and B3 cores ~8 and ~6 cm of snow respectively. The snow layers were malleable the ice depths noted in the CT figures are related to the solid ice depths disregarding the snow layer as part of the inclusion volume studies due to the errors associated with it malleability. It is further noted there was a 4cm loss in the B2 core due to shattering under the blade during cutting that was mitigated in the depth profile of that core.

Sample Depth (cm)	Grey Scale Image Slices from A1 Core	3D Reconstructed Brine Pores from A1 Core	3D Reconstructed Air Pores from A1 Core
0-5			
5-10			

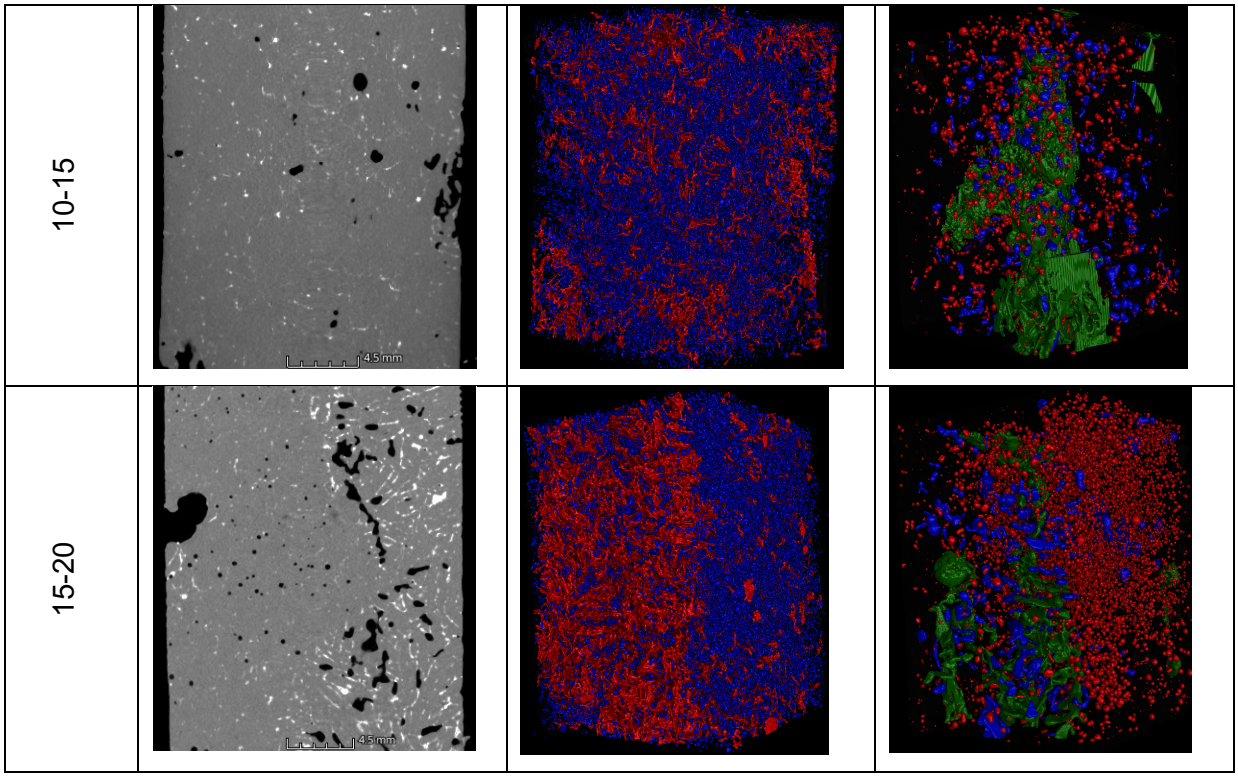
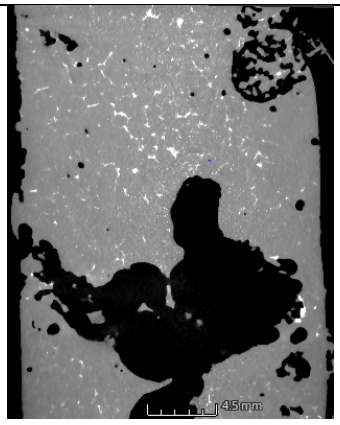
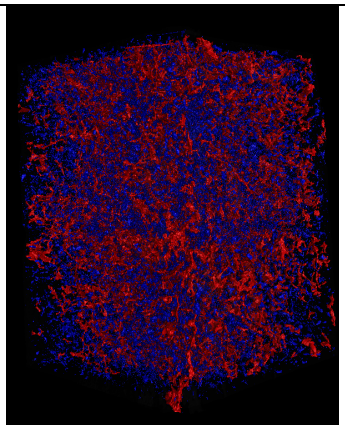
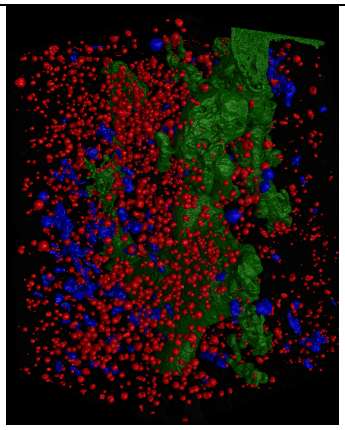
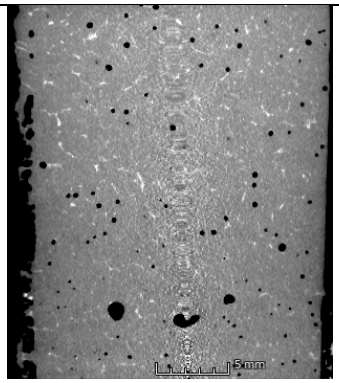
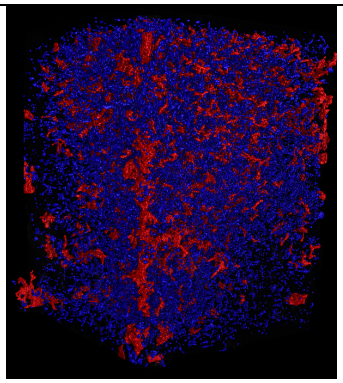
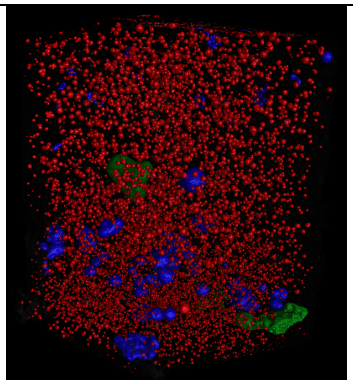
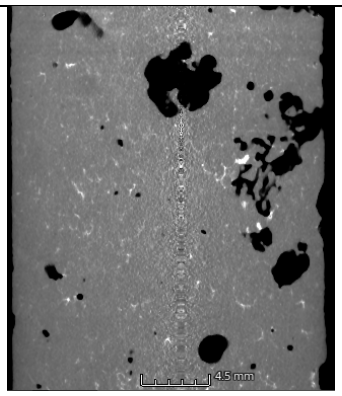
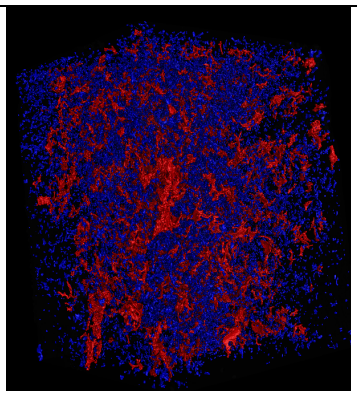
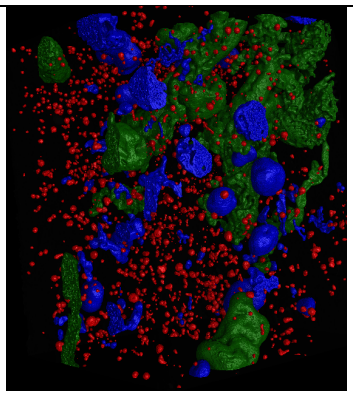
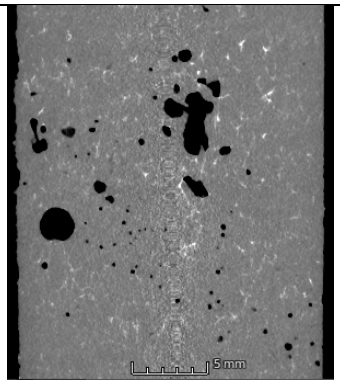
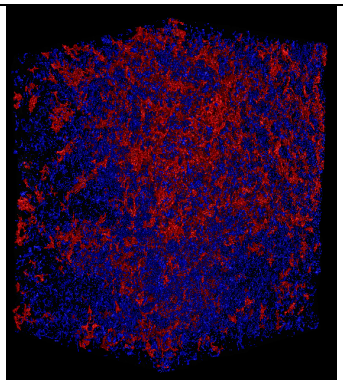
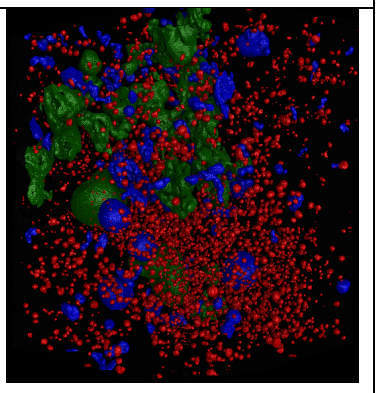
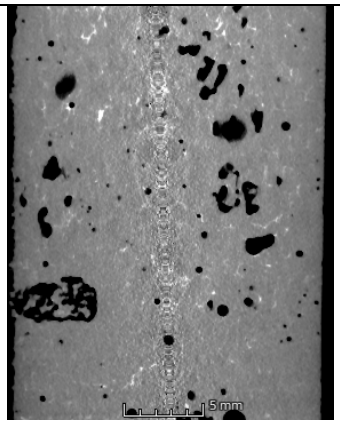
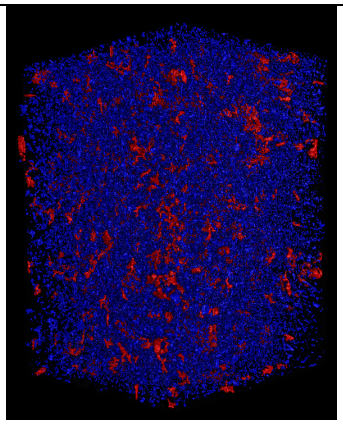
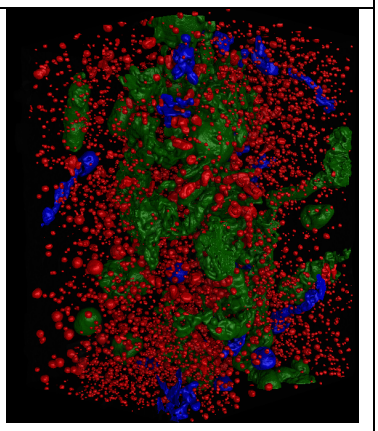
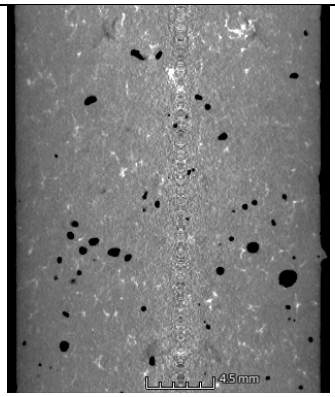
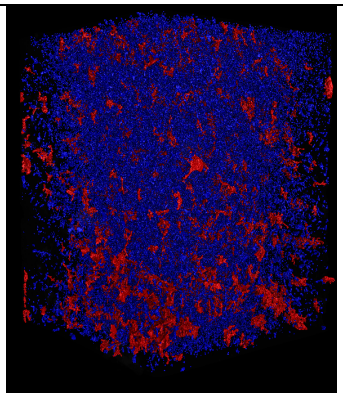
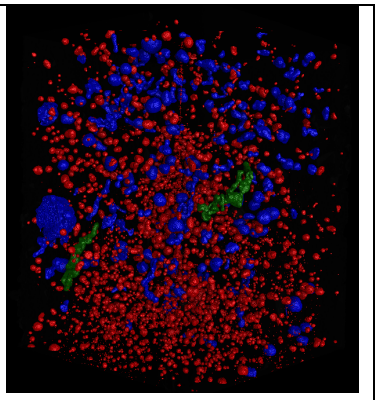
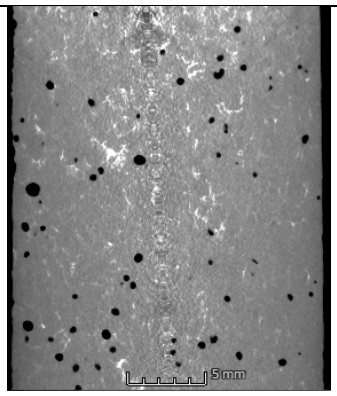
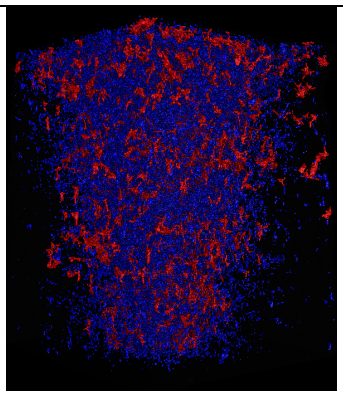
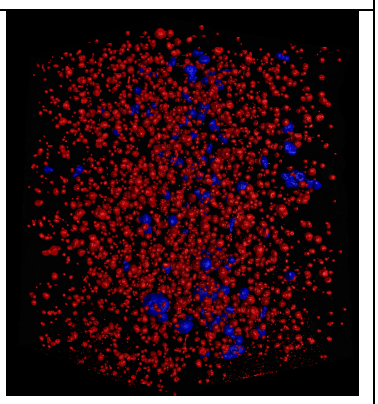
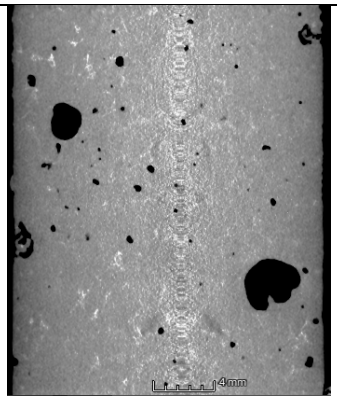
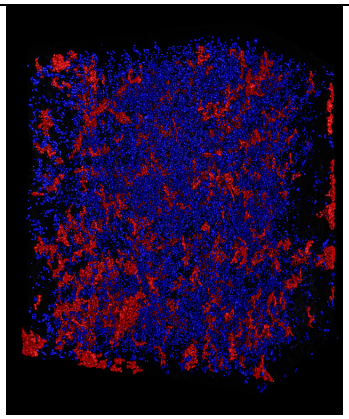
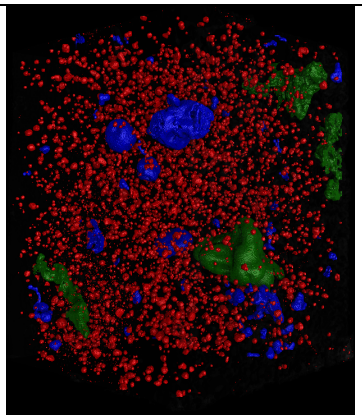
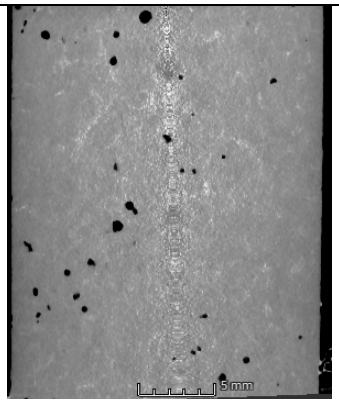
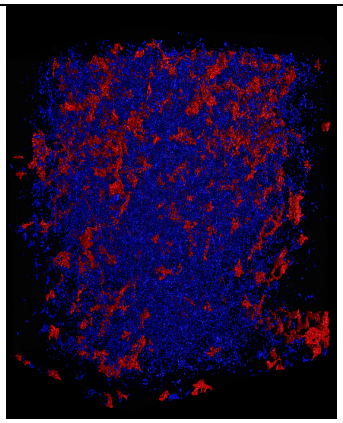
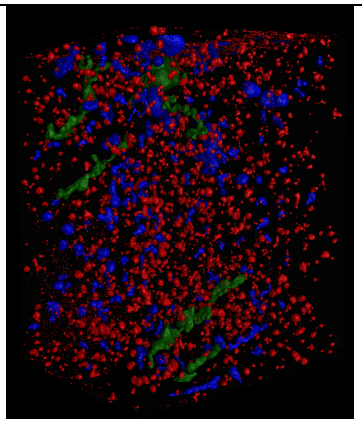


Figure G.1: Greyscale CT Images (left), 3D reconstructions of the brine (middle) and air (right) phases of the A1 winter 2019 CT core

Sample Depth (cm)	Grey Scale Image Slice from B1 Core	3D Reconstructed Brine Pores from B1 Core	3D Reconstructed Air Pores from B1 Core
0-4			

4-7			
7-12			
12-17			
17-22			

22-27			
27-32			
32-36			
36-40			

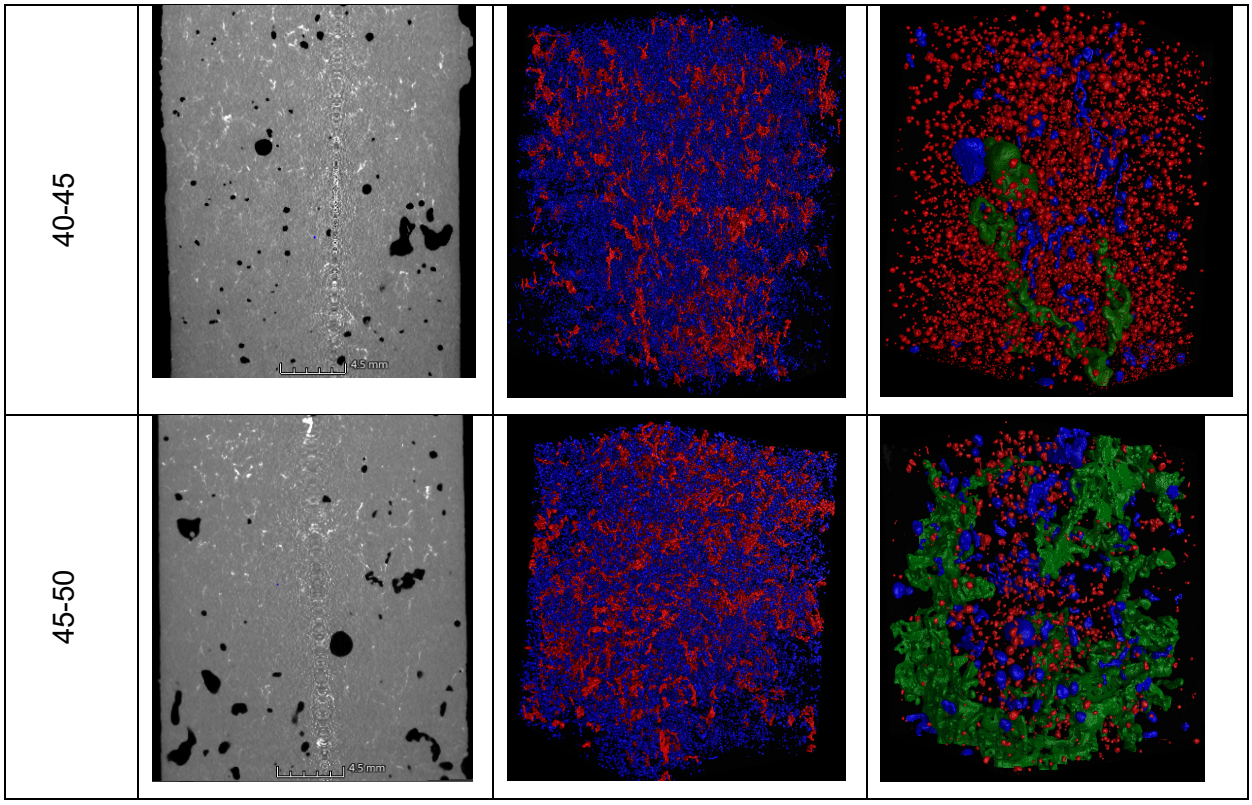
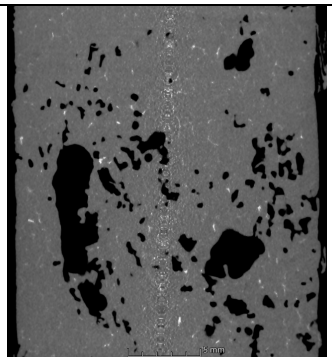
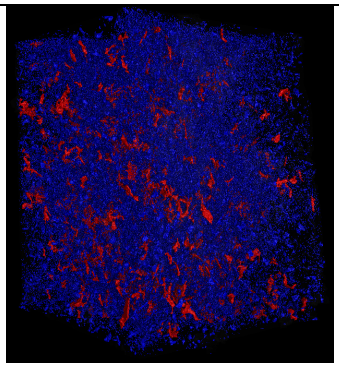
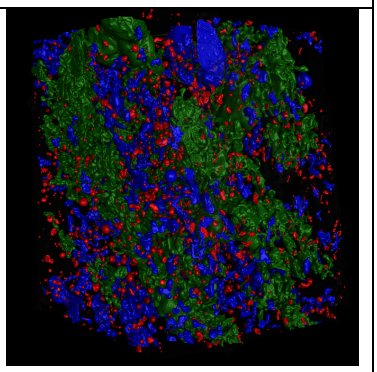
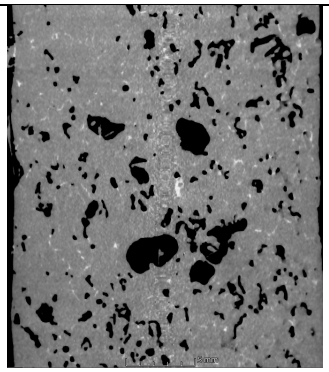
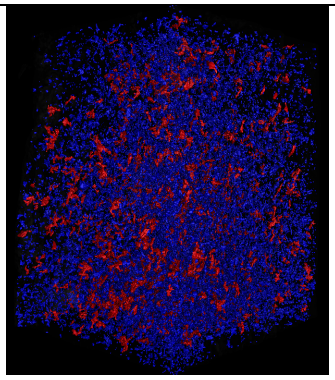
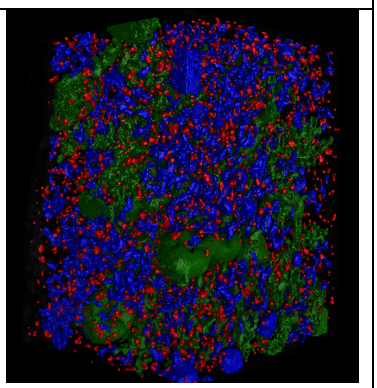
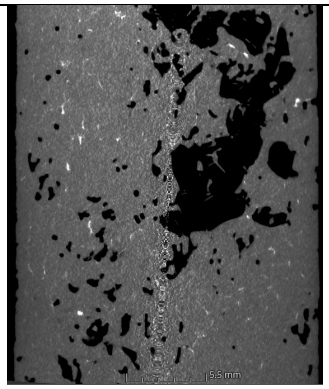
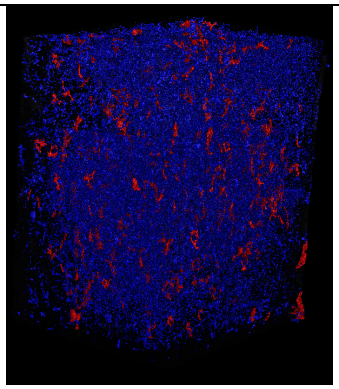
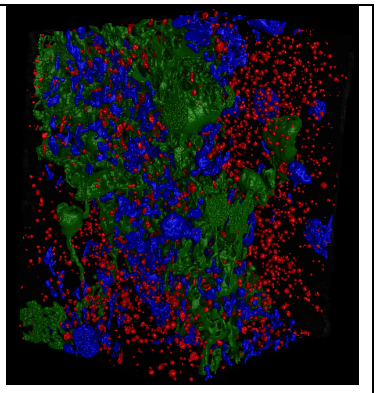
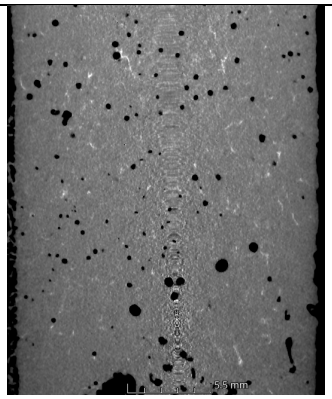
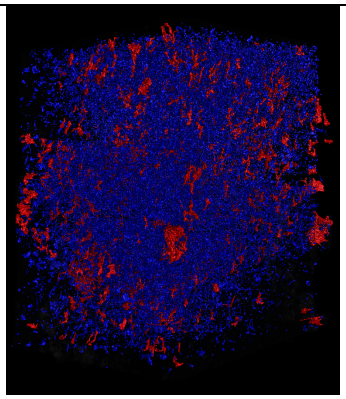
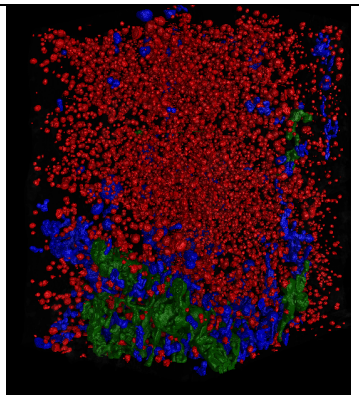
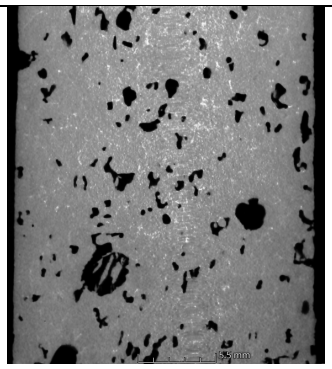
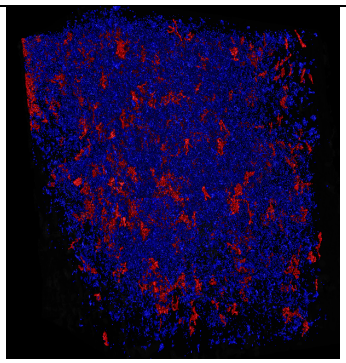
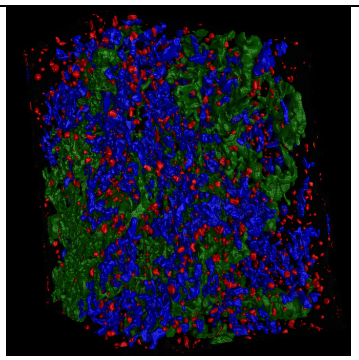
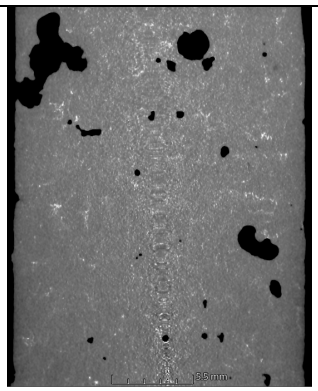
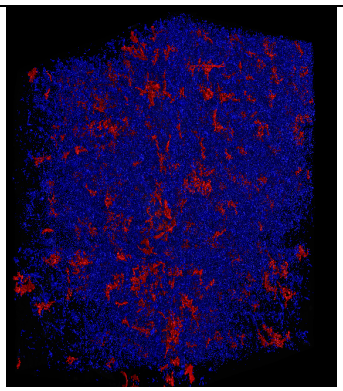
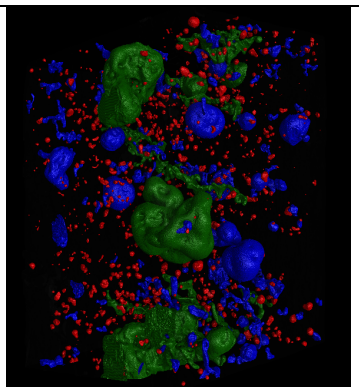


Figure G.2: Greyscale CT Images (left), 3D reconstructions of the brine (middle) and air (right) phases of the B1 winter 2022 CT core

Sample Depth (cm)	Grey Scale Image Slice from B2 Core	3D Reconstructed Brine Pores from B2 Core	3D Reconstructed Air Pores from B2 Core
0-5			
5-10			

10-15			
15-20			
20-25			
25-29			

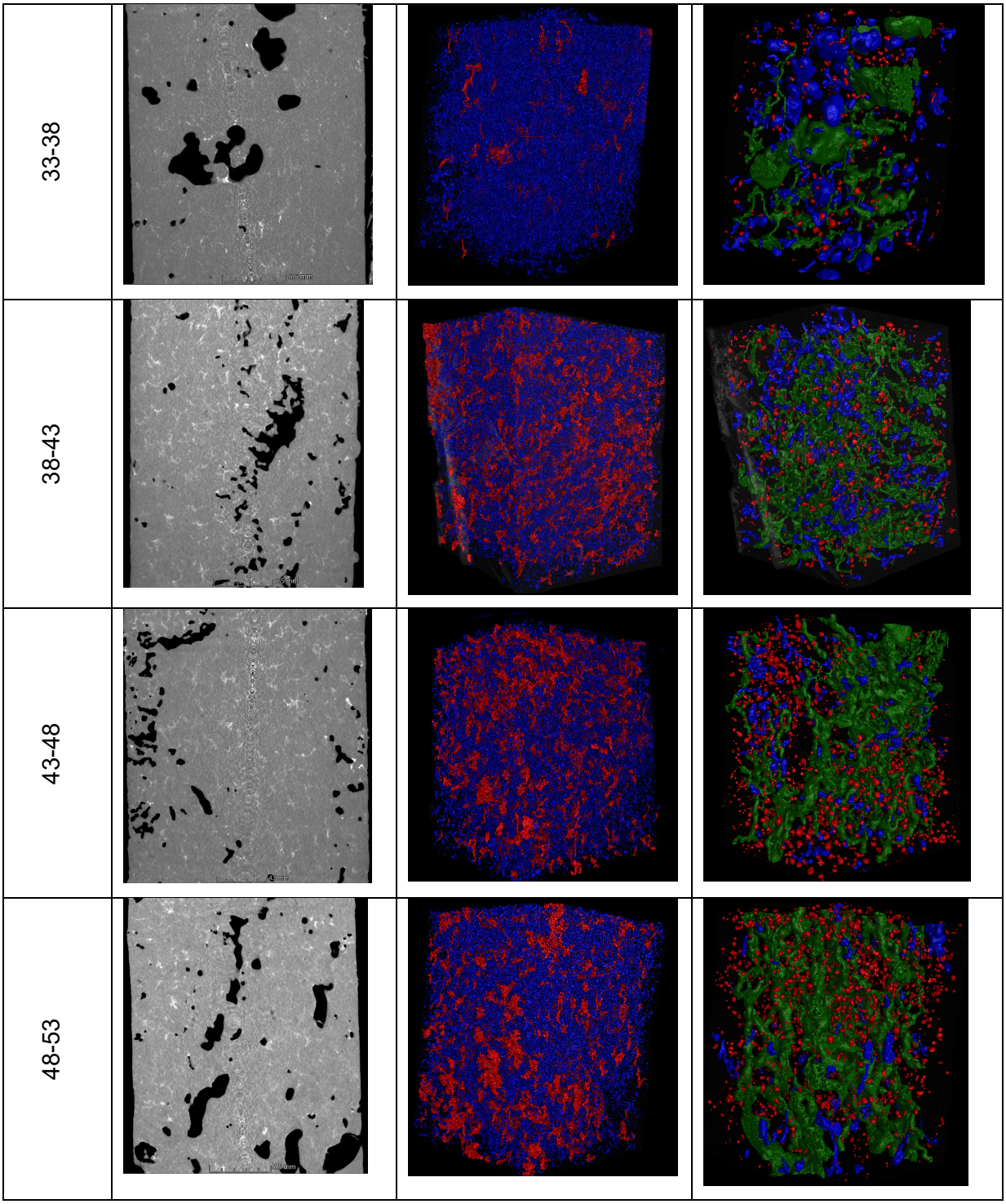
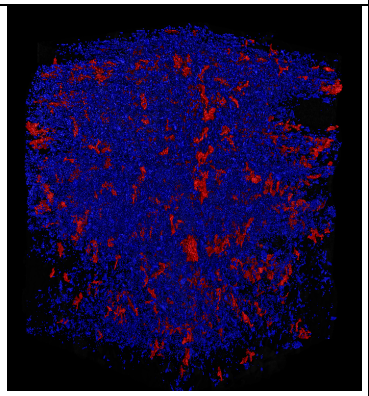
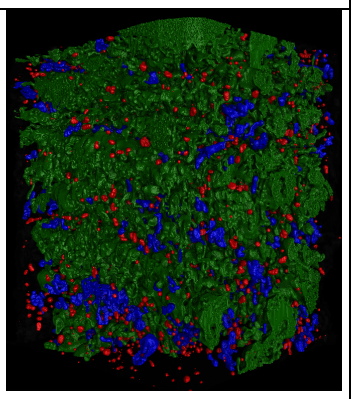
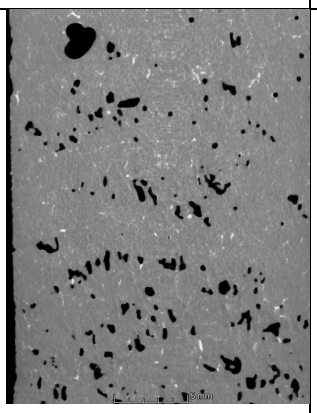
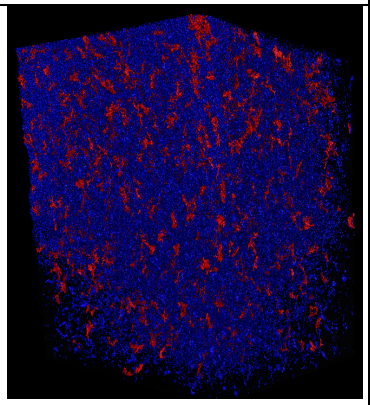
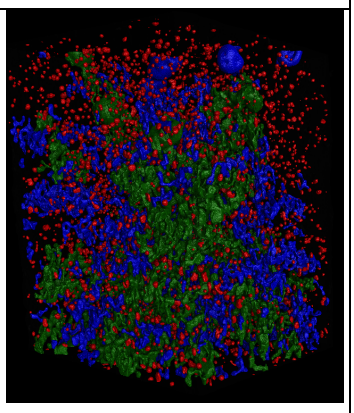
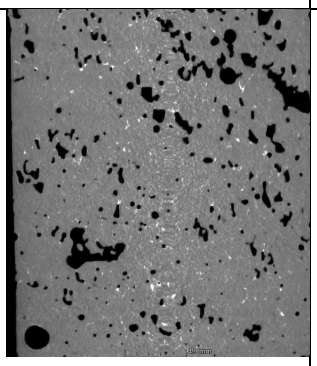
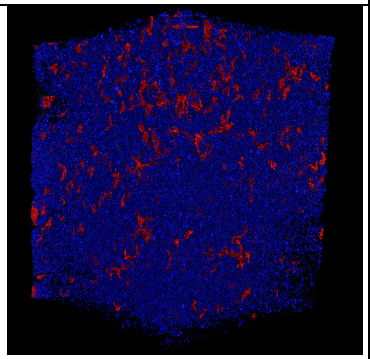
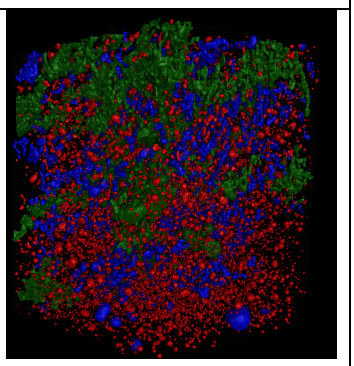
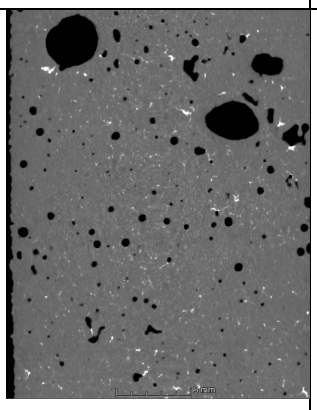
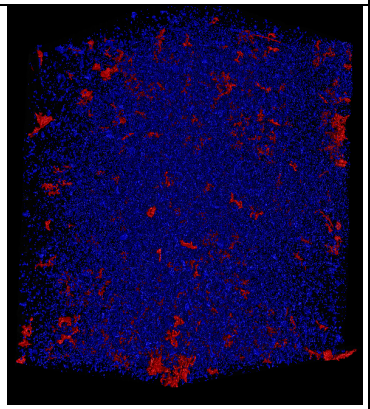
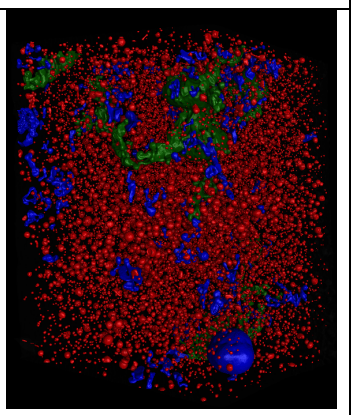
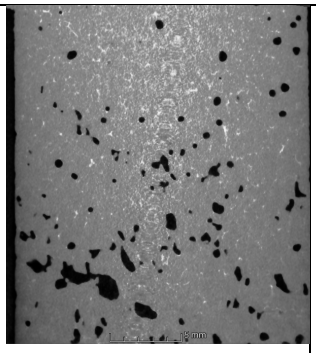
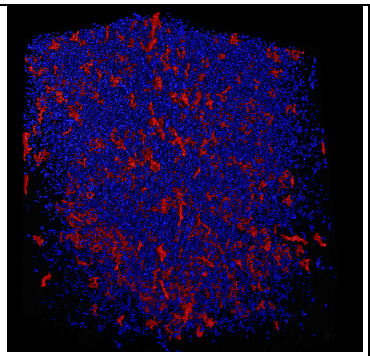
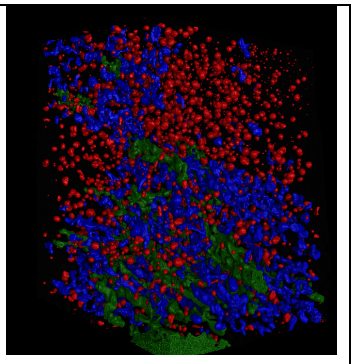
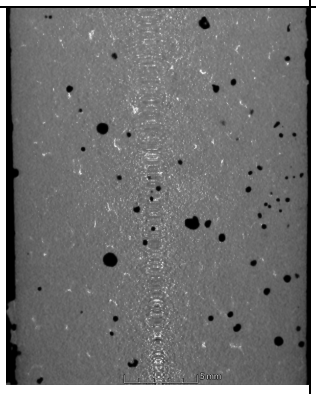
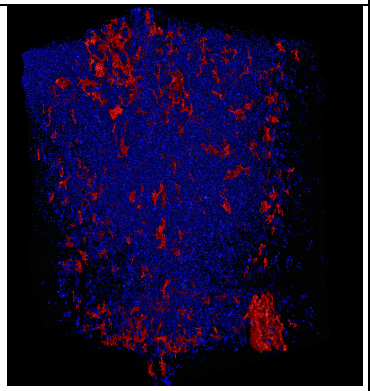
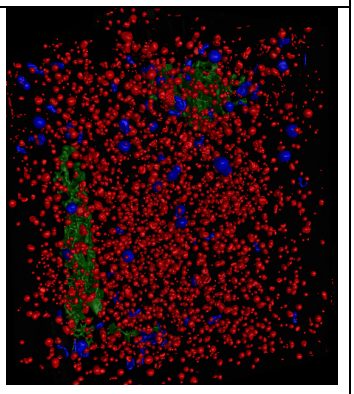
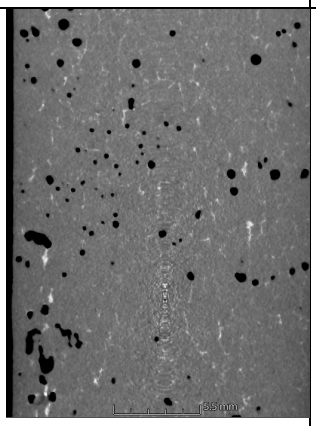
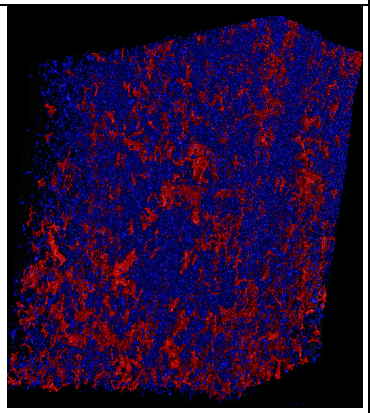
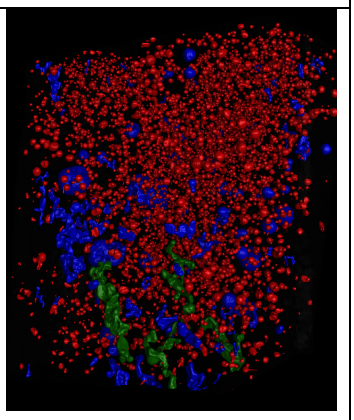
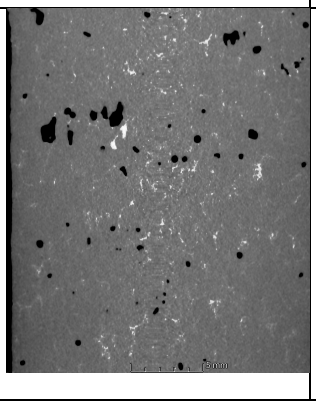
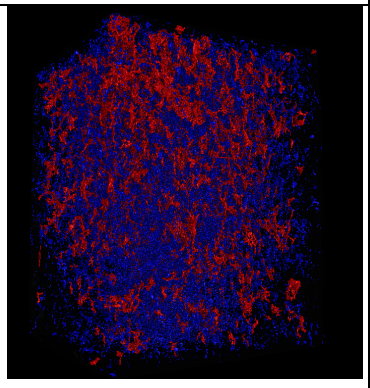
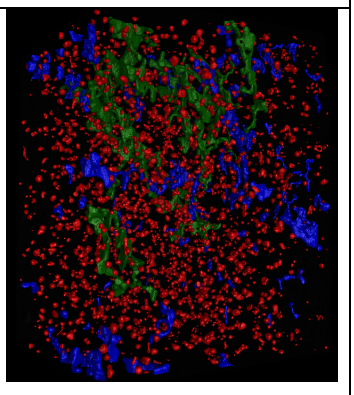


Figure G.3: Greyscale CT Images (left), 3D reconstructions of the brine (middle) and air (right) phases of the B2 winter 2022 CT core

Sample Depth (cm)	Grey Scale Image Slice from B3 Core	3D Reconstructed Brine Pores from B3 Core	3D Reconstructed Air Pores from B3 Core
0-3			
3-7			
7-12			
12-17			

17-22			
22-27.5			
27.5-33			
33-38.5			

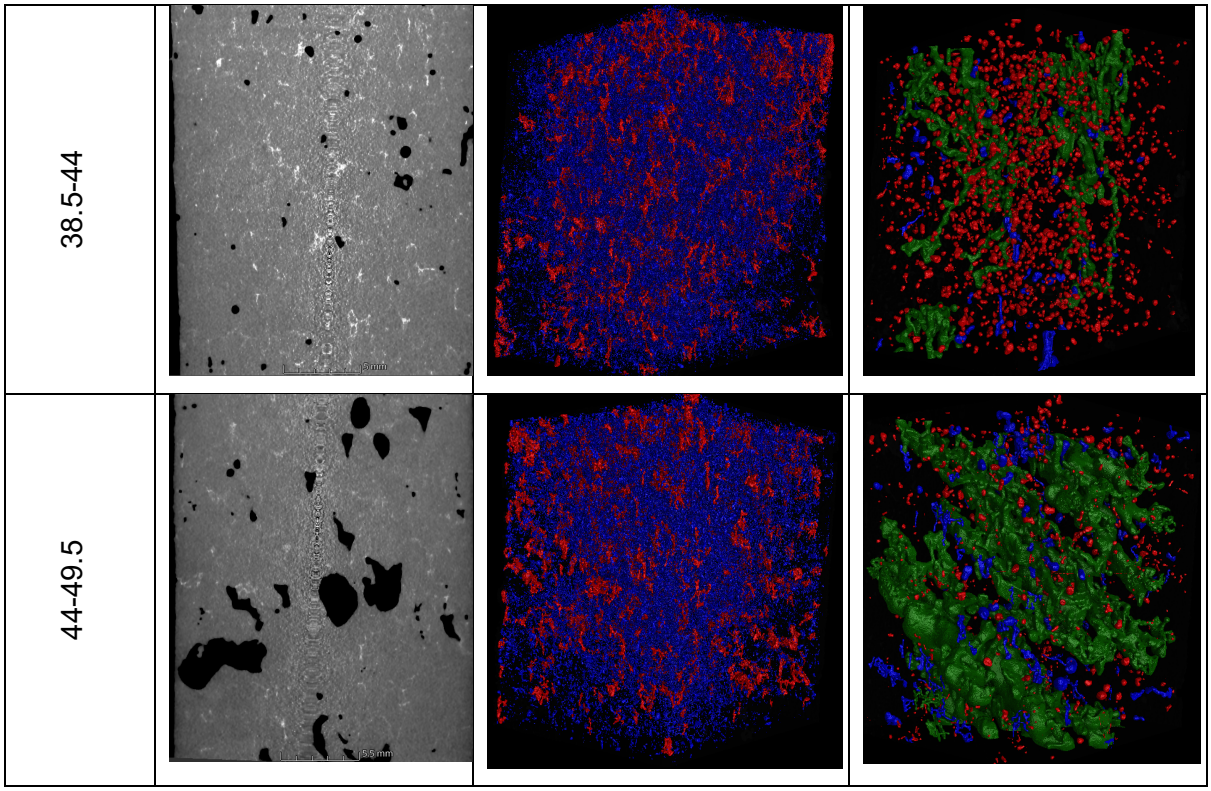


Figure G.4: Greyscale CT Images (left), 3D reconstructions of the brine (middle) and air (right) phases of the B3 winter 2022 CT core

Table G.1: Data generated from CT scans of the winter 2019 A1 core

A1	Brine		Air								
					Micro		Large		Macro		
Ice Depth (cm)	Porosity (%)	Inclusion No. Density (no/mm³)	Porosity (%)	Inclusion No. Density (no/mm³)	Porosity (%)	Inclusion No. Density (no/mm³)	Porosity (%)	Inclusion No. Density (no/mm³)	Porosity (%)	Inclusion No. Density (no/mm³)	Total Porosity (%)
0-5	1.08	5.08	2.33	0.18	0.63	0.16	0.55	1.36E-02	1.15	4.58E-04	3.41
5-10	2.20	8.03	0.42	0.17	0.10	0.16	0.30	9.24E-03	0.02	1.00E-04	2.61
10-15	1.26	4.35	2.76	0.15	0.22	0.14	0.17	8.35E-03	2.38	3.75E-04	4.02
15-20	4.61	6.95	2.55	0.78	0.64	0.77	0.88	1.02E-02	1.03	1.93E-04	7.16

Table G.2: Data generated from CT scans of the winter 2022 B1 core

B1	Brine		Air								
					Micro		Large		Macro		
Ice Depth (cm)	Porosity (%)	Inclusion No. Density (no/mm³)	Porosity (%)	Inclusion No. Density (no/mm³)	Porosity (%)	Inclusion No. Density (no/mm³)	Porosity (%)	Inclusion No. Density (no/mm³)	Porosity (%)	Inclusion No. Density (no/mm³)	Total Porosity (%)
0-4	2.65	7.30	6.49	0.30	0.84	0.29	0.44	1.35E-02	5.21	8.00E-04	9.13
4-7	4.03	5.87	2.12	0.82	0.97	0.82	0.76	4.91E-03	0.39	2.59E-04	6.15
7-12	2.11	3.24	6.64	0.21	0.38	0.20	1.29	8.10E-03	4.97	8.10E-04	8.75
12-17	1.93	8.51	5.24	0.42	0.69	0.41	1.03	1.15E-02	3.52	1.06E-03	7.17
17-22	3.36	11.17	6.78	0.57	0.85	0.56	1.15	1.32E-02	4.77	1.63E-03	10.14
22-27	3.16	14.44	1.84	0.36	0.91	0.34	0.87	1.97E-02	0.05	1.82E-04	5.00
27-32	2.26	7.52	1.51	0.38	1.11	0.37	0.40	9.50E-03	0	0	3.77
32-36	1.82	3.20	2.31	0.57	0.78	0.57	0.49	5.85E-03	1.05	4.50E-04	4.13
36-40	1.47	9.29	1.51	0.46	0.57	0.44	0.61	1.85E-02	0.33	5.42E-04	2.98
40-45	1.72	11.11	2.39	0.77	1.07	0.76	0.52	1.03E-02	0.80	2.56E-04	4.11
45-50	4.39	8.04	5.63	0.64	0.44	0.62	0.90	1.96E-02	4.28	3.80E-04	10.02

Table G.3: Data generated from CT scans of the winter 2022 B2 core

B2	Brine		Air								
					Micro		Large		Macro		
Ice Depth (cm)	Porosity (%)	Inclusion No. Density (no/mm³)	Porosity (%)	Inclusion No. Density (no/mm³)	Porosity (%)	Inclusion No. Density (no/mm³)	Porosity (%)	Inclusion No. Density (no/mm³)	Porosity (%)	Inclusion No. Density (no/mm³)	Total Porosity (%)
0-5	1.96	27.12	9.80	0.31	0.49	0.26	1.77	4.80E-02	7.54	2.54E-03	11.76
5-10	1.49	3.37	12.59	0.51	0.86	0.42	3.05	8.79E-02	8.68	3.25E-03	14.08
10-15	1.16	13.20	10.06	0.35	0.51	0.31	1.15	3.71E-02	8.40	7.81E-04	11.21
15-20	1.63	12.83	3.70	0.90	1.65	0.88	1.14	2.52E-02	0.90	7.97E-04	5.33
20-25	1.58	11.79	10.42	0.22	0.39	0.16	2.07	5.42E-02	7.95	2.09E-03	12.00
25-29	2.04	30.31	3.91	0.12	0.23	0.10	1.40	1.40E-02	2.29	1.49E-03	5.95
33-38	2.02	40.92	5.54	0.08	0.15	0.06	1.90	1.68E-02	3.49	1.73E-03	7.57
38-43	4.60	22.26	4.38	0.16	0.23	0.14	0.68	2.43E-02	3.48	9.67E-04	8.98
43-48	3.58	21.87	5.14	0.32	0.42	0.31	0.36	1.40E-02	4.36	5.43E-04	8.72
48-53	2.99	10.43	5.83	0.25	0.43	0.24	0.29	1.30E-02	5.11	6.27E-04	8.82

Table G.4: Data generated from CT scans of the winter 2022 B3 core

B3	Brine		Air								
					Micro		Large		Macro		
Ice Depth (cm)	Porosity (%)	Inclusion No. Density (no/mm³)	Porosity (%)	Inclusion No. Density (no/mm³)	Porosity (%)	Inclusion No. Density (no/mm³)	Porosity (%)	Inclusion No. Density (no/mm³)	Porosity (%)	Inclusion No. Density (no/mm³)	Total Porosity (%)
0-3	2.26	14.05	22.59	0.27	0.50	0.22	1.54	4.88E-02	20.55	1.33E-03	24.85
3-7	2.48	24.60	5.73	0.45	0.66	0.39	1.72	5.24E-02	3.34	3.35E-03	8.20
7-12	2.62	28.33	6.64	1.04	0.96	0.99	1.44	4.86E-02	4.24	1.37E-03	9.25
12-17	1.41	9.41	3.31	1.41	1.53	1.40	0.63	1.55E-02	1.16	7.05E-04	4.73
17-22	4.51	7.26	4.19	0.29	1.13	0.25	1.67	4.33E-02	1.39	2.83E-03	8.70
22-27.5	1.06	17.73	1.74	0.30	0.95	0.30	0.21	7.01E-03	0.58	2.73E-04	2.80
27.5-33	3.86	38.53	2.13	0.48	1.03	0.47	0.96	1.27E-02	0.13	4.52E-04	5.99
33-38.5	2.10	10.86	1.65	0.24	0.52	0.22	0.42	1.23E-02	0.71	1.14E-03	3.75
38.5-44	1.86	18.52	2.14	0.19	0.53	0.19	0.11	7.11E-03	1.50	6.91E-04	4.00
44-49.5	1.80	11.24	8.13	0.12	0.19	0.11	0.26	1.43E-02	7.69	4.47E-04	9.93

Table G.5: Summary of winter 2019 vs 2022 results

	Winter 2019	Winter 2022
Average crystal size (mm)	1.98±0.15	1.74±0.12
Brine porosity (%)	2.29±1.59	2.63±0.58
Air porosity (%)	2.02±1.06	3.86±1.33
Number of brine inclusions (no./mm^3)	6.1±1.65	8.15±1.99
Average brine inclusion volume (mm^3)	0.0036±0.0020	0.0038±0.0012
Average brine inclusion sphericity	0.28±0.01	0.67±0.03
Number of air inclusions (no./mm^3)	0.32±0.30	0.50±0.11
Average air inclusion volume (mm^3)	0.093±0.076	0.099±0.055